# QUANTIFICATION OF OXYGEN SATURATION

# OF VENOUS VESSELS

# USING SUSCEPTIBILITY MAPPING

# QUANTIFICATION OF OXYGEN SATURATION
# OF VENOUS VESSELS
# USING SUSCEPTIBILITY MAPPING

BY

JIN TANG, M.A.Sc

A Thesis

Submitted to the School of Graduate Studies

in Partial Fulfillment of the Requirements

for the Degree of

PhD

in Biomedical Engineering

McMaster University

| | |
|---|---|
| PHD (2012) | McMaster University |
| (Biomedical Engineering) | Hamilton, ON, Canada |

TITLE: Quantification of Oxygen Saturation of Venous Vessels Using Susceptibility Mapping

AUTHOR: Jin Tang, M.A.Sc. (McMaster University)

SUPERVISOR: Professor E. Mark Haacke

NUMBER OF PAGES: ix, 119

# Abstract

The regulation of oxygen supply and consumption by the brain is a complex and dynamic process. The determination of the oxygen saturation of venous blood is an indirect means to assess local tissue oxygen saturation. Quantitatively measuring oxygen saturation is important to characterize the physiological or pathological state of tissue function. Noninvasive and reliable measurements can help to better understand the changes in cerebral hemodynamics due to neuronal activation or to improve the characterization and monitoring of treatment of cerebral pathologies, such as stroke, multiple sclerosis (MS) or tumors. There are several methods available to quantify blood or tissue oxygenation. Most methods are invasive requiring the insertion of a catheter into the jugular vein or using radioactive isotopes, such as positron emission tomography (PET). Near-infrared spectroscopy (NIRS), a noninvasive method, can only access surface cortical structures of the brain due to the limited penetration of light into the tissue. MRI has the potential to estimate the blood oxygen saturation level because of the difference of the magnetic properties of oxygenated and deoxygenated blood. Deoxygenated blood in veins is less diamagnetic than oxygenated blood, and relative to the surrounding tissue it appears to be paramagnetic, which makes it possible to detect venous oxygen saturation levels using either susceptibility weighted MRI or susceptibility mapping.

In this thesis, we demonstrate the possibility of using susceptibility mapping to noninvasively estimate the venous blood oxygen saturation level. Accurate susceptibility quantification is the key to oxygen saturation quantification. Two approaches are presented in this thesis to generate accurate and artifact free susceptibility maps (SM): a regularized inverse filter and a k-space iterative method. Using the regularized inverse filter, with sufficient resolution, major veins in the brain can be visualized. The usual geometry dependent phase dipole effects can be removed leaving basically images of the veins. We found that different sized vessels show a different level of contrast depending on their partial volume effects; smaller vessels show smaller values due to errors in the methodology and due to partial volume effects; larger vessels show a bias toward a reduced susceptibility approaching 90% of the expected value. Also, streaking artifacts associated with high susceptibility structures such as veins are obvious in the reconstructed susceptibility map.

To further improve susceptibility quantification and reduce the streaking artifacts in the susceptibility maps, we proposed a threshold-based k-space/image domain iterative approach that used geometric information from the susceptibility map itself as a constraint to overcome the ill-posed nature of the inverse filter. Both simulations and *in vivo* results show that most streaking artifacts inside the susceptibility map caused by the ill-defined inverse filter were suppressed by the iterative approach. In simulated data, the bias toward lower mean susceptibility values inside vessels has been shown to decrease from around 10% to 2% when choosing an appropriate threshold value for the proposed iterative method. Typically, three iterations are sufficient for this approach to converge and this process takes less than 30 seconds to process for a 512 × 512 × 256 dataset. Generally, this new iterative method improves quantification of susceptibility inside vessels and reduces streaking artifacts throughout the brain for data collected from a single-orientation acquisition. This approach has been applied to vessels alone as well as to vessels and other structures such as the basal ganglia with lower susceptibility to generate whole brain susceptibility maps with significantly reduced streaking artifacts.

In summary, susceptibility maps based on the regularized inverse filter can successfully create venograms of the brain with varying levels of contrast-to-noise depending on the size of the vessel. These venograms have the potential to map oxygen saturation, especially when the resolution is high enough that there are several pixels across a vessel. The k-space iterative approach reduced the streaking artifacts and improved the accuracy of the calculated susceptibility maps bringing us one step closer to a practical means to map out oxygen saturation in the brain.

## Acknowledgements

First of all, I would like to express my sincere thanks and deep appreciation to my supervisor, Dr. E. Mark Haacke for his enduring inspiration, guidance, support and encouragement all through my study. I feel so lucky to have a supervisor who is a remarkable scientist and cares about his students and their research and who has responded to questions and queries so promptly. No matter when I sent an email to him, midnight or very early in the morning, I always got a reply right away. Thanks for spending the whole new year holidays helping me with my paper. I cannot thank him enough for what he has done for me.

I would like to thank my supervisory committee for all the valuable comments and suggestions that they provided for me during my research. I enjoyed committee meetings every year. Thanks to Dr. Michael Noseworthy for the wonderful MRI courses that he offered. I learned a great deal from his courses and enjoyed them all. Thanks to my Master's supervisor, Dr. Spencer Smith, for spending another four years supervising me and thanks for the scientific computing knowledge that he delivered to me during my Masters which still benefits my current research. Thanks to Dr. Alan Wassyng for all his advice, especially that linking my software engineering background to my current research. I will always keep this advice in mind. Thanks to Dr. Maureen Macdonald for her clearly and simply explaining physiology and anatomy to me during committee meetings. Her expertise on physiology and anatomy helped my research about blood oxygen saturation on the right track.

I also acknowledge Dr. Yu-Chung Norman Cheng and Dr. Jaladhar Neelavalli at Wayne State University, for all the time and energy that they spent helping me with my research. In addition, I am indebted to my student colleagues at McMaster, Saifeng Liu, Sagar Buch and Karen Mok for their help and sharing ideas and experiences.

I also want to thank many others in the MRI institute in Detroit, Rachel Martis Laze, Jing Jiang, Manju Liu, Yi Zhong, Ying Wang, Weili Zheng, Wei Feng and Yongquan Ye for their support and friendship.

Lastly, and most importantly, I wish to thank my parents, Qingli Li and Songmo Tang, my grandparents, Sanyu Xu and Zhenbang Li, and my sister, Min Tang, for the support, encouragement and endless love they provided me through my entire life. I could not have done this without them. This thesis is dedicated to them.

## Table of Contents

Chapter 1: Introduction ........................................................................................ 1
  1.1 Background and Significance........................................................................ 2
  1.2 Approaches to Measure Oxygen Saturation................................................. 4
  1.3 Motivation of the Study ............................................................................... 8
  1.4 Overview of Thesis...................................................................................... 10
Chapter 2: Susceptibility, MRI Phase and Susceptibility Mapping ..................................... 19
  2.1 Introduction of Susceptibility....................................................................... 20
    2.1.1 Bulk Magnetic Fields ............................................................................. 20
    2.1.2 Diamagnetism, Paramagnetism and Ferromagnetism .......................... 22
  2.2 Susceptibility and Oxygenation Level ........................................................ 22
  2.3 MRI Phase and Its Relationship to Susceptibility ...................................... 24
    2.3.1 Introduction of MRI Phase .................................................................... 24
    2.3.2 Relationship between Phase and Susceptibility.................................... 25
    2.3.3 Limitation of Phase ............................................................................... 25
  2.4 Susceptibility Mapping ............................................................................... 26
    2.4.1 Introduction of Susceptibility Mapping................................................. 26
    2.4.2 Susceptibility Map Calculation.............................................................. 27
Chapter 3: Susceptibility Mapping as a Means to Visualize Veins and Quantify Oxygen Saturation.............................................................................................................. 35
  3.1 Introduction ................................................................................................ 36
  3.2 Materials and Methods................................................................................ 37
  3.3 Results......................................................................................................... 44
  3.4 Discussion................................................................................................... 65

Chapter 4: Improving Susceptibility Mapping Using a Threshold-Based K-space/Image Domain Iterative Fourier Transform Reconstruction Approach .......... 76

4.1 Introduction .......... 76

4.2 Materials and Methods .......... 78

4.3 Results .......... 87

4.4 Discussion .......... 99

Chapter 5: Conclusions and Future Directions .......... 107

5.1 Conclusions .......... 108

5.2 Future Directions .......... 114

## List of Acronyms and Notations

| | |
|---|---|
| 2D | two-dimensional |
| 3D | three-dimensional |
| Bo | main magnetic field strength |
| BOLD | blood oxygenation level-dependent |
| $CaO_2$ | arterial oxygen content |
| CBF | cerebral blood flow |
| CBV | cerebral blood volume |
| $CMRO_2$ | cerebral metabolic rate of oxygen utilization |
| CNR | contrast to signal ratio |
| CSF | cerebrospinal fluid |
| DSC-PWI | dynamic susceptibility perfusion-weighted imaging |
| FA | flip angle |
| FWHM | full width at half-maximum |
| fMRI | functional magnetic resonance imaging |
| GM | grey matter |
| GRE | gradient-echo |
| Hct | hematocrit |
| HP | High-pass filter |
| MIP | maximum intensity projection |
| MRI | magnetic resonance imaging |
| MS | multiple sclerosis |
| MTT | mean transit time |
| mIP | minimum intensity projection |
| NIRS | near-infrared spectroscopy |
| OEF | oxygen extraction fraction |
| PET | positron emission tomography |
| RMSE | root mean squared error |
| ROI | region of interest |

| | |
|---|---|
| SD | standard deviation |
| SHARP | sophisticated harmonic artifact reduction for phase data |
| SM | susceptibility map |
| SNR | signal-to-noise ratio |
| SWI | susceptibility weight imaging |
| T | Tesla. Unit of magnetic field strength |
| T1 | spin-lattice relaxation time |
| T2 | spin-spin relaxation time |
| T2* | effective transverse relaxation decay |
| TBSO | threshold-based, single-orientation regularization method |
| TE | echo time |
| TOA | timeof arrival |
| Ya | arterial oxygen saturation level |
| Yv | venous oxygen saturation level |

# Chapter 1: Introduction

### 1.1 Background and Significance

The brain represents only 2% of the body weight; however, it receives 15% of the cardiac output and consumes 20% of the total body oxygen (1). This highlights the critical dependence of brain function on continuous, efficient usage of oxygen, and the organ's heightened vulnerability and sensitivity to alterations in oxygen supply. Accurate methods of measuring hemodynamics and oxygen metabolism in the brain and cardiovascular system have been important areas of study for neurological and cardiac diseases for decades (2–11). Many of the most common disorders of the brain, such as Alzheimer's, Parkinson's, Huntington's, multiple sclerosis (MS) and others, have been found to be associated with alterations in cerebral oxygen metabolism(12–15). Measurement of the cerebral metabolic rate of oxygen ($CMRO_2$) consumption will further enhance our understanding of normal cerebral physiology during rest, sleep, anesthesia, aging, functional brain tasks, and physiologic challenges, and will be useful for evaluating the effect of systemic disease processes such as hypertension and diabetes on cerebral oxygen metabolism.

The regulation of oxygen supply and consumption by the brain tissue for its metabolic processes is a complex and dynamic process. The amount of oxygen delivered is dependent on the tissue metabolic requirement and on physiologic parameters such as the arterial oxygen content, blood flow rate and hematocrit (Hct). The difference in oxygen content between the afferent arterial blood and the efferent venous blood reflects the amount of oxygen utilized by the tissue for its metabolic processes; therefore, $CMRO_2$can be estimated by combining venous and arterial oxygen saturation and CBF measurements using Fick's principle (16), $CMRO_2=CaO_2 \times CBF \times OEF$ [1]

where $CaO_2$ indicates the arterial oxygen content, CBF indicates cerebral blood flow rate and OEF denotes the oxygen extraction ratio defined as (Ya-Yv)/Ya. Here, Ya and Yv denote the oxygen saturation values of arteries and veins, respectively. Oxygen saturation refers to the fraction of hemoglobin that is saturated by oxygen. There is debate as to what is the normal range of Yv, but most authorities assume 50-54% to be the lower limit of normal and 75% the upper limit (17).For arterial oxygen saturation, Ya, the normal values are 97% to 99% in the healthy individual (18). In most studies, Ya is assumed to be 98% or even 100%. If Ya is assumed to be 100%, then OEF could be defined as 1-Yv. Therefore, Eq.[1] can be replaced by

$$CMRO_2=CaO_2 \times CBF \times (1-Yv) \qquad [2]$$

Under various physiological challenges, the body maintains a balance between oxygen supply and consumption by modulation of the CBF and OEF / Yv (19, 20). Dynamic susceptibility perfusion-weighted imaging (DSC-PWI) provides cerebral blood volume (CBV), cerebral blood flow (CBF), time of arrival (TOA) and mean transit time (MTT) maps. The picture is almost complete, but it misses the key ingredient to calculate the OEF and CMRO2: the venous oxygen saturation, Yv. If we can monitor the venous oxygen saturation, then we would have a complete picture of the tissue hemodynamics in the brain from MRI. This would be a major step forward for *in vivo* diagnostic imaging of disease and tissue function.

## 1.2 Approaches to Measure Oxygen Saturation

Currently, oxygen metabolism is not routinely measured clinically, in that several practical limitations have prevented its widespread application.

- Non-MRI Approaches

1) Positron Emission Tomography (PET)

Positron emission tomography provides the most direct measurement of oxygen metabolism through imaging of the accumulated inhaled 15O-labeled radiotracers in the brain, which, after distribution into the tissue, are converted into 15O-labeled water (21). Positron emission tomography is, however, restrictive in terms of its utility because of the high radiation dose, relatively complex setup required for the constant delivery of radio-labeled gases, high associated expenses, and long scan times, during which it is assumed that no change in physiologic state occurs.

2) Jugular Vein Oximetry

Another method for quantifying oxygen saturation is to use jugular vein oximetry involving catheterization and measuring flow through optical measurements or Doppler ultrasound (22). However, because of the invasiveness of the technique, it is prone to complications such as carotid artery puncture (incidence 1% to 4.5%), hematoma formation, jugular vein occlusion, thrombosis, risk of bacteremia, and other infections (23). In addition, the accuracy of the method is highly dependent on personnel skill and experience.

3) Near-infrared spectroscopy

Near-infrared spectroscopy has been proposed as a non-invasive alternative for assessing cerebral oxygenation during cardiac operations (24). Near-infrared spectroscopy is relatively inexpensive, has excellent temporal resolution, and is less hampered by subject motion. This technique measures regional oxygen saturation in cerebral tissue by analyzing the spectrum of reflected near-infrared light. It only requires a portable device, and thus can be easily implemented. However, due to the poor penetration of tissue by light, this technique is limited to superficial capillary sampling. Moreover, the localization of the reflected signal is uncertain and there is controversy regarding possible contributions to the signal from arteries and veins. The measurement obtained correlates with venous oxygen saturation. However, the relatively poor agreement suggests that it may not be possible to obtain absolute values of venous oxygen saturation with this technique, other than to predict trends in cerebral oxygenation status in individual subjects (25).

- MRI Approaches

1) $T_2$, $T_2$* or $T_2$’ approaches

Attempts have been made to noninvasively assess blood oxygenation using MRI, based on the blood oxygen level dependent (BOLD) effect. These have involved either $T_2$, $T_2$* or $T_2$’ approaches since relaxation rate $T_2$, $T_2$* and $T_2$’ decrease along with an increase of the deoxyhemoglobin concentration. The dependence of T2 relaxation time of blood on the oxygenation state of hemoglobin was first demonstrated in blood samples (26, 27). Graham Wright and others (28-30) have made pioneering efforts to use $T_2$ of major blood vessels and blood in the heart and brain as a means to extract the blood’s oxygen saturation.$T_2$ methods rely on an in vitro calibration curve to translate $T_2$ measurements to venous oxygen saturation levels (28). $T_2$* based methods have been tried by Debaio Li and others (31-33). A similar $T_2$* approach for small partial volumed vessels has been proposed by Sedlacik et al (34,35).Both static spin dephasing and spin diffusion through the field inhomogeneity caused by the presence of paramagnetic deoxyhemoglobin cause blood signal loss in gradient-echo imaging. This suggests that blood T2* measured using a gradient-echo sequence is potentially more sensitive to hemoglobin oxygen saturation changes than T2, measured using a spin-echo sequence, because spin diffusion is the only major contributor to signal loss in spin-echo imaging (32). Weili Lin (36-38) and Yablonskiy (39,40) have used the theory from Yablonskiy and Haacke (41) to extract oxygen saturation and blood volume of the underlying capillary network using $T_2$' from a special multi-echo gradient echo/spin echo sequence (42,43). In the $T_2$-approach, the relaxation rate is quantified with a Carr-Purcell-Meiboom-Gill (CPMG)-based pulse sequence and it is assumed that $1/T_2$ scales as$(1 – Yv)^2$(44). $T_2$*, the time constant for signal decay from static dephasing due to local spatial magnetic field variations within and in the vicinity of erythrocytes, is typically obtained with a multi-echo gradient-echo (GRE) sequence.

2) MR susceptometry-based oximetry

MR susceptometry-based oximetry first proposed by Haacke et al (45) and later used by other groups (44,46-49) has also been applied to single vessels in an attempt to extract venous susceptibility and oxygen saturation from small veins in the brain (45,46)and major veins in the neck(44,47-49). Specifically, venous blood oxygen saturation is estimated by quantifying the intravascular bulk magnetic susceptibility relative to the surrounding tissue by exploiting the inherent paramagnetism of deoxyhemoglobin in erythrocytes. In MR susceptometry-based oximetry, a vessel is approximated as a long paramagnetic cylinder (length >> diameter) surrounded by a uniform medium. More detailed discussions about this method will be provided in Chapter 2.

3)$^{17}$O MR

$^{17}$O MR may be the sole MR approach available currently for direct measurement of CMRO2*in vivo*. $^{17}$O is the only stable oxygen isotope that can be detected by MR. The quadrupolar moment of $^{17}$O spin (I = 5/2) can interact with local electric field gradients, resulting in extremely short T1 and T2 relaxation times which are in the range of several milliseconds.$^{17}$O MR determines the cerebral metabolic rate of oxygen utilization (CMRO2) through monitoring the dynamic changes of metabolically generated $H_2{}^{17}O$ from inhaled $^{17}$O-labeled oxygen gas in the brain tissue. However, the natural abundance of $^{17}$O is only 0.037%, which is almost 30 times lower than that of $^{13}$C and 2700 times lower than that of $^{1}$H. Moreover, the magnetogyric ratio $\gamma$ of $^{17}$O, which is proportional to the Larmor frequency, is 7.4 times lower than that of $^{1}$H. This low inherent MR sensitivity and the expense in obtaining $^{17}$O are the main reasons for its infrequent use for *in vivo* MR studies, especially at relatively low magnetic fields, despite its great potential for providing unique and vital biological information (50).

## 1.3 Motivation of the Study

Measuring venous blood oxygen saturation (Yv) in the brain is very important for monitoring the oxygen extraction fraction (OEF) and the amount of oxygen getting to the tissue. Therefore, Yv provides important information on the physiological and pathological state of the brain. If we could provide a rapid noninvasive method for quantifying oxygen saturation, it would have profound impact on both neuroscience studies and clinic practice.

The sensitivity of the phase to the local susceptibility of the tissue makes it possible to estimate oxygen saturation using phase. Yv can, in theory, be extracted from the phase of a vessel making any angle to the field if it is large enough relative to the pixel size and the pristine phase information is not distorted. Hemoglobin is the primary blood oxygen carrier, and is composed of four protein (“globin”) subunits. Each protein subunit contains a heme molecule that consists of an iron atom (Fe 2+). When the iron atom is bound to oxygen, no unpaired electrons exist, and therefore oxyhemoglobin is diamagnetic. When the oxygen dissociates from the iron atom it leaves behind deoxyhemoglobin which has four unpaired electrons and is paramagnetic relative to the surrounding tissue. Therefore, the iron in deoxyhemoglobin in venous blood acts as an intrinsic contrast agent, causing $T_2$*-related losses in the magnitude image and a shift in the phase relative to surrounding tissues in the phase image caused by susceptibility differences. The oxygen in oxyhemoglobin shields the iron so the $T_2$* and susceptibility effects are only seen in venous blood. Therefore, susceptibility can be investigated to reveal information about oxygen saturation levels in blood. Hence, there has been a major interest in quantifying susceptibility in MRI in general, as it could lead to a unique quantitative tool and provide a novel contrast mechanism.

Mapping susceptibility from field perturbation data (which is directly related to the MR phase images) is a difficult inverse problem. There are a variety of approaches to tackle this problem, all with their own artifacts and reconstruction advantages and difficulties (51-69). One method (62) approached this issue by using a multiple orientation data acquisition approach to remove the singularities. Most methods involve a mathematical regularization. Simple threshold based regularization methods (56,60,63) have led to quantitative measurements that fall within 10% - 20% of the true susceptibility values (56) despite the fact that reconstruction artifacts remain. Generally, constrained regularizations (59,65,69) have shown good overall results, but they require longer reconstruction times and assumptions about the contrast in or near the object to be detected.

In this thesis, we propose a novel method, i.e. a regularized inverse filter, which combines thresholding and weighted smoothing to help alleviate the ill-posed problem of the inverse filter and which therefore can provide susceptibility maps of the whole brain efficiently. Based on this method, we also considered a key refinement, a k-space iterative approach to overcome problems which threshold-based methods have, i.e., severe streaking artifacts and underestimated susceptibility values, in order to produce improved accuracy for susceptibility maps. The regularized inverse filter plus the k-space iterative method will provide an almost artifact free susceptibility map (SM) with accurate susceptibilities. Since susceptibility reveals the information about the oxygen saturation level in blood, with an accurate SM, in theory, we should be able to quantify the oxygen saturation level in blood.

## 1.4 Overview of Thesis

In this thesis, we propose two algorithms related to susceptibility quantification which are the key to measuring the oxygen saturation level accurately. Each algorithm which we developed will conquer several particular issues in susceptibility quantification. These two algorithms can be merged to measure the oxygen saturation.

There are five chapters in this thesis. Chapter 1 gives the motivation for measuring oxygen saturation and its associated problems. Chapter 2 provides the background knowledge associated with this thesis, for instance, susceptibility, phase, the relationship between susceptibility and phase and the concept of susceptibility mapping. The main body of the thesis consists of Chapter 3 and Chapter 4. Each chapter addresses one algorithm, i.e. the regularized inverse filter and the k-space iterative method, which we developed. At the end, Chapter 5 provides conclusions and points out future directions.

In Chapter 3, we look into how to create an orientation-independent, 3D reconstruction of the veins in the brain using susceptibility mapping. High-resolution, high-pass filtered phase images usually used for susceptibility weighted imaging (SWI) were used as a source for local magnetic field behavior. These images were subsequently post-processed using a regularized inverse filter, we proposed, to generate SMs of the veins. Regularization and interpolation of the data in k-space of the phase images were used to reduce reconstruction artifacts. To understand the effects of artifacts, and to finetune the methodology, simulations of blood vessels were performed with and without noise. With sufficient resolution, major veins in the brain could be visualized with this approach. The usual geometry-dependent phase dipole effects are removed by this processing, leaving basically images of the veins. Different sized vessels show a different level of contrast depending on their partial volume effects. Smaller vessels show smaller values due to errors in the methodology and due to partial volume effects. Larger vessels show a bias toward a reduced susceptibility approaching 90% of the expected value. Limitations of the method and artifacts related to different sources of errors are demonstrated.

In Chapter 4, we propose a k-space iterative approach using geometric information as a constraint to overcome the ill-posed nature of the inverse filter in calculating local susceptibility and to improve susceptibility quantification of veins in the brain. Simulations are used to study the resulting accuracy of the method and its robustness in the presence of noise. *In-vivo* data are processed and analyzed using this method. Both simulations and *in-vivo* results show that most streaking artifacts inside the susceptibility map caused by the ill-defined inverse filter have been suppressed by the iterative approach. The bias toward lower mean susceptibility values inside vessels has been shown to decrease from around 10% to 2% when choosing an appropriate threshold value. This iterative method allows for quantification of susceptibility maps from a single-orientation acquisition. This method can be applied not only to veins but also other *in vivo* structures to generate potentially whole brain susceptibility maps without streaking artifacts.

## References

1. Magistretti PJ, Pellerin L. Cellular Mechanisms of Brain Energy Metabolism. Relevance to Functional Brain Imaging and to Neurodegenerative Disordersa. Annals of the New York Academy of Sciences. 1996 Jan 1;777(1):380–7.

2. Beaney RP, Lammertsma AA, Jones T, McKenzie CG, Halnan KE. Positron emission tomography for in-vivo measurement of regional blood flow, oxygen utilisation, and blood volume in patients with breast carcinoma. Lancet. 1984 Jan 21;1(8369):131–4.

3. Xu F, Ge Y, Lu H. Noninvasive quantification of whole-brain cerebral metabolic rate of oxygen (CMRO2) by MRI. Magn Reson Med. 2009 Jul;62(1):141–8.

4. Thorniley MS, Houston R, Wickramasinghe YA, Rolfe P. Application of near-infrared spectroscopy for the assessment of the oxygenation level of myoglobin and haemoglobin in cardiac muscle in vivo. Biochem. Soc. Trans. 1990 Dec;18(6):1195–6.

5. Thorniley MS, Livera LN, Wickramasinghe YA, Spencer SA, Rolfe P. The non-invasive monitoring of cerebral tissue oxygenation. Adv. Exp. Med. Biol. 1990;277:323–34.

6. Benaron DA, Benitz WE, Ariagno RL, Stevenson DK. Noninvasive methods for estimating in vivo oxygenation. Clin Pediatr (Phila). 1992 May;31(5):258–73.

7. Schelbert HR. Blood flow and metabolism by PET. Cardiol Clin. 1994 May;12(2):303–15.

8. Madsen PL, Secher NH. Near-infrared oximetry of the brain.Progress in Neurobiology. 1999 Aug;58(6):541–60.

9. Derdeyn CP. Positron Emission Tomography Imaging of Cerebral Ischemia. PET Clinics. 2007 Jan;2(1):35–44.

10. Khan N, Williams BB, Hou H, Li H, Swartz HM. Repetitive Tissue pO2 Measurements by Electron Paramagnetic Resonance Oximetry: Current Status and Future Potential for Experimental and Clinical Studies. Antioxidants & Redox Signaling. 2007 Aug;9(8):1169–82.

11. Torres Filho IP, Terner J, Pittman RN, Proffitt E, Ward KR. Measurement of Hemoglobin Oxygen Saturation Using Raman Microspectroscopy and 532-Nm Excitation. J Appl Physiol. 2008 Jun 1;104(6):1809–17.

12. Leenders KL, Frackowiak RSJ, Quinn N, Marsden CD. Brain energy metabolism and dopaminergic function in Huntington’s disease measured in vivo using positron emission tomography. Movement Disorders. 1986 Jan 1;1(1):69–77.

13. Tanaka M, Kondo S, Okamoto K, Hirai S. [Cerebral perfusion and oxygen metabolism in Parkinson’s disease: positron emission tomographic study using oxygen-15-labeled CO2 and O2]. Nippon Rinsho. 1997 Jan;55(1):218–21.

14. K I, H K, M K, E M. Decreased medial temporal oxygen metabolism in Alzheimer’s disease shown by PET. Journal of nuclear medicine : official publication, Society of Nuclear Medicine. 1996 Jul;37(7):1159.

15. Ge Y, Zhang Z, Lu H, Tang L, Jaggi H, Herbert J, et al. Characterizing brain oxygen metabolism in patients with multiple sclerosis with T2-relaxation-under-spin-tagging MRI. J. Cereb. Blood Flow Metab. 2012 Mar;32(3):403–12.

16. KETY SS, SCHMIDT CF. The effects of altered arterial tensions of carbon dioxide and oxygen on cerebral blood flow and cerebral oxygen consumption of normal young men. J. Clin. Invest. 1948 Jul;27(4):484–92.

17. Macmillan CSA, Andrews PJD. Cerebrovenous oxygen saturation monitoring: practical considerations and clinical relevance. Intensive Care Medicine. 2000;26(8):1028–36.

18. Sandra L. Schutz. (2001). Oxygen Saturation Monitoring by Pulse Oximetry. AACN Procedure manual for Critical Care, Fourth Edition

19. Powers WJ, Grubb RL, Darriet D, Raiehle ME. Cerebral Blood Flow and Cerebral Metabolic Rate of Oxygen Requirements for Cerebral Function and Viability in Humans.Journal of Cerebral Blood Flow & Metabolism. 1985 Dec 1;5(4):600–8.

20. Powers WJ. Cerebral hemodynamics in ischemic cerebrovascular disease.Annals of Neurology. 2004 Oct 8;29(3):231–40.

21. Ito H, Ibaraki M, Kanno I, Fukuda H, Miura S. Changes in cerebral blood flow and cerebral oxygen metabolism during neural activation measured by positron emission tomography: comparison with blood oxygenation level-dependent contrast measured by functional magnetic resonance imaging. Journal of Cerebral Blood Flow & Metabolism. 2005 Jan 19;25(3):371–7.

22. Mayberg TS, Lam AM. Jugular bulb oximetry for the monitoring of cerebral blood flow and metabolism.Neurosurg.Clin. N. Am. 1996 Oct;7(4):755–65.

23. Coplin WM, O’Keefe GE, Grady MS, Grant GA, March KS, Winn HR, et al. Thrombotic, infectious, and procedural complications of the jugular bulb catheter in the intensive care unit. Neurosurgery. 1997 Jul;41(1):101–107; discussion 107–109.

24. Daubeney PEF, Pilkington SN, Janke E, Charlton GA, Smith DC, Webber SA. Cerebral oxygenation measured by near-infrared spectroscopy: Comparison with jugular bulb oximetry. The Annals of Thoracic Surgery. 1996 Mar;61(3):930–4.

25. Tortoriello TA, Stayer SA, Mott AR, DEAN McKENZIE E, Fraser CD, Andropoulos DB, et al. A noninvasive estimation of mixed venous oxygen saturation using near-infrared spectroscopy by cerebral oximetry in pediatric cardiac surgery patients.Pediatric Anesthesia. 2005 Jun 1;15(6):495–503.

26. Thulborn KR, Waterton JC, Matthews PM, Radda GK. Oxygenation dependence of the transverse relaxation time of water protons in whole blood at high field.Biochim.Biophys.Acta. 1982 Feb 2;714(2):265–70.

27. Gomori JM, Grossman RI, Yu-Ip C, Asakura T. NMR relaxation times of blood: dependence on field strength, oxidation state, and cell integrity. J Comput Assist Tomogr. 1987 Aug;11(4):684–90.

28. Wright GA, Hu BS, Macovski A. Estimating oxygen saturation of blood in vivo with MR imaging at 1.5 T. Journal of Magnetic Resonance Imaging. 1991 May 1;1(3):275–83.

29. Oja JME, Gillen JS, Kauppinen RA, Kraut M, Zijl PCM van.Determination of Oxygen Extraction Ratios by Magnetic Resonance Imaging.Journal of Cerebral Blood Flow & Metabolism. 1999 Dec 1;19(12):1289–95.

30. Zijl PCM van, Eleff SM, Ulatowski JA, Oja JME, Traystman RJ, et al. Quantitative assessment of blood flow, blood volume and blood oxygenation effects in functional magnetic resonance imaging. Nature Medicine. 1998 Feb 1;4(2):159–67.

31. Chien D, Levin DL, Anderson CM. MR gradient echo imaging of intravascular blood oxygenation: T2* determination in the presence of flow. Magn Reson Med. 1994 Oct;32(4):540–5.

32. Li D, Wang Y, Waight DJ. Blood oxygen saturation assessment in vivo using T2* estimation. Magn Reson Med. 1998 May;39(5):685–90.

33. Li D, Waight DJ, Wang Y. In vivo correlation between blood T2* and oxygen saturation. J Magn Reson Imaging. 1998 Dec;8(6):1236–9.

34. Sedlacik J, Rauscher A, Reichenbach JR. Quantification of modulated blood oxygenation levels in single cerebral veins by investigating their MR signal decay. Z Med Phys. 2009;19(1):48–57.

35. Sedlacik J, Reichenbach JR. Validation of quantitative estimation of tissue oxygen extraction fraction and deoxygenated blood volume fraction in phantom and in vivo experiments by using MRI. Magn Reson Med. 2010 Apr;63(4):910–21.

36. An H, Lin W. Quantitative Measurements of Cerebral Blood Oxygen Saturation Using Magnetic Resonance Imaging. Journal of Cerebral Blood Flow & Metabolism. 2000 Aug 1;20(8):1225–36.

37. An H, Lin W. Cerebral oxygen extraction fraction and cerebral venous blood volume measurements using MRI: Effects of magnetic field variation. Magnetic Resonance in Medicine. 2002 May 1;47(5):958–66.

38. An H, Lin W, Celik A, Lee YZ. Quantitative measurements of cerebral metabolic rate of oxygen utilization using MRI: a volunteer study. NMR in Biomedicine. 2001 Nov 1;14(7-8):441–7.

39. He X, Yablonskiy DA. Quantitative BOLD: Mapping of human cerebral deoxygenated blood volume and oxygen extraction fraction: Default state. Magnetic Resonance in Medicine. 2007 Jan 1;57(1):115–26.

40. He X, Zhu M, Yablonskiy DA. Validation of oxygen extraction fraction measurement by qBOLD technique.Magnetic Resonance in Medicine. 2008 Oct 1;60(4):882–8.

41. Yablonskiy DA, Haacke EM. Theory of NMR signal behavior in magnetically inhomogeneous tissues: The static dephasing regime. Magnetic Resonance in Medicine. 1994 Dec 1;32(6):749–63.

42. Yablonskiy DA, Haacke EM. An MRI method for measuring T2 in the presence of static and RF magnetic field Inhomogeneities.Magnetic Resonance in Medicine. 1997 Jun 1;37(6):872–6.

43. Yablonskiy DA, Reinus WR, Stark H, Haacke EM. Quantitation of T2′ anisotropic effects on magnetic resonance bone mineral density measurement. Magnetic Resonance in Medicine. 1997 Feb 1;37(2):214–21.

44. Langham MC, Magland JF, Epstein CL, Floyd TF, Wehrli FW. Accuracy and precision of MR blood oximetry based on the long paramagnetic cylinder approximation of large vessels. Magnetic Resonance in Medicine. 2009 Aug 1;62(2):333–40.

45. Haacke EM, Lai S, Reichenbach JR, Kuppusamy K, Hoogenraad FGC, Takeichi H, et al. In vivo measurement of blood oxygen saturation using magnetic resonance imaging: A direct validation of the blood oxygen level-dependent concept in functional brain imaging. Human Brain Mapping. 1997 Jan 1;5(5):341–6.

46. Liu Y, Pu Y, Fox PT, Gao J. Quantification of dynamic changes in cerebral venous oxygenation with MR phase imaging at 1.9 T. Magnetic Resonance in Medicine. 1999 Feb 1;41(2):407–11.

47. Fernández-Seara MA, Techawiboonwong A, Detre JA, Wehrli FW. MR susceptometry for measuring global brain oxygen extraction. Magnetic Resonance in Medicine. 2006 May 1;55(5):967–73.

48. Langham MC, Floyd TF, Mohler III ER, Magland JF, Wehrli FW. Evaluation of Cuff-Induced Ischemia in the Lower Extremity by Magnetic Resonance Oximetry.Journal of the American College of Cardiology. 2010 Feb 9;55(6):598–606.

49. Langham MC, Magland JF, Floyd TF, Wehrli FW. Retrospective correction for induced magnetic field inhomogeneity in measurements of large-vessel hemoglobin oxygen saturation by MR susceptometry. Magnetic Resonance in Medicine. 2009 Mar 1;61(3):626–33.

50. Zhu X, Zhang N, Zhang Y, Zhang X, Ugurbil K, Chen W. In vivo17O NMR approaches for brain study at high field. NMR in Biomedicine. 2005 Apr 1;18(2):83–103.

51. Deville G, Bernier M, Delrieux JM. NMR multiple echoes observed in solid ^{3}He. Phys. Rev. B. 1979 Jun 1;19(11):5666–88.

52. Haacke EM, Cheng NYC, House MJ, Liu Q, Neelavalli J, Ogg RJ, et al. Imaging iron stores in the brain using magnetic resonance imaging. Magnetic Resonance Imaging. 2005 Jan;23(1):1–25.

53. Koch KM, Papademetris X, Rothman DL, de Graaf RA. Rapid calculations of susceptibility-induced magnetostatic field perturbations for in vivo magnetic resonance. Phys Med Biol. 2006 Dec 21;51(24):6381–402.

54. de Rochefort L, Brown R, Prince MR, Wang Y. Quantitative MR susceptibility mapping using piece-wise constant regularized inversion of the magnetic field. Magn Reson Med. 2008 Oct;60(4):1003–9.

55. Cheng Y-CN, Neelavalli J, Haacke EM. Limitations of calculating field distributions and magnetic susceptibilities in MRI using a Fourier based method. Phys Med Biol. 2009 Mar 7;54(5):1169–89.

56. Wharton S, Schäfer A, Bowtell R. Susceptibility mapping in the human brain using threshold-based k-space division. Magn Reson Med. 2010 May;63(5):1292–304.

57. Wharton S, Bowtell R. Whole-brain susceptibility mapping at high field: a comparison of multiple- and single-orientation methods. Neuroimage. 2010 Nov 1;53(2):515–25.

58. Schweser F, Deistung A, Lehr BW, Reichenbach JR. Differentiation between diamagnetic and paramagnetic cerebral lesions based on magnetic susceptibility mapping. Med Phys. 2010 Oct;37(10):5165–78.

59. Kressler B, de Rochefort L, Liu T, Spincemaille P, Jiang Q, Wang Y. Nonlinear regularization for per voxel estimation of magnetic susceptibility distributions from MRI field maps. IEEE Trans Med Imaging. 2010 Feb;29(2):273–81.

60. Shmueli K, de Zwart JA, van Gelderen P, Li T, Dodd SJ, Duyn JH. Magnetic susceptibility mapping of brain tissue in vivo using MRI phase data. Magnetic Resonance in Medicine. 2009 Dec 1;62(6):1510–22.

61. Schäfer A, Wharton S, Gowland P, Bowtell R. Using magnetic field simulation to study susceptibility-related phase contrast in gradient echo MRI. Neuroimage. 2009 Oct 15;48(1):126–37.

62. Liu T, Spincemaille P, de Rochefort L, Kressler B, Wang Y. Calculation of susceptibility through multiple orientation sampling (COSMOS): a method for conditioning the inverse problem from measured magnetic field map to susceptibility source image in MRI. Magn Reson Med. 2009 Jan;61(1):196–204.

63. Haacke EM, Tang J, Neelavalli J, Cheng YCN. Susceptibility mapping as a means to visualize veins and quantify oxygen saturation.J Magn Reson Imaging. 2010 Sep;32(3):663–76.

64. Li W, Wu B, Liu C. Quantitative susceptibility mapping of human brain reflects spatial variation in tissue composition. Neuroimage. 2011 Apr 15;55(4):1645–56.

65. Liu T, Liu J, de Rochefort L, Spincemaille P, Khalidov I, Ledoux JR, et al. Morphology enabled dipole inversion (MEDI) from a single-angle acquisition: comparison with COSMOS in human brain imaging. Magn Reson Med. 2011 Sep;66(3):777–83.

66. Li L, Leigh JS. Quantifying arbitrary magnetic susceptibility distributions with MR. Magn Reson Med. 2004 May;51(5):1077–82.

67. Marques JP, Bowtell R. Application of a Fourier-based method for rapid calculation of field inhomogeneity due to spatial variation of magnetic susceptibility. Concepts in Magnetic Resonance Part B: Magnetic Resonance Engineering. 2005 Apr 1;25B(1):65–78.

68. Salomir R, de Senneville BD, Moonen CT. A fast calculation method for magnetic field inhomogeneity due to an arbitrary distribution of bulk susceptibility. Concepts in Magnetic Resonance Part B: Magnetic Resonance Engineering. 2003 Jan 1;19B(1):26–34.

69. de Rochefort L, Liu T, Kressler B, Liu J, Spincemaille P, Lebon V, et al. Quantitative susceptibility map reconstruction from MR phase data using bayesian regularization: validation and application to brain imaging. Magn Reson Med. 2010 Jan;63(1):194–206.

# Chapter 2: Susceptibility, MRI Phase and Susceptibility Mapping[1]

---

[1] Most of the contents of this chapter have been adapted from Haack et al, Magnetic Resonance Imaging: Physical Principles and Sequence Design. 1st Ed. Wiley-Liss;1999, and Haacke et al, Susceptibility Weighted Imaging in MRI: Basic Concepts and Clinical Applications. 1st Ed. Wiley-Blackwell, 2011.

## 2.1 Introduction of Susceptibility

Magnetic susceptibility is a basic material property that measures the ability of a substance to get magnetized when placed in an external magnetic field. It may also be characterized as being the measure of the extent to which a substance modifies the strength of the magnetic field passing through it. The internal susceptibility differences between tissues can cause image distortion and loss of signal, especially T2* losses in gradient-echo imaging. On the other hand, susceptibility is also another intrinsic tissue property and local variations in susceptibility can be useful in identifying special properties or states of the tissue of interest. Quantifying magnetic susceptibility of biological tissues could have very important clinical implications, such as differentiating a hemorrhagic lesion as acute or chronic, identifying calcifications, or measuring oxygen saturation in the blood which is the focus of this thesis.

### 2.1.1 Bulk Magnetic Fields

When an external uniform magnetic $\vec{B}_0 = \mu_0\vec{H}_0$ is applied to a substance, the actual field $\vec{B}$ inside the material is given by

$$\vec{B} = \mu_0 (\vec{H} + \vec{M}) \qquad [1]$$

where $\vec{B}$ is the magnetic field measured in Tesla (T), $\vec{H}$ is the applied magnetic field measured in Ampere/meter (A/m), $\vec{M}$ is the permanent magnetization or the induced magnetization measured in Ampere/meter (A/m) and $\mu_0$is the absolute permeability of free space ($4\pi\times 10^{-7}$) with units of T m/A. When a material is not permanently magnetized, i.e., $\vec{M}$ is not a constant, the induced magnetization $\vec{M}$ inside the material is related to the $\vec{H}$ field by a constant susceptibility $\chi$ through

$$\vec{M} = \chi\vec{H} \quad [2]$$

Thus, equation [1] can be rewritten as

$$\vec{B} = \mu_0(1+\chi)\vec{H} \quad \text{or} \quad \vec{B} = \left(\frac{1+\chi}{\chi}\right)\mu_0\vec{M} \quad [3]$$

The field distribution outside the material will also be perturbed due to the fact that the object has an induced magnetization. The solution for field perturbation outside the object is a vector function of the induced magnetization $\vec{M}$ and depends on the shape and volume of the object:

$$\vec{B}_{\text{out}}(\text{r}) = \vec{B}_0 + f(\vec{M}, \text{object shape, object size}, \vec{r}) \qquad [4]$$

Where $f$ denotes “function of”, $\vec{B}_0$ is the external magnetic field, and $\vec{B}_{\text{out}}$ is the field at a point $\vec{r}$ outside the object.

MR measurements are sensitive to the magnetic field manifested in frequency through the Larmor equation (a right handed system)

$$\omega = -\gamma \cdot B \qquad [5]$$

where $\omega$ is the precession angular frequency, $\gamma$ is the gyromagnetic ratio of the proton, and B is the actual field experienced by a proton. This change in frequency caused by changes in susceptibility and changes in the local magnetic field are what provide us with the ammunition to measure susceptibility information with MR.

### 2.1.2 Diamagnetism, Paramagnetism and Ferromagnetism

Based on the macroscopic behavior under the influence of an external magnetic field, various substances are broadly classified into diamagnetic, paramagnetic, and ferromagnetic materials (1). From equation [3], if the susceptibility $\chi$ is positive ($\chi>0$), the material or the object is considered as paramagnetic. If $\chi$ is negative ($\chi<0$), the material is diamagnetic. In the ferromagnetic case, $\chi >>1$. For permanent magnetic or ferromagnetic substances, equation [3] is not suitable, so the original equation [1] should be used. The value of $\chi$ is given in ppm (parts per million). Water is diamagnetic and has a susceptibility value of $\chi_{water} \approx -9.05$ ppm. Human tissues tend to be mostly water by weight. As a consequence, almost all soft tissues in the body are diamagnetic in nature. For most biological tissues, $\chi << 1$.In MRI, the term “paramagnetic” or “diamagnetic” is used relative to the susceptibility of water. For instance, fully deoxygenated whole blood (assuming Hct=0.45) has a magnetic susceptibility of -7.9ppm.When it compared to water ($\chi_{water} \approx -9.05$ ppm), it is paramagnetic.

## 2.2 Susceptibility and Oxygenation Level

As the oxygen content in blood changes, the local susceptibility in the blood changes accordingly. The source of this dependence has been shown to be the unshielded iron in hemoglobin (red blood cells). Blood can be approximated as a two-compartment system containing both plasma and red blood cells (they together constitute about 99% of whole blood by volume). Hematocrit (Hct) is the fraction of the volume of packed red blood cells in the blood. Typically, Hct is about 0.4 for women and 0.45 for men. Much of the iron in the blood is in the hemoglobin in one of two states: oxyhemoglobin or deoxyhemoglobin. Oxyhemoglobin is formed during physiological respiration when oxygen binds to the heme component of the protein hemoglobin in red blood cells. Deoxygenated hemoglobin is the form of hemoglobin without bound oxygen. Oxyhemoglobin is diamagnetic due to the lack of unpaired electrons and deoxyhemoglobin is paramagnetic due to unpaired electrons.

Susceptibility of a red blood cell depends on the oxygen saturation of hemoglobin within it. If we neglect the slight paramagnetic susceptibility contribution of dissolved oxygen in plasma, we can model the susceptibility of whole blood as:

$$\chi_{blood} = \mathrm{Hct}\,(Y_v\,\chi_{oxy} + (1 - Y_v)\,\chi_{deoxy}) + (1-\mathrm{Hct})\chi_{plasma} \qquad [6]$$

where Hct stands for hematocrit, $\chi_{plasma}$ is the susceptibility of plasma, and $\chi_{oxy}$ and $\chi_{deoxy}$ are susceptibilities of a red blood cell with 100% ($Y_v$=1) and 0% ($Y_v$=0) oxygen saturation.

The change in blood susceptibility from fully oxygenated to deoxygenated blood has been measured to be $\chi_{do} = \chi_{deoxy} - \chi_{oxy} = 4\pi\cdot(0.27)$ ppm per unit Hct (2). It has been observed that arterial (oxygenated) blood appears to have the same susceptibility as the surrounding tissue. Then, if $\chi_{plasma}$ is close to $\chi_{oxy}$, equation [6] leads to the practical form

$$\chi_{blood,relative} = \chi_{blood} - \chi_{surr} = \chi_{blood} - \chi_{oxy} = 4\pi\cdot(0.27)\cdot\mathrm{Hct}\,(1 - Y_v)\ \mathrm{ppm} \qquad [7]$$

The dependence of magnetic susceptibility of blood on its oxygenation state could help us to measure the oxygen saturation level ($Y_v$) and therefore metabolic state of the underlying tissue.

## 2.3 MRI Phase and Its Relationship to Susceptibility

### 2.3.1 Introduction of MRI Phase

In MRI, phase can be defined as the changing orientation of the magnetization vector in the transverse plane. Quantitatively, it depends on the product of time and angular velocity of the transverse magnetization vector, as well as on an initial phase constant $\varphi_0$ that defines the value of phase at the time origin. Hence, phase can be defined by the following expression:

$$\varphi(t) = \omega \cdot t + \varphi_0 \qquad [8]$$

Assuming x-y to represent the coordinates of the transverse plane, the transverse magnetization vector M can be written as

$$\vec{M} = |M| \cdot e^{i\varphi(r,t)} = |M| \cdot (\cos\varphi + i \sin\varphi) \qquad [9]$$

where $|M| = \sqrt{x^2 + y^2}$ is the modulus or magnitude of the vector (x, y) and φ is the phase, that is, the angle between the x axis and the vector (x, y) measured counterclockwise and in radians. The phase angle φ can be given by the inverse tangent

$$\varphi = \tan^{-1}(y/x) \qquad [10]$$

### 2.3.2 Relationship between Phase and Susceptibility

Different tissues and substructures may have different magnetic susceptibilities. In the magnetic field of an MRI scanner, these susceptibility differences cause variations in the local magnetic field strength. This leads to small changes in the resonance frequency of the spins excited and detected by MRI and results in phase differences in gradient-echo MR images. Phase at a given point in an MR image is sensitive to the local field perturbation (with respect to the uniform applied field $B_o$), rather than the absolute field. So phase $\varphi$ is given by

$$\varphi (t) = -\gamma \cdot \Delta B \cdot t \qquad [11]$$

where $\Delta B$ is the field perturbation in $B_o$ and $t$ is the time at which signal is acquired. Under the situation of structures with different susceptibilities embedded within each other, it is the difference in their susceptibility, $\Delta\chi$, that becomes the important parameter determining the field perturbation. In other words, $\Delta B = Bo \cdot \Delta\chi \cdot g$ where g is a constant depending on the object's geometry. Within the human body, small relative susceptibility differences between adjacent tissues cause a unique phase signature in the MR signal.

### 2.3.3 Limitation of Phase

Phase images of the brain generated using gradient-echo techniques at high field strength show excellent contrast related to the variation of magnetic susceptibility across tissues (3–8). However, extraction of accurate anatomic information from phase data is made difficult by the nonlocal relationship between the field perturbation that gives rise to the phase changes and the associated susceptibility distribution (9), which means that phase variation occurs remotely from underlying anatomic structures (7). Additionally, in brain imaging the measured phase variation depends on the angle that the head makes with respect to the applied magnetic field (7, 9). These limitations provide a strong motivation for attempting to map directly the magnetic susceptibility variation underlying the induced field and phase variation.

## 2.4 Susceptibility Mapping

### 2.4.1 Introduction of Susceptibility Mapping

A novel technique, referred to as quantitative susceptibility mapping, overcomes the non-local relationship between magnetic field perturbation and susceptibility. Here, phase data are processed to extract the underlying magnetic susceptibility distribution, resulting in a novel quantitative anatomical contrast of an intrinsic physical tissue property. Susceptibility maps (SM) are expected to enable quantitative examination of changes in magnetic tissue properties *in vivo* due to, e.g., elevated iron storage or local blood oxygen saturation. In general, the key feature for susceptibility mapping is to use phase information (which is linearly related to the local field changes) for enhanced contrast and for local susceptibility information. SMs overcome the major disadvantages of phase images, whose contrast vary with orientation and are non-local. In SMs, the contrast of cortical layers is more consistent than in the phase images and is independent of the structures' orientation relative to $B_o$. Non-local contrast variation in phase images, caused by regions with different susceptibility values, is also mitigated by susceptibility SMs.

Accurate MR-based susceptibility quantification would have many applications, beside quantification of blood oxygen saturation, it could be used to investigate the relationship between tissue iron content and progression of neurodegenerative diseases such as Parkinson’s disease, Huntington's disease and multiple sclerosis as well as to accurately measure the concentration of contrast agents *in vivo*.

### 2.4.2 Susceptibility Map Calculation

According to Equation [3], the magnetic induction $\vec{B}$ determines the local precession frequency and is given by $\vec{B} = \mu_0(1+\chi)\vec{H}$, any spatial variation in $\chi$ is also reflected in the spatial variation of the Larmor frequency (see Equation [5]). Therefore, it should be possible to relate directly the spatial variation of susceptibility to the expected field. This is indeed readily possible for objects with simple geometries, such as cylinders, spheres, or plates. The problem, however, becomes more intricate for more complex susceptibility distributions, for which it is usually necessary to use numerical methods. Quite recently, efforts have been undertaken to calculate magnetic field perturbations via Fourier analysis of heterogeneous magnetic susceptibility distributions (9, 10). Based on these approaches, it may become possible to calculate tissue susceptibility from phase images, which, in turn, would be highly beneficial since magnetic susceptibility is an intrinsic tissue property that reflects tissue composition more closely than the phase image. In this section, a susceptibility calculation using a Fourier transform approach will be discussed based on the simple geometry for a cylinder.

#### 2.4.2.1 SM Calculation Using a Numerical Model

Using the boundary conditions for the induced magnetization distribution (which factors in the object's shape and size), solutions for the fields inside and outside the object can be obtained (11). Analytically solving these equations for objects with some structural symmetry like a sphere or a cylinder is relatively easy. It is instructive to look at field perturbation solutions for uniform materials taken in certain standard symmetric geometrics like a sphere or a cylinder to get a feel for the nature of the field distortions/perturbations that we can expect in MR imaging. For example, sinuses might be modeled as spheres and blood vessels as long cylinders. Here, we only focus on a cylindrical model, since the model of an infinitely long, homogeneous magnetic cylinder is often used to describe a straight section of a single vessel.

Since the external uniform magnetic field, $B_o$, is applied along the z-direction, the objects primarily get magnetized along the z-direction, $\vec{M}_z$, with $\vec{M}_x$ and $\vec{M}_y$, being negligible. Furthermore, since $\chi \ll 1$ for most biological tissues, from Equation [3], we can approximate $\vec{M}_z$ as $(\chi/\mu_o)\vec{B}_o$. Given these conditions, assuming that the objects are in vacuum, solving for $\vec{B}$ inside and outside by applying the proper boundary conditions (11) then yields the expressions for the magnetic field inside and outside an infinitely long cylinder as following (1).

$$\vec{B}_{in} = \vec{B}_o + \frac{\chi\vec{B}o}{6} \cdot (3cos^2\theta - 1)[12]$$

$$\vec{B}_{out} = \vec{B}_o + \frac{\chi\vec{B}o}{2} \cdot \frac{a^2}{|r|^2} sin^2\theta cos2\phi[13]$$

where $\theta$ is the angle that the long axis of the cylinder makes with the main magnetic field $\vec{B}_o$, $\Phi$ is the polar angle subtended by $r$ on the plane perpendicular to the long axis of the cylinder; $r$ is the position vector of the point of observation; and $a$ is the radius of the cylinder.

If a cylinder is embedded in some external medium or compartment that has a finite shape and susceptibility value, these field equations are slightly modified. The term $\chi$ is replaced by $\Delta\chi = (\chi_{\text{cylinder}} - \chi_{\text{outside compartment}})$ and an additional field term that is dependent on the global geometry of the outer compartment is added.

We know $\varphi(t) = -\gamma \cdot \Delta B \cdot t$ (Equation [11], phase is sensitive to the local field perturbation. Thus, from Equation [12], the susceptibility $\Delta\chi$ can be obtained from phase and $Y_v$ values. This method is also called magnetic resonance oximetry (12) which was proposed by Haacke et al in 1997 and later used by other groups(14–18) to calculate the oxygen saturation level $Y_v$ where:

$$Y_v = \left[1 - \frac{2|\Delta\varphi|}{\gamma \Delta\chi_{do} Bo\left(cos^2\theta - \frac{1}{3}\right)Hct}\right] \times 100\% \qquad [14]$$

and $\Delta\varphi$ here is the average phase difference between intravascular blood and surrounding tissue.

In theory, phase variations can be used as a source of information about oxygen saturation level ($Y_v$). If we know the individual susceptibilities ($\Delta\chi$) of the hemoglobin components and the Hct, we can determine the absolute oxygen saturation $Y_v$ from the phase ($\Delta\varphi$).

### 2.4.2.2 SM Calculation Using Field Maps

As mentioned above, for complex susceptibility distributions, it is usually necessary to use numerical methods. Efforts have been undertaken to calculate magnetic field perturbations via Fourier analysis of heterogeneous magnetic susceptibility distributions (9,10). Based on these approaches, it may become possible to calculate tissue susceptibility from phase images.

When an object with a certain magnetic susceptibility distribution, $\chi$(r), is placed in an external magnetic fieldBo, the resulting magnetic field, $\vec{B}(\vec{r})$ at any position r isgiven by:

$$\vec{B}(\vec{r}) = \vec{B}\mathrm{o} + \frac{\mu_o}{4\pi}\int_{V'} \left\{\frac{3\vec{M}(\vec{r}\,')\cdot(\vec{r}-\vec{r}\,')}{|\vec{r}-\vec{r}\,'|^5}(\vec{r}-\vec{r}\,') - \frac{\vec{M}(\vec{r}\,')}{|\vec{r}-\vec{r}\,'|^3}\right\} \mathrm{d}V' \qquad [15]$$

where$\vec{M}(\vec{r})$ is the induced magnetization distribution ofthe object. In the case of MR experiments, the externalapplied magnetic field Bo is many orders of magnitude larger in one direction, assumed to be the z direction, than in the other two orthogonal directions. Taking this into account, and observing that the second term in Equation[16] is a convolution(9,18,19), this term can be Fourier-transformed into a simple product relation in the spatial frequency domain(generally referred to as k-space) to give:

$$\vec{B}_{dz}(\vec{k}) = \mu_o \vec{M}_z(\vec{k})\left(\frac{1}{3} - \frac{k_z^2}{K^2}\right) \qquad [16]$$

Here $k_x$, $k_y$, and $k_z$ are the coordinates in k-space and $K^2 = k_x^2 + k_y^2 + k_z^2$, $M_z(k)$ is the Fourier transform of the magnetization distribution of the object along the z direction and this spatially varying field $B_{dz}(r)$, which is the Fourier transform of $B_{dz}(k)$, gives rise to the spatially-varying phase seen in a gradient echo MR experiment. Since the susceptibilities of biological tissues are typically much less than unity, the magnetization of the object is $M_z(r) = \chi(r) \cdot B_o/\mu_o$ and hence $M_z(k) = FT(\chi(r)) \cdot (B_o/\mu_o)$, where FT stands for Fourier transformation. Thus the phase due to a spatially-varying field $B_{dz}(r)$, which itself arises from the presence of the susceptibility distribution $B_{dz}(r)$, can be calculated from:

$$\phi(\vec{r}) = -\gamma \vec{B}_{dz}(\vec{r}) TE = -\gamma B_o TE \cdot FT^{-1}\left[FT\left(\chi(\vec{r})\right) \cdot \left(\frac{1}{3} - \frac{k_z^2}{K^2}\right)\right] \qquad [17]$$

Equation [17] offers a simple, fast, and powerful means for calculating the field deviation due to the presence of a known $\chi(r)$ in an otherwise uniform field Bo. It is important to note here that Equations [16]and [17] are derived under the assumption that Bo is the predominant magnetic field and that the $B_{dz}$ field does not affect the magnetization of the object. The amazing element of this transformation is that it appears to require no *a priori* knowledge of the shape of the object. Now if an inverse relation between susceptibility and phase could be obtained, that is, if it were possible to predict the susceptibility distribution from phase images, it would be of great scientific and clinical significance. A crude but straightforward approach to predict the SM is given by the inverse of the above filter in Equation [17](20)

$$\chi(\vec{r}) = FT^{-1}\left[FT\left(\frac{\phi(\vec{r})}{-\gamma BoTE}\right)\left(\frac{1}{\frac{1}{3} - \frac{k_z^2}{K^2}}\right)\right] \qquad [18]$$

The main challenge in creating SMs from phase data is the ill-posed nature of the process of inversion. The reason for using the Fourier-based method is that the relationship between the field perturbation and the magnetic susceptibility distribution becomes simple and local in the Fourier domain. However, when inverting this relationship to obtain the susceptibility in terms of the field variation a problem arises, since the denominator, $\frac{1}{3} - \frac{k_z^2}{K^2}$, of the resulting expression (Equation [18]) tends to zero over two conical surfaces in k-space. These surfaces lie at the magic angle to the direction of the main magnetic field and its reflection. Without careful conditioning the resulting division-by-zero gives rise to artifacts in the calculated susceptibility distribution.

In Chapter 3 and Chapter 4 in this thesis, a regularized inverse filter and a k-space iterative method will be proposed to deal with the ill-posed problem of the inverse filter to provide improved accuracy and almost artifact free SMs.

## Reference

1. Haacke EM, Brown RW, Thompson MR, Venkatesan R. Magnetic Resonance Imaging: Physical Principles and Sequence Design. 1st ed. Wiley-Liss; 1999.
2. Spees WM, Yablonskiy DA, Oswood MC, Ackerman JJ. Water proton MR properties of human blood at 1.5 Tesla: magnetic susceptibility, T(1), T(2), T*(2), and non-Lorentzian signal behavior. Magn Reson Med. 2001 Apr;45(4):533–42.
3. Duyn JH, van Gelderen P, Li T-Q, de Zwart JA, Koretsky AP, Fukunaga M. High-field MRI of brain cortical substructure based on signal phase. Proc. Natl. Acad. Sci. U.S.A. 2007 Jul 10;104(28):11796–801.
4. Haacke EM, Cheng NYC, House MJ, Liu Q, Neelavalli J, Ogg RJ, et al. Imaging iron stores in the brain using magnetic resonance imaging. Magn Reson Imaging. 2005 Jan;23(1):1–25.
5. Koopmans PJ, Manniesing R, Niessen WJ, Viergever MA, Barth M. MR venography of the human brain using susceptibility weighted imaging at very high field strength. MAGMA. 2008 Mar;21(1-2):149–58.
6. Deistung A, Rauscher A, Sedlacik J, Stadler J, Witoszynskyj S, Reichenbach JR. Susceptibility weighted imaging at ultrahigh magnetic field strengths: theoretical considerations and experimental results. Magn Reson Med. 2008 Nov;60(5):1155–68.
7. Schäfer A, Wharton S, Gowland P, Bowtell R. Using magnetic field simulation to study susceptibility-related phase contrast in gradient echo MRI. Neuroimage. 2009 Oct 15;48(1):126–37.
8. Haacke EM, Mittal S, Wu Z, Neelavalli J, Cheng Y-CN. Susceptibility-weighted imaging: technical aspects and clinical applications, part 1. AJNR Am J Neuroradiol. 2009 Jan;30(1):19–30.
9. Marques JP, Bowtell R. Application of a Fourier-based method for rapid calculation of field inhomogeneity due to spatial variation of magnetic susceptibility. Concepts in Magnetic Resonance Part B: Magnetic Resonance Engineering. 2005 Apr 1;25B(1):65–78.
10. Salomir R, de Senneville BD, Moonen CT. A fast calculation method for magnetic field inhomogeneity due to an arbitrary distribution of bulk susceptibility. Concepts in Magnetic Resonance Part B: Magnetic Resonance Engineering. 2003 Jan 1;19B(1):26–34.
11. Edelstein WA, Hutchison JM, Johnson G, Redpath T. Spin warp NMR imaging and applications to human whole-body imaging. Phys Med Biol. 1980 Jul;25(4):751–6.

12. Haacke EM, Lai S, Yablonskiy DA, Lin W. In vivo validation of the bold mechanism: A review of signal changes in gradient echo functional MRI in the presence of flow. International Journal of Imaging Systems and Technology. 1995 Jun 1;6(2-3):153–63.

13. Liu Y, Pu Y, Fox PT, Gao J. Quantification of dynamic changes in cerebral venous oxygenation with MR phase imaging at 1.9 T. Magnetic Resonance in Medicine. 1999 Feb 1;41(2):407–11.

14. Fernández-Seara MA, Techawiboonwong A, Detre JA, Wehrli FW. MR susceptometry for measuring global brain oxygen extraction. Magnetic Resonance in Medicine. 2006 May 1;55(5):967–73.

15. Wright GA, Hu BS, Macovski A. Estimating oxygen saturation of blood in vivo with MR imaging at 1.5 T. Journal of Magnetic Resonance Imaging. 1991 May 1;1(3):275–83.

16. Langham MC, Magland JF, Epstein CL, Floyd TF, Wehrli FW. Accuracy and precision of MR blood oximetry based on the long paramagnetic cylinder approximation of large vessels. Magnetic Resonance in Medicine. 2009 Aug 1;62(2):333–40.

17. Langham MC, Magland JF, Floyd TF, Wehrli FW. Retrospective correction for induced magnetic field inhomogeneity in measurements of large-vessel hemoglobin oxygen saturation by MR susceptometry. Magnetic Resonance in Medicine. 2009 Mar 1;61(3):626–33.

18. Deville G, Bernier M, Delrieux JM. NMR multiple echoes observed in solid ^{3}He. Phys. Rev. B. 1979 Jun 1;19(11):5666–88.

19. Enss T, Ahn S, Warren WS. Visualizing the dipolar field in solution NMR and MR imaging: three-dimensional structure simulations. Chemical Physics Letters. 1999 May 14;305(1–2):101–8.

20. Haacke EM, Cheng NYC, House MJ, Liu Q, Neelavalli J, Ogg RJ, et al. Imaging iron stores in the brain using magnetic resonance imaging. Magnetic Resonance Imaging. 2005 Jan;23(1):1–25.

# Chapter 3: Susceptibility Mapping as a Means to Visualize Veins and Quantify Oxygen Saturation[2]

---

[2] Most of the contents of this chapter have been adapted from Haacke EM, Tang J, Neelavalli J, Cheng YC. Susceptibility mapping as a means to visualize veins and quantify oxygen saturation. J Magn Reson Imaging 2010; 32: 663-676.

## 3.1 Introduction

Susceptibility weighted imaging (SWI) has been used for some time as a means to enhance venous signal using high pass filtered phase images (1,2). The special image created by SWI processing relies on an asymmetric voxel aspect ratio. Therefore, when SWI is collected with high resolution isotropic data, the conventional processing will fail. To overcome this problem, we propose using a form of susceptibility mapping to produce an image of veins from SWI phase data (1). Such a map would make it easier to image venous vessels independent of their size and orientation, which we refer to here as susceptibility mapping of veins.

The ability to quantify local magnetic susceptibility is tantamount to being able to measure the amount of calcium or iron in the body whether it is calcium in breast (3)or iron in the form of non-heme iron (such as ferritin or hemosiderin) or heme iron (de-oxyhemoglobin). In the last few years, there have been a number of papers discussing different methods for doing this using a fast Fourier transform approach (4-10). All of these methods are based on the simple expression in k-space for analyzing distant dipolar fields from a given source of susceptibility distributions first given by Deville et al (11) in 1979. One of the methods utilizes the inverse of the Green's function (8). This is, however, fraught with difficulties as it is an ill-posed problem due to singularities in the inverse of the Green's function. To this end, different groups have tried regularization or multiple scans acquired with the object being rotated between scans (8, 9). In this chapter, we show that good quality magnetic source images or susceptibility maps (SM) of the veins in the brain can be obtained when the inverse is regularized and other sources of phase noise are removed.

## 3.2 Materials and Methods

### Inverse Filter Regularization

To reconstruct the susceptibility distribution, a regularized inverse filter, $g^{-1}(\mathbf{k})$, was applied to the Fourier transform of the high pass filtered phase image. The forward filter is defined by:

$$g(\mathbf{k}) = 1/3 - k_z^2/|\mathbf{k}|^2 \qquad [1]$$

where $k_x$,$k_y$,$k_z$ denote the coordinates in k-space and $|\mathbf{k}|^2 = k_x^2 + k_y^2 + k_z^2$. The filter $g(\mathbf{k})$ goes to zero when $2k_z^2 = k_x^2 + k_y^2$, making $g^{-1}(\mathbf{k})$ undefined (we refer to these $k_z$ values which satisfy this equation as $k_{zo}$). Hence, to reconstruct the susceptibility distribution, a regularized version of the inverse filter $g^{-1}(\mathbf{k})$ is applied to the Fourier transform of the unwrapped and background removal/high pass filtered phase image, $\varphi(\mathbf{k})$. It should be noted here that "k-space" in this chapter refers to the Fourier or frequency domain of unwrapped/high pass filtered phase images (i.e., obtained by directly taking their discrete Fourier transform), rather than the usual acquired k-space data in MRI.

In our approach to this problem, we regularize $g^{-1}(\mathbf{k})$ as follows. First, we restrict $g(\mathbf{k})$ to have a minimum value $a$ so that its inverse remains well defined. That is, for any $\mathbf{k}$ where $|\, g(\mathbf{k}) \,| < a$, $g(\mathbf{k})$ is set to $-a$ or $a$ depending on the sign of $g(\mathbf{k})$ (i.e., $g^{-1}(\mathbf{k})$ is set to a minimum of $-1/a$ or a maximum of $1/a$). This first step prevents $g^{-1}(\mathbf{k})$ from becoming too large and enhancing noise points near singularities. Second, the inverse, $g^{-1}(\mathbf{k})$, is brought smoothly to zero as $\mathbf{k}$ approaches $k_{zo}$ such that the discontinuity at $k_z = k_{zo}$ is removed. This smoothing is accomplished by multiplying $g^{-1}(\mathbf{k})$ by $\alpha^2(k_z)$ where $\alpha(k_z)$ is defined as:

$$\alpha(k_z) = (k_z - k_{zo})/(b\Delta k_z) \qquad [2]$$

for $|(k_z - k_{zo})| < b\Delta k_z$ and

$\alpha(k_z) = 1$ when $|k_z - k_{zo}| >= b\Delta k_z$

where $k_z$ is the z component of that particular point in k-space, $k_{zo}$ is the point at which the function $g^{-1}(\mathbf{k})$ becomes undefined and$\Delta k_z$ is the k-space sampling interval along the z direction.

This filter starts to reduce the maximum of $g^{-1}(\mathbf{k})$ starting *b* pixels away from the singularity and rapidly brings it to zero at the singularity. The choice of *b* is discussed below. Denoting the regularized inverse filter by $g^{-1}_{reg}(\mathbf{k})$,the susceptibility map for the 3D data set is calculated via:

$$\chi(r) = FT^{-1}(g^{-1}_{reg}(\mathbf{k})\ \varphi_{zf\text{-}proc}(\mathbf{k}))/(\gamma B_o TE) \qquad [3]$$

where $\varphi_{zf\text{-}proc}(\mathbf{k})$is the Fourier transform of the high pass filtered phase $\varphi_{zf\text{-}proc}(\mathbf{r})$. The subscript “zf-proc” refers to the high pass filtered, zero filled phase images as described in references (1,2). Note that, we impose the condition $g^{-1}_{reg}(k_x=0, k_y=0, k_z=0) = 0$ in the regularized filter. This in-turn implies that the quantification is only valid for relative susceptibility differences, i.e. only $\Delta\chi$, and not for absolute $\chi$ values.

### Selection of *a* and *b*

The choice of threshold value is particularly important in determining the quality of the susceptibility map (SM). The choice of threshold *a* for g(**k**) determines to a large degree the amount of streaking that will occur. The reason for this is based more so on the discretization errors and ill-posedness of this inverse approach. To find an appropriate threshold value, phase due to a cylinder of diameter 8 voxels perpendicular to the main magnetic field, was simulated (for simulation details see the next section). A $\Delta\chi$ of 0.45 ppm, $B_0$ of 3T and TE of 5ms was assumed. Susceptibility maps were generated using $g^{-1}_{reg}(\mathbf{k})$ in Eq. [3] for varying *a* values. In the resultant SM, mean and standard deviation (SD) of susceptibility values inside the vessel were measured. The mean squared error of the values outside the vessel was also used to measure artifact levels in the background. The value of *a* was varied from 0.05 to 0.30 in steps of 0.05.

Although setting the threshold value, *a*, prevents $g^{-1}(\mathbf{k})$ from becoming ill-defined, it creates an abrupt step-like discontinuity in the behavior of $g^{-1}(\mathbf{k})$ in the neighborhood of $k_z = k_{zo}$. To avoid these abrupt transitions, we use $\alpha(k_z)$, defined with a parameter *b*, to bring the inverse filter smoothly to zero. When $| g(\mathbf{k}) | < a$, the filter smoothly reduces the value of $g^{-1}(\mathbf{k})$ starting *b* pixels away from the singularity and rapidly brings it to zero at the singularity. The value of *b* in turn depends on the value of *a* since:

$$b=|k_{za} - k_{zo}|/ (\Delta k_z) \qquad [4]$$

where $k_{za}$ is the $k_z$ coordinate value where $|g(\mathbf{k})| = a$, for a given $k_x$ and $k_y$ coordinates. One can now rewrite Eq. [2] as

$\alpha(k_z) = (k_z\text{-}k_{zo}) / | k_{za}\text{-}k_{zo} |$ [5]

### Simulations

To study the effects of partial-voluming, noise, phase aliasing and high pass filtering of phase on the susceptibility mapping process, we simulated the phase of cylinders of varying size, oriented perpendicular to the main magnetic field. The susceptibility maps of these cylinders were generated using the regularized filter $g^{-1}_{reg}(\mathbf{k})$ with an *a* value of 0.1. In these simulations, instead of calculating the phase of each of the cylinders on discrete grid points directly using the analytic formula for an infinitely long cylinder, we performed a process analogous to the MRI image acquisition. We start by simulating the cylinder and its phase on a large grid consisting of a 4096×4096 matrix. We then obtained the lower resolution version of the phase by taking the central part of its Fourier transform and applying an inverse Fourier transform to this central k-space matrix, say 512×512 for isotropic voxel size. So, for example for a cylinder that is 64 voxels wide in a 512 matrix size; this started out as a 512 voxels wide cylinder in the 4096 matrix. In that sense, if the 512×512 matrix represents 0.5×0.5 mm resolution, then we are using a resolution of 62.5μm to first sample the object discretely and by taking the central k-space, we mimic a more analytic Fourier transform representation of the final resolution's k-space signal. Data generated in this manner exhibits the usual experimental artifacts such as Gibbs ringing and partial volume effects not seen with an analytical solution. We refer to these input phase images in this chapter as the 'simulated phase' images. All simulations assumed a $B_o$ value of 3T and $\Delta\chi$ of 0.45 ppm and a cylindrical geometry perpendicular to the main magnetic field is considered.

To estimate the effect of partial voluming, cylinders with different radii (r = 0.25, 0.5, 1, 2, 4, 8, 16 and 32 voxels), perpendicular to the main magnetic field were simulated, each with voxel aspect ratios of 1:1, 1:2 and 1:4. For example, a phase image with a voxel aspect ratio of 1:2 is generated by inverse Fourier transforming only the central 512×256 points of the original 4096×4096 point k-space (and for 1:4 aspect ratio, it is the central 512×128 points). Subsequently, their corresponding susceptibility maps were generated and the mean and standard-deviation of the resultant susceptibilities were measured. Two echo times, TE=5ms and TE=20ms, were considered for this simulation to study the effect of phase aliasing on the estimated susceptibility values. While TE=5ms does not lead to any phase aliasing, the phase image at TE=20ms has considerable phase aliasing. Different voxel aspect ratios here are meant to represent the ratio between in-plane to through-plane voxel dimensions for typical transversely orientated SWI data.

The effect of high pass filtering the phase data on the susceptibility maps was also simulated and studied. Again, simulated phase images of cylindrical geometry with radii of 0.25, 0.5, 1, 2, 4, 8, 16 and 32 were considered. Homodyne high pass filters (1, 2) of size 16, 32 and 64 were applied on these phase images before being used for susceptibility mapping process. The mean and standard deviation of the susceptibility value for each simulated case were measured.

To study the effect of noise in phase images on the noise in the resultant susceptibility map, we simulated a complex data set for a cylinder of diameter 8 voxels with Gaussian noise added. Noise was added to both real and imaginary channel images such that the resultant signal-to-noise-ratio (SNR) in the magnitude image was 40:1, leading to a standard deviation in the phase image of 0.025 radians. After performing the process outlined in Eq.[3] to get the susceptibility map, this phase noise will be altered in some manner by the susceptibility mapping process. We measure the noise mean and standard deviation outside the object in the SM map.

### In vivo MR Data Collection and Processing

To reconstruct a susceptibility map of venous vessels with minimal artifacts, the following steps were carried out: i) collect an isotropic high resolution SWI data set, ii) high pass filter the phase images, iii) interpolate k-space, iv) remove spurious phase noise sources from the phase images and v) regularize the data. These steps are described in more detail below.

i) Susceptibility weighted imaging sequence, which is a high resolution 3D gradient echo sequence with velocity compensation in all 3 directions was used for data collection. The sequence parameters used were TR=26 ms, flip angle $11^o$ and bandwidth 80 Hz/pixel in the read direction. We collected images with 0.5mm isotropic resolution at 4T field strength at three echo times of 11.6ms, 15ms, and 19.2 ms and with a matrix size of 352 × 512 (phase x read directions respectively). A total of 88 slices were collected. The k-space data were then truncated in the slice select direction to mimic 1mm and 2mm thick slices and zero filled to interpolate the images to 0.5mm slice thickness in order to create maximum intensity projections (MIPs) that would match when comparing MIPs over the different resolution reconstructions. The images were acquired in absolute transverse orientation without any angulation to coronal or saggital direction.

ii) Phase data were high pass filtered using an n × n central low pass filtered image (1, 2) divided into the original complex image. This gives a homodyne or effective high pass filtered phase image, φ(x), which removes most of the low spatial frequency phase.

iii) To keep the field of view in x, y and z directions at the aspect ratio of 1:1:4, k-space was interpolated by zero filling the phase images, $\varphi_{\text{zf-proc}}(\mathbf{r})$, in all three directions to a 512 × 512 × 128 matrix size. This 3D image set, $\varphi_{\text{zf-proc}}(\mathbf{r})$, was then Fourier transformed to create a k-space data set $\varphi_{\text{zf-proc}}(\mathbf{k})$. Zero filling the initial input phase images to a larger matrix also helps in reducing the pseudo ghosting that gets introduced in the SM due to artifacts associated with the Fourier transform and application of the inverse-filter. Note that ghosting referred to here, is a form of structural-aliasing and in this sense refers to the replication of information in the image domain when the data are under-sampled. Elsewhere in this chapter we use the term aliasing to refer to phase information that has aliased back into the interval $[-\pi,\pi)$.

iv) Noise in the non-tissue region in the phase images was removed, by using a complex thresholding (12) approach on the magnitude image, followed by a skull stripping algorithm to separate the brain from the skull.

v) The regularized inverse filter discussed earlier was applied to the Fourier transform of the high pass filtered phase image.

To assess the sensitivity of SM maps to changes in venous oxygenation levels, we compare the susceptibility map data before and after ingestion of 200 mg caffeine (NoDoz, Bristol-Myers Squibb, NY, NY) for a normal healthy male volunteer. The data was acquired at 3T on a Siemens VERIO system with a voxel size of 0.5×0.5×2mm, flip angle of $15^o$ and a bandwidth of 100Hz/pixel at an echo time of 20ms. SWI images were acquired before the ingestion of caffeine and about 50 minutes after the ingestion of caffeine. All human data was collected in accordance with the local institutional review board guidelines.

## 3.3 Results

### Simulations

There are six major sources of error in creating venous susceptibility maps: i) errors in the inversion process, i.e. those due to $g^{-1}_{reg}(\mathbf{k})$ itself; ii) voxel aspect ratio effects (i.e., partial voluming); (iii) aliasing in input phase images caused by longer echo times; (iv) errors caused by high pass filtered phase data; v) errors due to discrete sampling in MRI and vi) thermal noise in the phase data. We consider each of these in the following paragraphs.

(i) Even with regularization, and with no thermal noise considered, the inversion process is not perfect. In this case, it depends on the choice of $a$. In Table 1, we show the root mean squared error (RMSE) both inside and outside the cylinder along with the percent error of the quantified susceptibility with respect to the input value of 0.45 ppm. RMSE outside the cylinder is taken only from an annular region centered around the cylinder with a thickness of 20 voxels (i.e., an annular region defined by a n inner-radius of 4 and an outer-radius of 24 voxels (beyond which the error is small)). The errors inside the object seem to be minimized with at $a$=0.15. Practically, a choice of $a$ anywhere between 0.05 to 0.2 appears to provide a reasonable estimate for the susceptibility without causing much noise or ghosting artifacts outside the object. Nonetheless, for the sake of consistency, we have used an *a* value of 0.1 for all the results presented in this manuscript. To appreciate the distribution of errors we show the phase of a cylinder perpendicular to the field and its corresponding susceptibility map in Fig.1a & b respectively. As we can see, within the susceptibility maps, the errors can be divided into three regions: a) within the object itself, b) errors along the streak artifacts corresponding to the cone of singularity in $g^{-1}_{reg}(\mathbf{k})$ in k-space, i.e points in the neighborhood of $\mathbf{k_z=k_{zo}}$ where $|g^{-1}(\mathbf{k})| > 1/a$. and c) errors outside these regions. Notice that while the cone of singularity in $g^{-1}(\mathbf{k})$ is defined in k-space at $\mathbf{k_z = k_{zo}}$ (i.e., where $\mathbf{2k_z^2 = k_x^2 + k_y^2}$), the streak artifacts in the image domain occur along $\mathbf{z^2 = 2x^2+2y^2}$.

**Table 1:**Root Mean Squared errors in susceptibility values, measured within and outside a cylinder of 8voxels diameter, for different threshold values *a*.

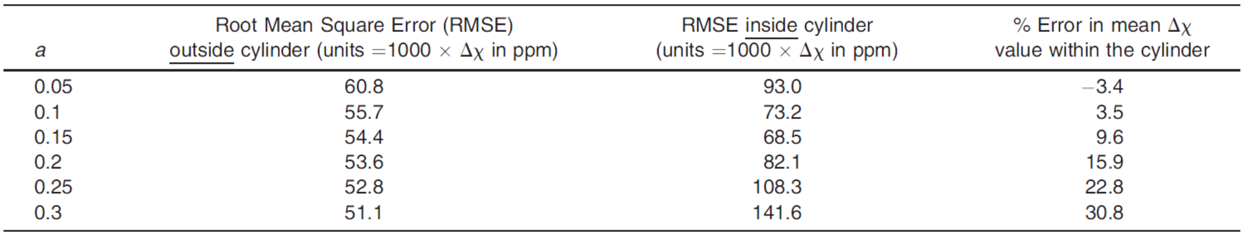

| *a* | Root Mean Square Error (RMSE) outside cylinder (units =1000 × $\Delta\chi$ in ppm) | RMSE inside cylinder (units =1000 × $\Delta\chi$ in ppm) | % Error in mean $\Delta\chi$ value within the cylinder |
|---|---|---|---|
| 0.05 | 60.8 | 93.0 | −3.4 |
| 0.1 | 55.7 | 73.2 | 3.5 |
| 0.15 | 54.4 | 68.5 | 9.6 |
| 0.2 | 53.6 | 82.1 | 15.9 |
| 0.25 | 52.8 | 108.3 | 22.8 |
| 0.3 | 51.1 | 141.6 | 30.8 |

Errors outside the cylinder were measured within a concentric annular ring with an inner radius = 4 and outer radius = 24 voxels. Also shown is the corresponding % error in quantified mean $\Delta\chi$ with respect to an expected 0.450 ppm (the error defined as (0.45 - $\chi$)).Errors outside the cylinder decrease with increasing *a* value where as for the error within the cylinder, an *a* value of 0.15 seems to be optimal. However, in general a threshold value of 0.05to 0.2 could be used depending on the contrast needed in the SM map.

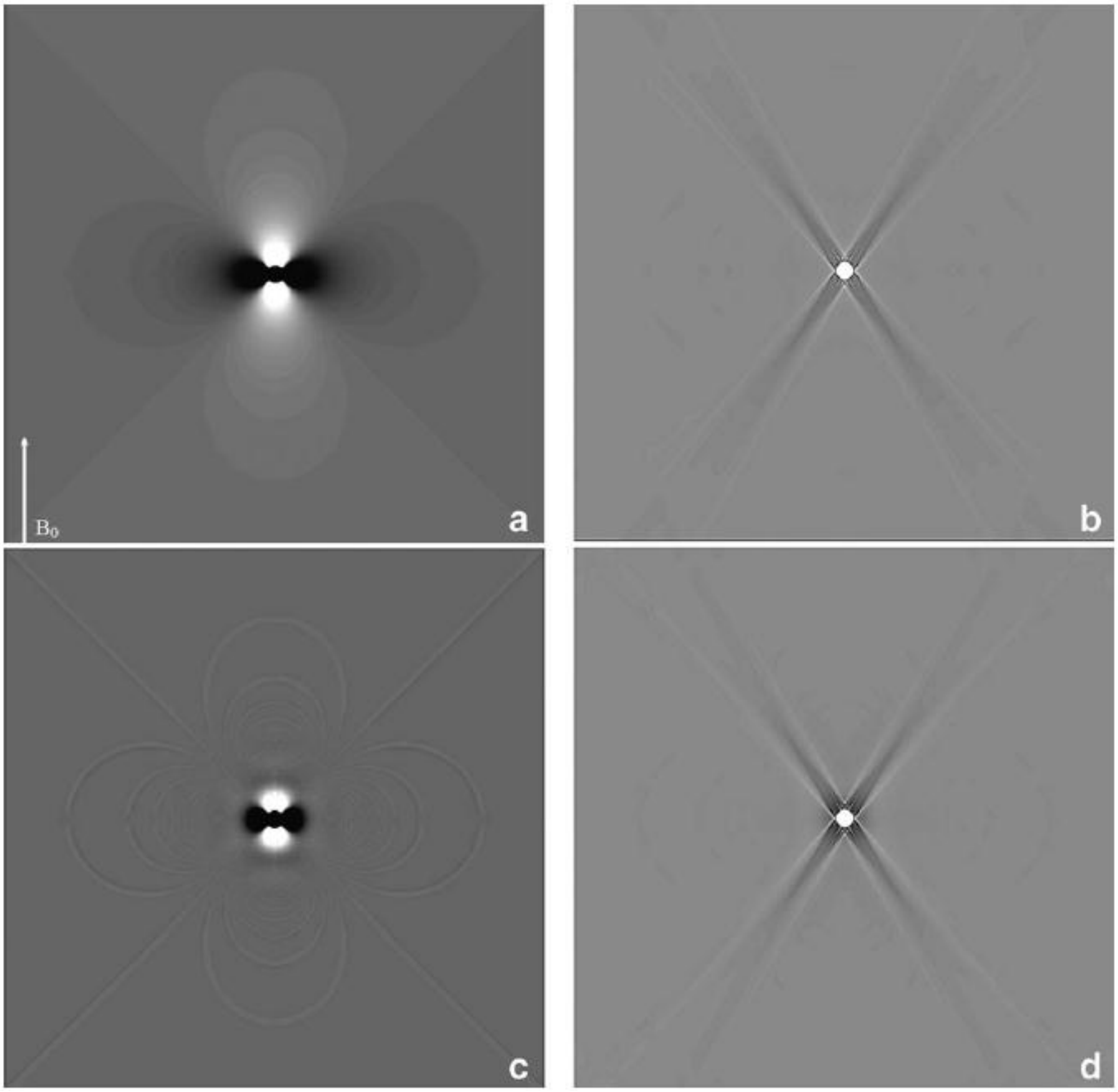

**Figure 1:** The original phase at TE = 5msec (a), high pass filtered phase (c) and their corresponding susceptibility maps (b) and (d) for a cylinder with a diameter = 8 pixels. Streak artifacts are clear in both (b) and (d). The arrow in (a) indicates the direction of Bo.

(ii) Errors outside the object, along the streak artifacts: Along the streak artifacts, (see Fig. 2a), the error in the susceptibility map measured in a region of interest the size of the vessel (near the boundary of the object) is within -5% of the input susceptibility value in voxels close to the boundary of the cylinder and drops off quickly within the next few voxels to less than -2% (see insert in Fig. 2a) and then slowly after that to less that -0.25%

at the edge of the field of view. Since the errors outside the object scale with the input susceptibility value of the vessel, the errors here are quoted as its percentage. However, if we observe plots Fig.2c and Fig.2e, it is clear that the error profile along the streak also depends on Gibbs ringings. The plots in Fig.2a and b were generated assuming no magnitude signal difference between the vessel and the surrounding background region. This provides us the minimal Gibbs ringing artifacts (arising only due to phase differences between inside and outside the vein). However, practically magnitude signal from the veins is usually different from the surrounding tissue, either lower or higher, depending on the data acquisition parameters. For example, signal from veins can be higher than the parenchyma at shorter echo times and usually at isotropic resolution where partial voluming effects are minimal; and venous signal is usually lower than the surrounding tissue at longer echo times when there is increased T2* loss (this can also happen at shorter echo times in the presence of a exogenous T2* based contrast agent) or when there is intra-voxel signal dephasing (due to partial voluming). Both these circumstances lead to additional Gibbs ringing contribution from magnitude signal differences and lead to slightly different behavior in the susceptibility maps as illustrated in Fig.2c and Fig.2e.

Errors outside the object and the streak artifacts: Outside of these two regions, the errors in the susceptibility maps (basically the systematic ‘noise’ generated outside the object due to the susceptibility mapping process) is again close to -25% in the immediate boundary of the object and drops off rapidly to less than -0.25% for most of the field-of-view (see Fig. 2b). Again, this error in the immediate neighborhood of the object is further modified by Gibbs ringing due to magnitude signal differences. However, one important point to note is that this near vessel error is negative so that when maximum intensity projections of the susceptibility maps are taken to display the veins as contiguous objects, this error is not visually apparent.

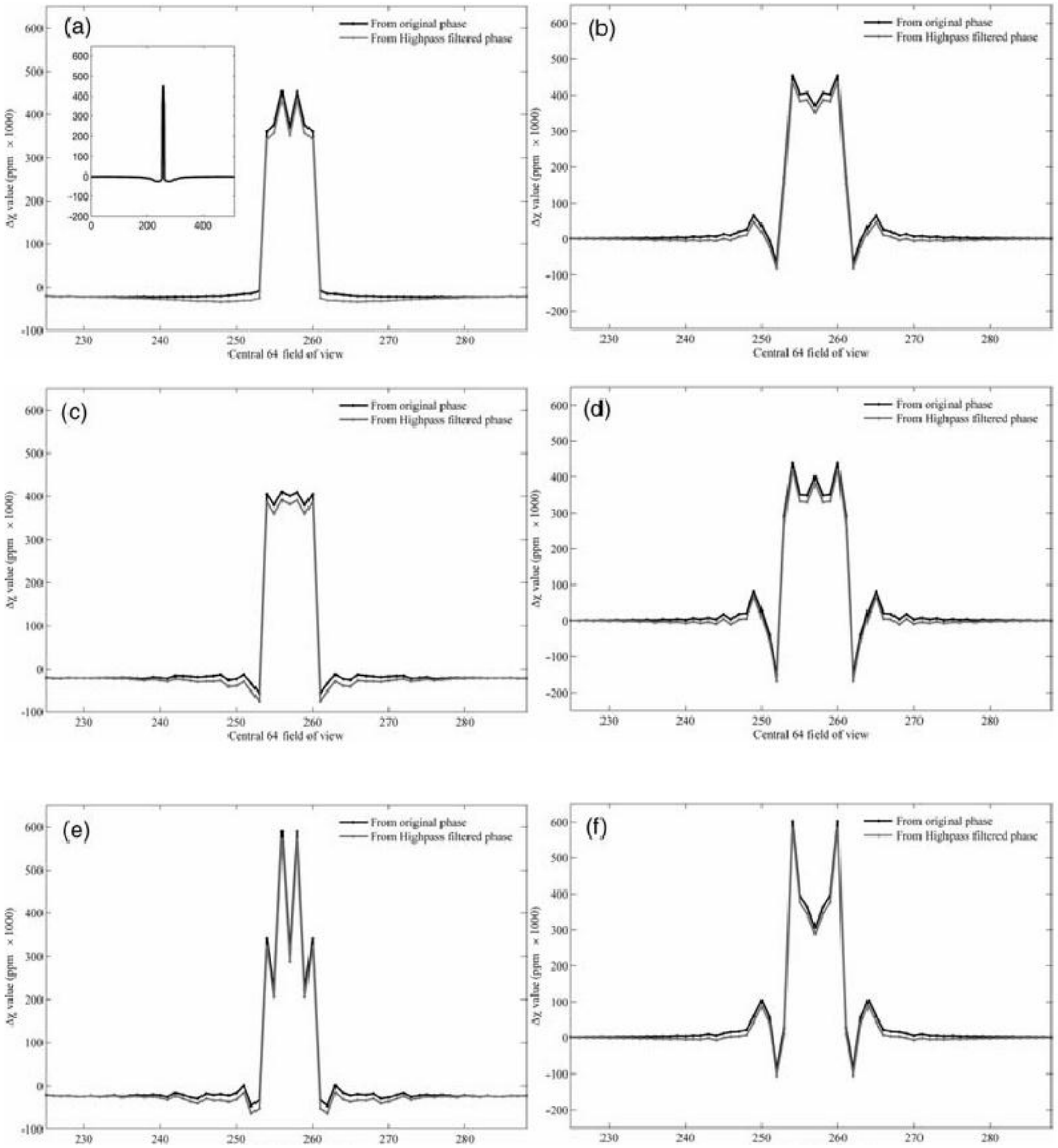

**Figure 2:** Susceptibility profile plots illustrating the quantitative nature of artifacts under different vessel-background signal conditions. Susceptibility profile plots along the streak

artifact (a, c) and along the x-axis (b, d) plotted for the central 64×64 pixels of the 512×512 image. The insert in (a) shows the profile across the full length of the streak artifact. Source phase data for all the plots here was generated from a high resolution 4096×4096 complex data set containing a magnitude and 2D phase representation of the cylinder. For plots in (a) and (b) a magnitude image for the cylinder was simulated in which the signal from cylinder and the surrounding background was taken to be the same, i.e. 1 arbitrary unit (a.u.). For plots in (c) and (d), a signal of 4 a.u. was assumed inside the cylinder and a signal of 1a.u. for the background outside. Conversely, for plots in (e) and (f) a signal of 1 a.u. inside the cylinder and 4 a.u. outside the cylinder was assumed in the magnitude. The difference in the susceptibility map profiles from (a, b) through (e, f) can be clearly seen. This difference in profiles is a direct result of Gibbs ringing that arises in the simulated data due to magnitude signal differences between the vessel and the background. In general, the errors near the boundary of the object are large but decay quickly to zero, away from the object. The gray lines show errors in the susceptibility maps from the high-pass filtered phase images (filter size 32×32). The diameter of the cylinder considered here is 8 pixels.

Errors within the cylinder: Fig.3a plots the mean and standard deviation of the measured susceptibility values across different radii cylinders and different voxel aspect ratios, for an input phase at TE = 5ms. With an isotropic resolution and a vessel diameter greater than 8 pixels, the susceptibility is underestimated by roughly 11% (with respect to the input $\Delta\chi$ value of 0.45 ppm). For objects smaller than 4 pixels, again the estimated susceptibility drops but this time more drastically as the error here depends on partial volume effects. For a diameter of two pixels, the susceptibility is already down to two thirds of its expected value and after that, it heads rapidly toward zero with the amount of signal in the susceptibility map depending on the volume of the vessel occupying the pixel. Furthermore, since through plane resolution is often less than in-plane resolution, it is interesting to look at the results for different voxel aspect ratios. It is not surprising to find that as the slice thickness to vessel diameter ratio increases, the estimates for susceptibility get worse due to increasing partial voluming. With a voxel aspect ratio of in-plane to slice thickness of 1:1 or 1:2, the susceptibility is estimated reasonably well (Fig.3a), but for an aspect ratio of 1:4, even for an object that is 4 pixels in diameter, the estimated susceptibility is beginning to significantly deviate from the actual susceptibility value.

(iii) Longer echo times can lead to signal loss and aliasing in the phase data. This leads to an effective increase in the size of the vessel and hence a reduction in the predicted susceptibility. Comparing the TE = 5ms susceptibility data in Fig.3a with the TE = 20ms data in Fig.3b, we can see that all the susceptibility values are lower in the latter case and this reduction becomes more dramatic as the vessel size decreases. This is caused by the phase aliasing that occurs at the longer echo time of 20ms which in turn affects the expected diameter of the vessel and the susceptibility. Furthermore, with aliasing, the effect of vessel partial voluming due to non-isotropic voxel dimensions follows a more drastic trend than that seen at TE 5 ms.

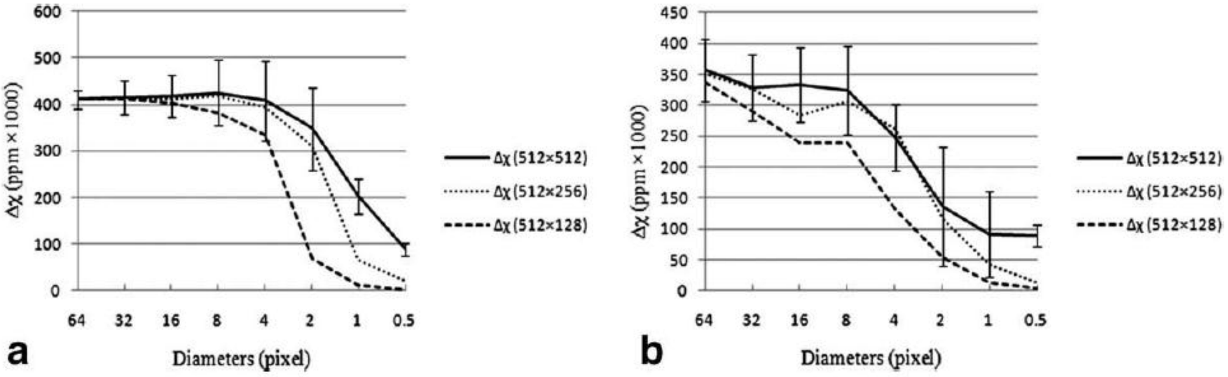

**Figure 3**: Plots of the measured susceptibility as a function of both diameter of a vessel and the aspect ratio for TE = 5ms (a) and TE = 20ms (b). The 512 × 512 simulation (created from the original 4096 × 4096 data) represents a voxel aspect ratio for an in-

plane resolution to slice thickness of 1:1. The 512 × 256 simulation represents an aspect ratio of 1:2 and the 512 × 128 simulation represents an aspect ratio of 1:4. Note that the susceptibility values are multiplied by 1000 for display purposes. Errors bars are shown for the isotropic case to demonstrate the systematic error. The errors in the 1:1 and 1:2 aspect ratios are similar and the errors in the 1:4 case are somewhat larger. Mean and standard deviation of susceptibility values were measured by zooming objects twice for cylinders with diameter 2, three times for a diameter of 1 and four times for diameter of 0.5 voxels. While no phase aliasing is present for (a), aliasing at TE 20 ms leads to an additional effect on the susceptibility quantification in (b). The input susceptibility value for all simulations was 0.45 ppm (i.e., 450 in the plot).

iv) High pass filtering: Fig. 4 shows the effect of phase high-pass filtering on the measured susceptibility values within the cylinders of different size. Effects of filter sizes, 16×16, 32×32 and 64×64 are plotted. As expected, different errors are seen for different filter sizes. Generally, the larger the filter size, the greater the quantitative error in the susceptibility value. However, in values from very small objects, about 10 voxels across or smaller, there is little variation with filter size with error being within -15% for filter sizes up to 32×32. Only at the filter size of 64×64, the error increases to -28% for an object 10 pixels wide. In fact, at a filter size of 16×16, mean susceptibility values for objects up to 20 voxels wide can be quantified with an error less than -12%. As a rule of thumb, applying a high-pass filter of a given size, $N_f$, along a particular direction leads to loss of phase information varying over a spatial extent defined by the ratio $N/N_f$ or greater, where N is the matrix size in that direction. Thus, filtering out phase from smaller structures needs larger filter sizes. It has to be noted here that the values presented here will be slightly influenced by the Gibbs ringing introduced due to magnitude signal differences between the vessel and the background. This Gibbs ringing effect will have lesser influence in a larger objects compared to smaller objects. The gray lines plotted in

Fig. 2 show the effect of high-pass filter on the "noise" (errors) outside the object and along the streak artifacts. Apart from influencing the susceptibility value inside the cylinder, high-pass filtering also causes a proportional change in the error around the boundary of the object. In general, it is seen that the susceptibility profile from unfiltered phase data, clearly illustrating the effect of loss of phase information. As noted earlier, the error at the edge of the vessel is negative so that when MIPs are taken of the veins to display them as contiguous objects, this error does not contribute to the final MIPped image of the veins.

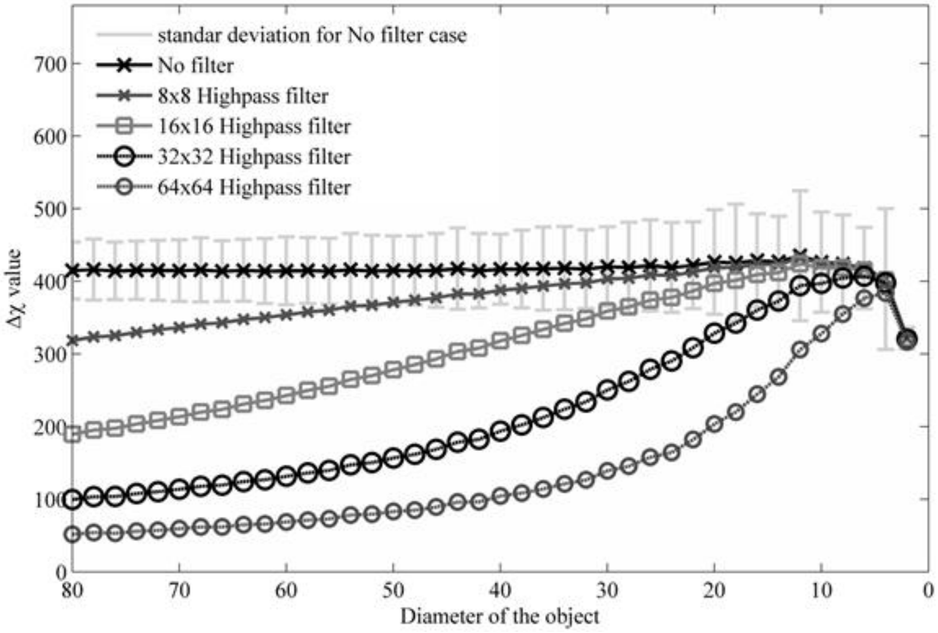

**Figure 4:** Plot shows the effect of high-pass filtering on the quantified susceptibility values. Results for four filter sizes $N_f$ (8×8, 16×16, 32×32, and 64×64) along with 'No filter' case are shown here for different object sizes. Error bars are only shown for 'No filter' case for visual clarity in the plot. Standard deviation measures (i.e error bars) for the other curves are also on the same order of magnitude and follow the same trend shown here. It is seen that quantitative error in susceptibility values increases with increasing filter size. However, for very small objects, typically smaller than 10 voxels

across, the error is less than -15% for filter size 32×32 or smaller. Applying a high-pass filter of a given size leads to a major loss of phase information in objects that are larger than ($N/N_f$) voxels, where N is the matrix size and $N_f$ is the filter size along a given direction.

v) The discretization errors can lead to improper representation of the object in the phase images because of partial volume effects. This explains in part the errors seen in Fig.3 as object size decreases. In principle, if the measured diameter of the object ($d_m$) is compared to the actual input value ($d_a$) and used to predict the area change, then we can predict the magnetic moment rather than the susceptibility. Since the magnet moment is related to the cross sectional area of the vessel times the susceptibility, the corrected value, $\Delta\chi_{actual}$, can be calculated from $\Delta\chi_{measured}\ (d_m/d_a)^2$.

vi) The systematic errors described above are distinct from the effects of thermal noise. There we see that an SNR of 2.5% in the magnitude image leads to a thermal noise or error in the phase image of 0.025 radians. If the inverse filter did not affect the phase noise at all, the noise error in the susceptibility map would be expected to be around 0.0063ppm. However, the inverse filter amplifies the noise near the streak artifacts and this leads to noise outside the magnetic source (the cylinder) of 0.035 ppm in the susceptibility map in regions outside the streak artifacts (Fig.5). This systematic error from thermal noise is independent of the object susceptibility value and hence errors are quoted in ppm rather than as percentage of the object susceptibility.

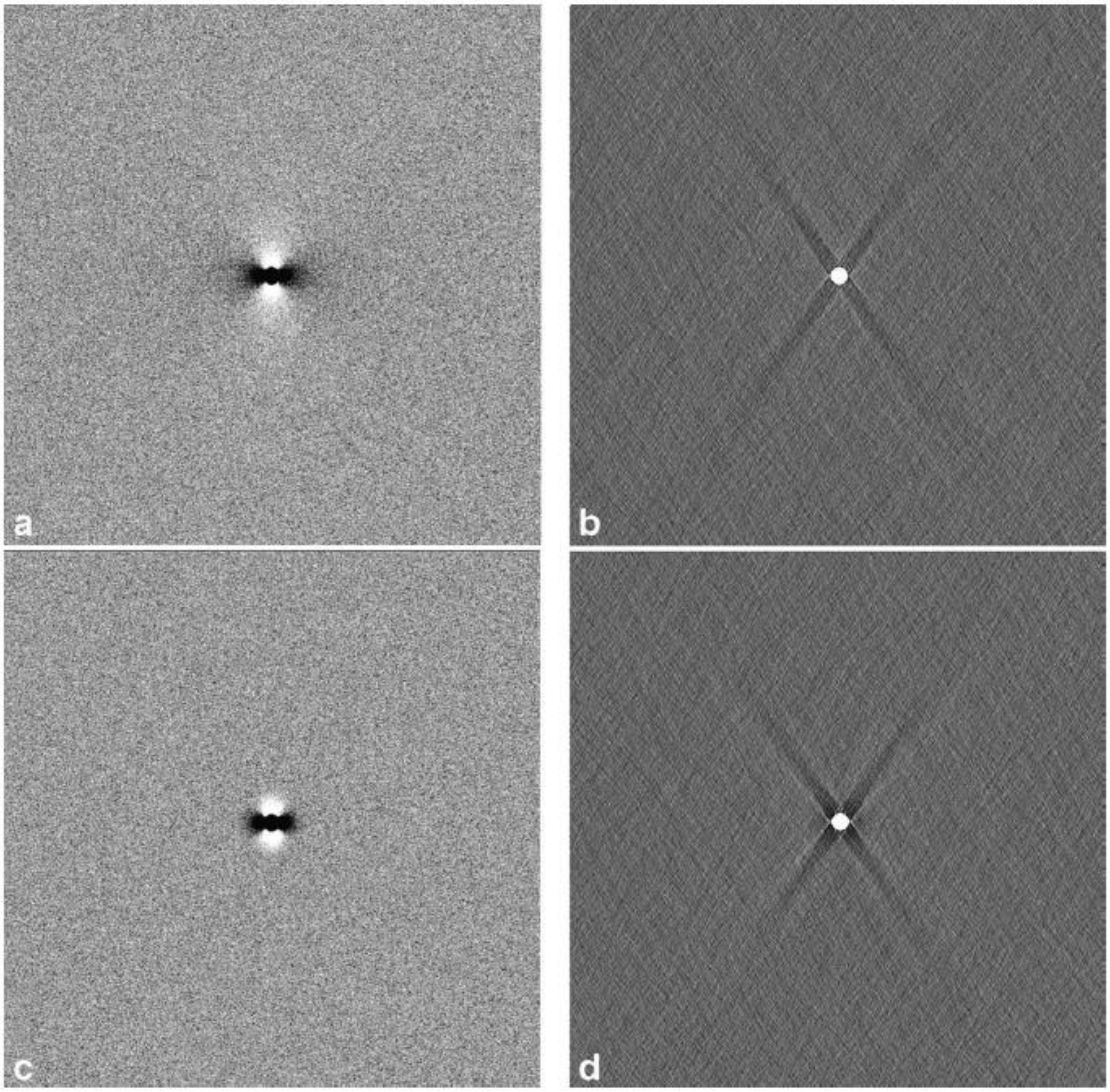

**Figure 5:** Thermal noise added to the simulated phase of a cylinder with diameter = 8 voxels, oriented perpendicular the main magnetic field (a). Following parameters were assumed: susceptibility = 0.45 ppm, Bo = 3T, and TE = 5 ms. Gaussian noise was added to the real and imaginary channels such that magnitude SNR was 40:1 resulting in thermal noise in the phase image of 0.025 radians. Corresponding susceptibility map (b). The SNR in this image is measured outside the streak artifacts. The noise in these areas increases to 0.035ppm (instead of the expected 0.0063ppm corresponding to a phase standard deviation of 0.025 radians) independent of the susceptibility of the cylinder. The susceptibility value inside the cylinder is 0.42 +/- 0.067ppm. High pass filtered phase image (64 × 64 central filter) (c) and the corresponding susceptibility map (d). The

susceptibility value inside the cylinder is now increased to 0.46 +/- 0.075 ppm. This is caused by the high pass filter effect on the phase. Note there is a negative error in susceptibility around the cylinder as seen in Figs 1 and 2.

### Susceptibility Maps of the in vivo Dataset

In the following material, we review the results of the implementation of the susceptibility mapping process as applied to an *in vivo* data set. First, we show how a vessel changes its phase behavior as it courses through the brain making different angles to the main magnetic field (Fig.6a). Using the conventional SWI processing here would enhance the veins parallel to the field but would incorrectly enhance the outside of the veins perpendicular to the field. After the susceptibility mapping process (Fig.6b), the vein appears as one contiguous object. A second example of this is given in the simpler in-plane case where larger veins show a clear dipole effect (Fig.7a). Again the susceptibility map shows a bright vessel along the entire path (Fig.7b), and the negative Gibbs ringing effect can also be seen.

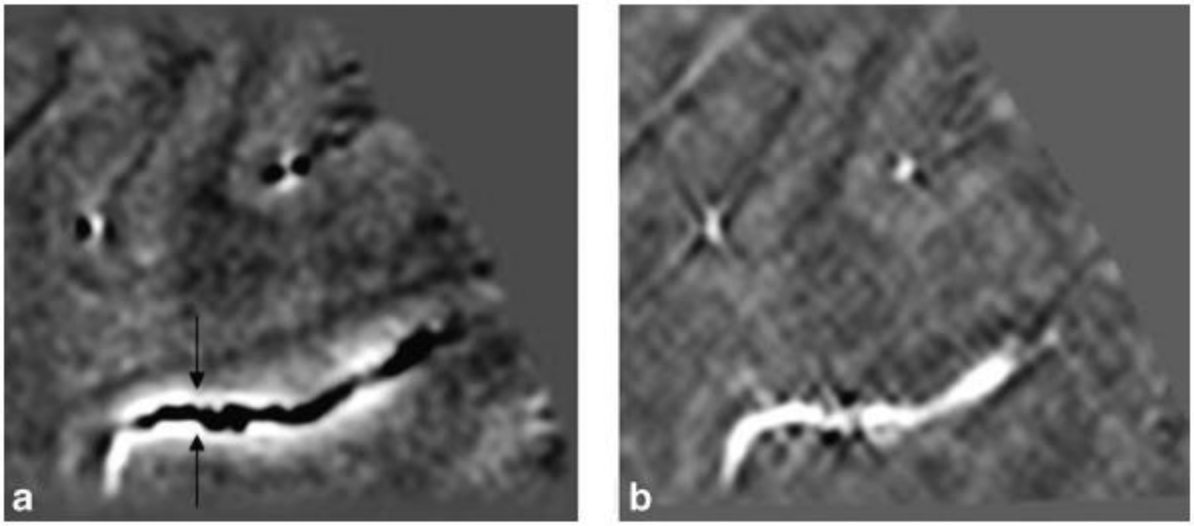

**Figure 6:** A sagittal cut demonstrating the change in phase at TE = 19.2ms, as a vein courses through the brain (a). For proper visualization of the whole vessel section, phase from 2 saggital slices (i.e., total thickness 1mm) was combined. In the phase image, the dipole effect is clearly seen with the vessel appearing dark in the phase image when perpendicular to the field and bright when parallel to the field. The distance from the top of the vessel (upper arrow) to the bottom of the vessel (lower arrow) is 7 slices (3.5mm). The fact that the phase is clearly seen in one slice with the correct sign suggests that the vein is on the order of one or two pixels in diameter (i.e., 0.5mm to 1mm). The same vein shown from the corresponding susceptibility map (b). Clearly, most of the dipolar phase around the vessel is removed and susceptibility of the vessel is highlighted throughout, independent of its orientation with the main magnetic field.

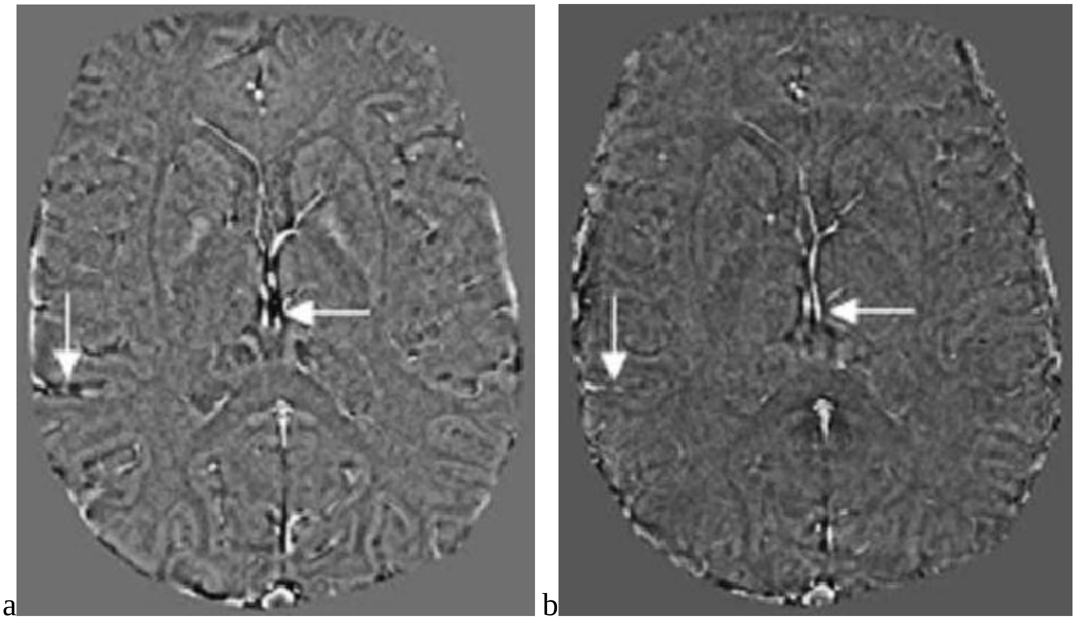

**Figure 7:** High pass filtered phase image showing the dipole effects for the TE = 19.2ms case (a). Corresponding susceptibility map (b). Note there is a small negative band at the edge of the major vessels as also seen in the simulations, but overall the vessels are clearly highlighted without a varying dipole effect obscuring vascular information.

Since we are interested in displaying the susceptibility map of the veins, we present next an example set of susceptibility maps to compare with the original phase data. In Fig.8a, we show an MIP of the phase (from a right handed system) with 0.5mm isotropic resolution with an echo time of 19.2ms. The vessels are clearly shown with reduced intensity. The dipolar effect with the opposite polarity in phase can be seen on the outside of the vessels. In Figs.8b-8d, we show the corresponding susceptibility maps for TEs of 11.6ms, 15ms and 19.2ms respectively. From the venous vessel perspective, these images from different echo times are almost identical to each other.

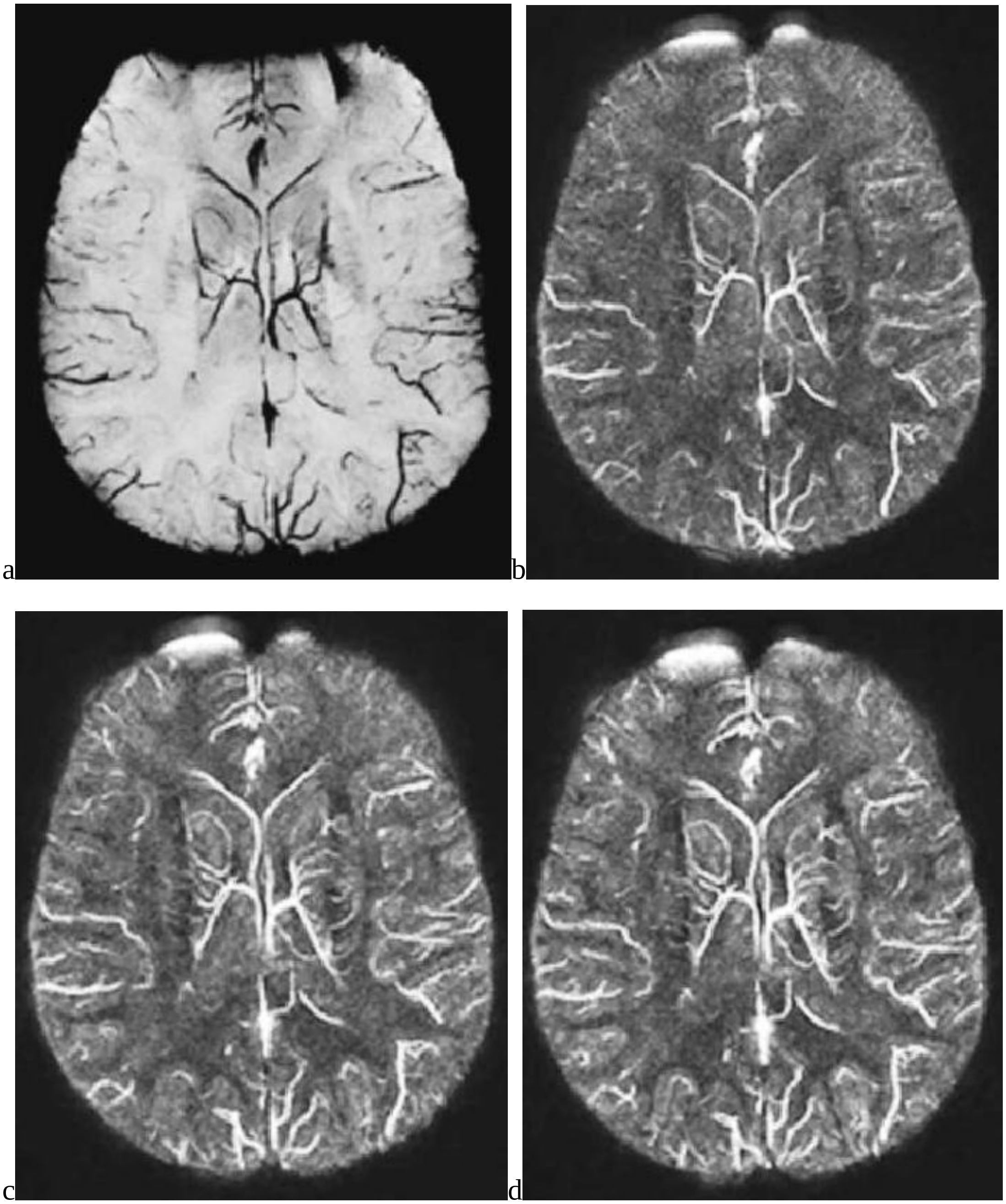

**Figure 8:**mIP (minimum Intensity Projection) over 16mm (32 slices) of the phase images collected at TE = 15ms (a) along with the corresponding susceptibility maps from TE = 11ms (b), TE = 15ms (c) and TE = 19.2ms (d) phase data. Phase data were filtered with a 64 × 64 central filter. The image in a represents minimum intensity projection (mIP) over 16mm for a right handed system and all the corresponding susceptibility maps are MIPped over the same 16mm.

There are a few key observations to be made here. First, the image with the shortest echo time is the most noisy as it has much less phase information i.e., less phase-SNR. The phase-SNR here refers to $\frac{\gamma \cdot \Delta B \cdot TE}{\sigma_{phase}}$ where, $\gamma$ is the gyromagnetic ratio, $\Delta B$ is the field perturbation and $\sigma_{phase}$ is the phase standard deviation for a given imaging experiment which relates to magnitude SNR as $\sigma_{phase}=1/SNR_{magnitude}$. Second, the contrast between gray matter and white matter improves at longer echo times. Third, the smaller vessels become more visible and better defined at longer echo times because there is more phase information available outside the vessel. Quantitatively speaking, all of the above points are related to the initial SNR in the phase image (unlike magnitude SNR, phase SNR actually increases initially with increasing TE, so long as T2* loss is not significant and there is no phase aliasing). The higher this phase SNR, the better the corresponding susceptibility map image. Fourth, the heavy air/tissue interface artifacts present in normal SWI data are also present in the susceptibility map data. This can be seen from the very bright area in the right frontal part of the brain which could have been manually removed, but it is left in the figure to demonstrate this potential problem. Fifth, the original phase MIP shown in Fig.8a sometimes shows small vessels better than the susceptibility map data and sometimes the susceptibility map data shows better images of the vessels.

To validate that the results for the vessels were almost independent of TE, we measured the susceptibility in three large veins (Table 2). The largest vein had a susceptibility close to the normal expected value for the venous blood’s susceptibility of 0.45ppm. For display purposes, the susceptibilities are scaled by 1000, so the numbers quoted in the figures and tables should be on the order of 450. A susceptibility of 0.45ppm corresponds to an oxygen saturation of 70% when assuming a hematocrit of 0.45 and a susceptibility difference between fully oxygenated and deoxygenated blood, $\chi_{do}$, of 2.26ppm is 0.45ppm in SI units (13). The mean oxygen saturation value of 70% measured from a large vein (Vein of Galen) agrees with many literatures. The susceptibility value of the thalmostriate vein is around 0.3ppm which may be caused by the partial volume effects. For smaller vessels, partial volume effects will lead to the underestimated susceptibility values. According to Eq. 7 in Chapter 2, oxygen saturation is inversely proportional to the susceptibility; therefore, underestimated susceptibility value leads to an overestimate of the venous oxygen saturation.

The mean values for the different echo times lay within ten percent of the means despite the large variance. The large variance for each individual measurement was caused, in part, by a broad distribution of values since the region of interest was drawn to cover the entire vessel. When only the central part of the vessel was used, the standard deviations were much smaller.

**Table 2:** Susceptibility values of left and right thalmostriate vein and the vein of Galen

| TE\Vein | V1 | V2 | V3 |
|---|---|---|---|
| 11.6 ms | 278/78 | 289/62 | 435/70 |
| 15 ms | 331/98 | 303/85 | 461/163 |
| 19.2 ms | 323/90 | 280/64 | 434/119 |

Mean and standard deviation for the susceptibility values of three veins (in ppm × 1000) chosen from the 0.5 × 0.5 × 0.5 isotropic voxel data shown in Fig.8. V1 is for the left thalmostriate vein, V2 for the right and V3 for the vein of Galen. There is not much variation of susceptibility value with echo time, as would be theoretically expected.

Practically these isotropic scans take a long time to collect and have limited coverage. If parallel imaging is used it would be possible to reduce the scan times by a factor of 2 to 4. Therefore, the next step is to see if reasonable susceptibility maps can be derived from slices that are 1mm thick (Fig.9a) or 2mm thick (Fig.9b) as are acquired today in most SWI applications. Fig.9 shows that the thicker slices have better SNR but poorer contrast for displaying the veins. Although a few vessels have begun to become less defined with 1mm thick slices, there is a much greater loss of small vessel information in the 2mm slices. However, the thicker the slice, the better the gray-matter/white-matter contrast. For the vein of Galen, the susceptibility values remain essentially unchanged close the expected value of 0.45 ppm. As shown in Fig.3, as the slice thickness increases (i.e., the aspect ratio changes from 1:1, to 1:2 to 1:4) relative to the cylindrical objects, a reduction in the effective susceptibility is expected. For the thicker slices, the peak susceptibility drops to 0.41ppm for 1mm thick slices, and to 0.30 ppm for the 2mm thick slices showing that the partial volume effect is degrading the contrast in the images.

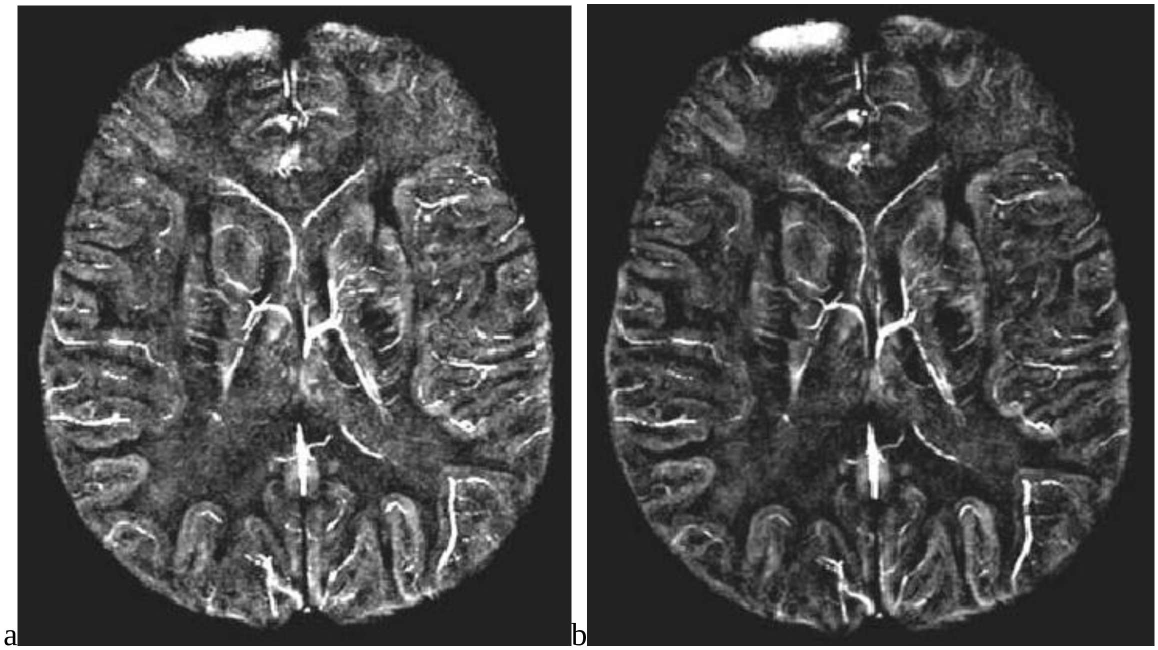

**Figure 9:** Thicker initial slices of 1mm (a) or 2mm (b), projected (MIP) over the same thickness as in Fig. 8, show the pros and cons of susceptibility mapping for lower resolution images. The thicker slice images were created from the original 0.5mm isotropic data so there is no misregistration between the images in Fig.8 and here. Note that the thicker the slice the better the SNR (especially for the gray matter and white matter) but the less clearly small vessels are seen. This is because the phase information in the voxel is now corrupted by integration of the complex signal across the slice.

As another example, we compare the susceptibility maps before and after ingestion of 200 mg caffeine (NoDoz, Bristol-Myers Squibb, New York, NY) to examine the changes in oxygenation levels in the veins and to see if any obvious changes are visible in other parts of the brain such as the basal ganglia. It has been suggested that iron content in the basal ganglia are revealed by SWI data or susceptibility map may have some contribution from the BOLD (blood oxygen level-dependent) effect and if that is the case there should be some change in oxygen saturation after ingestion of caffeine. Caffeine will affect both blood flow and neural activity. Caffeine is a member of the methylxanthine family of drugs that are adenosine antagonists. Vasoconstriction due to caffeine is thought to primarily reflect the antagonism of adenosine $A_2$ receptors. As binding of adenosine to A2 receptors is associated with vasodilation, caffeine-related antagonism may reduce the ability of adenosine to contribute to functional increases in cerebral blood flow (CBF). Since brain activity remains constant or even increases, the decrease of CBF in the presence of caffeine should thus increase the oxygen extraction fraction (OEF) in order to maintain CMRO2 (20). The increased OEF leads to the increase of the concentration of deoxyhemoglobin in the blood; therefore, we expect to see higher susceptibility values in post caffeine administration case. Fig. 10 shows the projection of the data over 4 slices (8 mm), for both before and after ingestion of 200 mg of caffeine. There is a clear increase in the susceptibility of venous blood, as can be seen from the brighter venous vessels in Fig. 10d, indicating an increase in deoxyhemoglobin levels post caffeine administration. The susceptibility values in the thalamostriate vein increased from 0.121 ± 0.007 to 0.166 ± 0.008 ppm while that in the smaller veins increased from 0.095 ± 0.006 to 0.122 ± 0.007 ppm (Fig. 11). Fig. 10c and 10d indicate the vessels from which measurements were made. For the thalamostriate vein, the susceptibility value increases 37% which corresponds to venous oxygen saturation decreased 16% (according to Eq. [7] in Chapter 2). No change in basal ganglia iron content was measured.

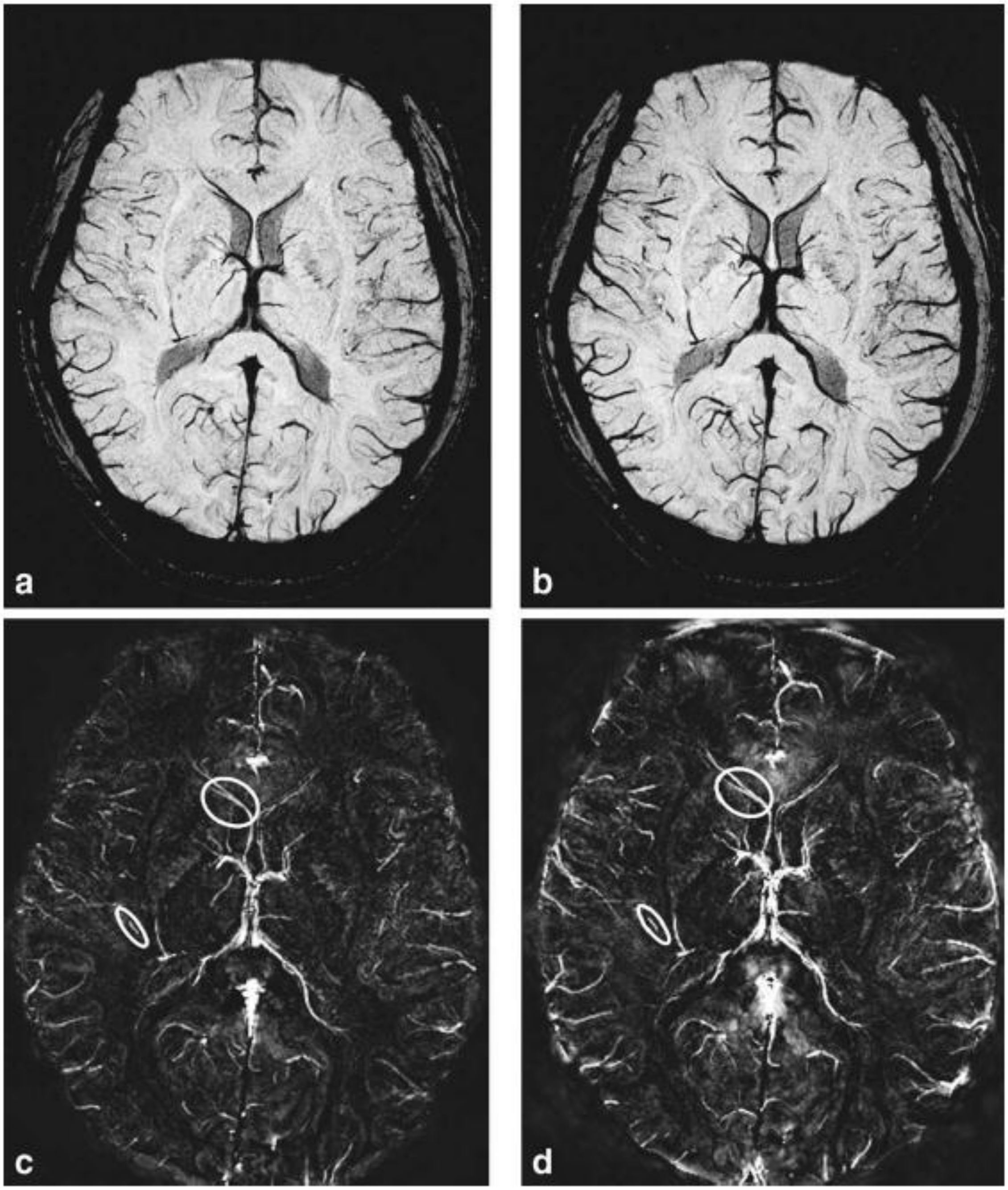

**Figure 10:** Minimum intensity projections (mIP) of SWI images pre (a) and post (b) caffeine administration (8mm thick sections). Corresponding susceptibility maps pre(c) and post (d) caffeine. A thalamostraiate vein and a small vein are shown within the circles. It is in these regions where the oxygen saturation measurements were made. Note that images (c) and (d) are set to the same intensity-window levels to have a fair comparison.

We can clearly see the overall enhancement of the venous structures in the post-caffeine image (d). Similarly, window levels for images (a) and (b) are also set at the same values for appropriate visual comparison.

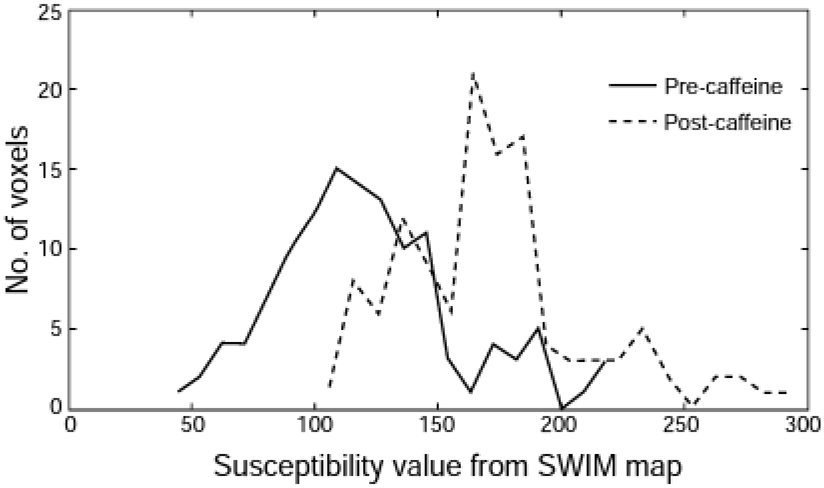

**Figure 11:** Histogram of the susceptibility in the thalamostriate vein showing a clear shift to the right post caffeine administration. The susceptibility values are 1000 times the actual value (so a value of 200 represents 0.2 ppm in SI units). The susceptibility value increases 37% which is corresponding to venous oxygen saturation decreased 16%.

## 3.4 Discussion

### Effects of Inverse Filter Regularization

The basic concept of using a simple Fourier transformation method to predict the magnetic field distribution from a given susceptibility distribution was described first by Deville at al (11). Since then a number of papers have used this simple k-space filter to predict the magnetic field perturbation in MR (4-7). However, the inverse problem, i.e., obtaining the source susceptibility distribution from magnetic field measurements, is more complicated. Provided that the shape/geometry of the susceptibility source is known, this problem can also be tackled as a forward problem approach by fitting the predicted field to the measured field (6, 7). Another way to solve this problem is by taking the direct inverse of the k-space kernel function. However, this inverse filter has a singularity at all points that satisfy the equation $1/3 = k_z^2/\mathbf{k}^2$, and only regularization methods (8) or multiple acquisition methods (9) have heretofore been used to remove most of these artifacts.

In our approach, we have regularized the signal based on the proximity of the sampled point in k-space to the cone of singularity. The closer a k-space point is to the point of singularity, the more rapidly it is set to zero. This creates a smooth approach to zero from either side of the singularity where the function jumps rapidly from very small numbers to very large numbers. This appears to work fairly well in simulations giving systematic errors that depend on the object size. The signal-to-noise ratio in the final susceptibility maps appears to be reasonably well behaved with an error of 7.8% for 0.45 ppm (i.e., 0.035ppm) at 3T and TE = 5ms (assuming an initial 40:1 SNR in the magnitude images). As susceptibility increases, the effective SNR for the susceptibility map data will also increase. The SNR as a function of echo time is a bit more complicated. If there were no T2* effects and no phase aliasing, then the SNR would be expected to vary linearly with phase, i.e. increase with phase. However, since the signal decays according to exp(-TE/T2*), it is well known that this gives an optimal echo time of TE = T2*. Practically, images acquired at longer echo times (such as TE 25 ms at 3T, which is roughly the T2* value for normal venous blood) suffer from serious problems associated with signal loss and aliasing at the edge of the vein and also at air/tissue interfaces.

Susceptibility maps from a human brain data set with different threshold values are shown in Fig.12. The 'noise' outside the brain in the SMs is significantly decreased with increasing threshold value, *a*. Table 3 presents mean and standard deviation of susceptibility values for three different sized veins with different threshold values. Quantitatively, the smaller the threshold value, the more accurate the susceptibility values. However, smaller threshold values also have more serious 'noise'/artifacts (see Table 1). Therefore, when we choose a threshold value, we must compromise between the susceptibility values and artifacts/noise to get an acceptable susceptibility map. The threshold values between 0.05 to 0.2 seem to provide good choices depending on the application. If a more accurate estimate of oxygen saturation is needed, the lower value of 0.1 or 0.15 might be best, while, based on our experience, if it is overall CNR and the ability to evaluate the gray matter and white matter contrast in the susceptibility map, then 0.2 might be best, as suggested by Fig.12.

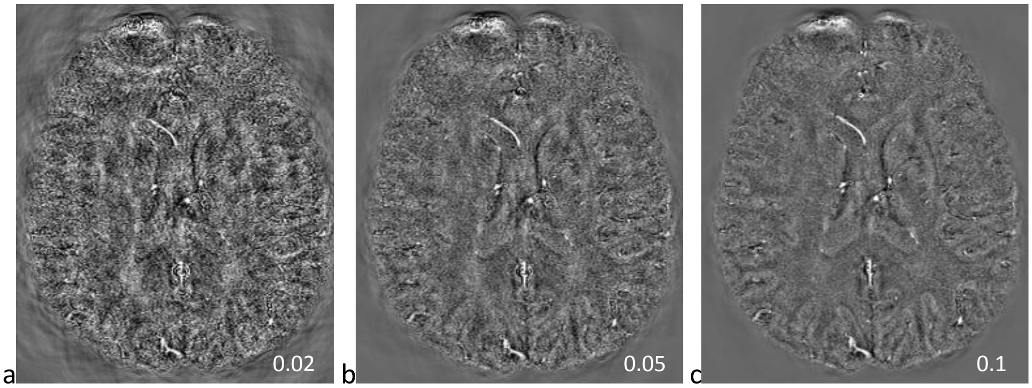

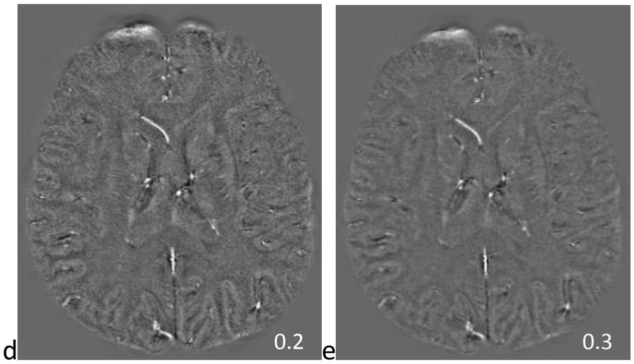

**Figure 12:** Susceptibility maps from the 0.5 × 0.5 × 0.5 isotropic voxel human brain data with threshold value (a) 0.02, (b) 0.05, (c) 0.1, (d) 0.2 and (e) 0.3. The 'ghosting' artifact is seen to reduce with increasing *a*.

**Table 3:** Susceptibility values for different threshold values

| Vein\Threshold | *a* = 0.02 | *a* = 0.05 | *a* = 0.1 | *a* = 0.2 | *a* = 0.3 |
|---|---|---|---|---|---|
| V1 | 321 / 95 | 299 / 82 | 271 / 63 | 225 / 53 | 174 / 48 |
| V2 | 324 / 94 | 315 / 87 | 289 / 75 | 227 / 61 | 177 / 41 |
| V3 | 457 / 98 | 446 / 92 | 418 / 77 | 358 / 52 | 282 / 43 |

Mean and standard deviation of susceptibility values (in ppm × 1000) measured from the same three veins as in Table2, obtained for different threshold values *a* = 0.02, 0.05, 0.1, 0.2 and 0.3. Phase data from TE=11.6ms was used for susceptibility mapping. Increasing *a* values lead to more and more under estimation of the susceptibilities, in agreement with results in Table 1.

### Effects of Echo Time on the Susceptibility Maps

A major feature of the susceptibility map is its theoretical independence of susceptibility to the choice of echo time. This is indicated in Fig. 8 and Table 2. If the magnitude SNR and the phase information in the short echo time images were good enough, one would not need to use the long echo times that we do today for SWI for example. If a susceptibility map could be obtained from an echo time of 11ms and a repeat time of 15ms, it would be a much more efficient sequence and one which could also be used as an

MRA sequence as well. Nevertheless, as also shown in Fig.8, there is indeed a susceptibility map-SNR (SM-SNR) dependence with echo time. We expect the SM-SNR to increase for TE approaching T2*. However, the effect of echo time is complicated since longer echo times will lead to aliasing around the vein. This aliasing coupled with partial volume effects creates a non-physical phase at the edge of the object. (By non-physical, we mean that there is no geometry or susceptibility distribution that can act as a physical source for this type of phase and therefore the inverse process will produce artifacts.) The expected dipolar phase without aliasing occurs outside this area and because of this the susceptibility map will have two parts to it. The first part is the correct reconstruction of a widened object based on the fact that the vessels exhibit the expected dipole behavior. The second part will be the systematic artifacts associated with aliasing and non-physical phase effects. These will lead to systematic noise and ghosting (or structural aliasing) associated with non-physical phases in the susceptibility maps. However, if the area in question has complete signal dephasing, setting the phase in this region to zero will give a magnetic moment close to the correct value in the widened object without much concern as to this non-perfect choice of central phase. In fact, that is why these images tend to reconstruct quite well despite all the potential problems. However, in closing this discussion, it should be realized that this is also the reason why we do not at this point try and use the quantified results of susceptibility maps to extract oxygen saturation. Finally, ghosting (or structural aliasing) remains even with no noise, creating a negative ring around the vessel. Larger objects suffer more from this error, and it is for this reason that objects larger than 16 pixels tend to have a nearly 10% systematic drop than the expected susceptibility.

### Methods to Improve Quality of Susceptibility Map

Regularization is not the only means necessary to reconstruct good quality susceptibility maps. There are also key signal processing and image reconstruction concepts that need to be applied to the data to remove other types of artifacts. The first is a more finely sampled k-space. This avoids serious ghosting in the reconstructed susceptibility map. The second is spatial resolution high enough to allow for as many pixels as possible to give useful phase information outside the source. The third is echo time long enough for phase development so as to achieve sufficient phase SNR. The use of all these methods has led to the high quality images presented in this chapter. In principle, one could actually collect higher resolution data in the read direction at the possible expense of signal-to-noise without an increase in acquisition time, while it would increase data acquisition time in either the phase or partition encoding direction. However, zero filling in the image domain to interpolate in k-space seems to suffice to remove much of the Gibbs ringing effects.

Moreover, reducing the presence of noise in the phase images is crucial in obtaining a high quality susceptibility map. Not only should the noisy pixels from the magnitude image be thresholded, but also areas of wildly varying phase coming from, for example, the skull where out-of-phase fat can cause a serious problem. Setting the phase inside spherical or cylindrical regions to be a constant also helps avoid phase noise effects.

Areas of constant phase jumps will also generate a new type of structural ghosting artifact that we refer to as the inverse dipole rippling effect. That is, if the phase appears as a constant without the expected concomitant external phase behavior, then this rippling effect emanating from the source will permeate the image in a non-local fashion. A similar effect can be caused by remnant phases that survive the high pass filter. This leaves a non-physical phase at the edge of the brain. This could be tackled either by simply eliminating that tissue (and hence not obtaining useful susceptibility images in that part of the brain) or by using the forward model from the magnitude geometry constraints in an attempt to remove air/tissue interface phase effects (14). The better that this job is done, the less errors will permeate other parts of the brain from the rippling/ghosting effects described above.

Partial volume effects can cause a complete loss of phase information when the vein is much smaller than the slice thickness (13). For example, an aspect ratio of 1:4 appears to give the best cancellation effects and turns the phase inside small vessels from positive to negative for a right handed system. This leads to the issue of the reduced measured susceptibilities. There are a few causes for the reduced values: partial volume effects, phase aliasing and loss of signal due to spin dephasing around the magnetic source. In each of these cases, it is necessary to use the estimated size of the source larger than its actual value. For veins (cylinders), this means a reduction in the susceptibility by the ratio of the original area to the enlarged area, and for spheres a reduction in the susceptibility by the ratio of the original volume to the enlarged volume. Again, forcing the phase inside the object to be zero has little impact on the actual estimate for the magnetic moment (which is directly related to the product of the area times susceptibility for the veins or the volume times the susceptibility for a spherical microbleed for example). On the other hand, the partial volume effect can lead to smoothing effects. Although we do see the negative ring around the vessels in the *in vivo* data, the expected large dip in the center of the vessels is to a large degree absent.

The choice of how many slices to process to create a venous susceptibility map depends not so much on regional and global structural variations (as it does if one is estimating the effects of air/tissue interfaces (14)), but rather on how many slices the vessel phase appears in. This means that one can reconstruct the susceptibility map image with an arbitrary number of the acquired slices if one is interested only in local vessels and if this process removes more noise, it can lead to further improvement in the susceptibility maps.

Susceptibility mapping offers a means to study BOLD effects in an entirely different light. Although phase has been used in BOLD fMRI experiments, susceptibility values can be used to quantify changes in oxygenation levels and then infer changes in flow as well (15). In Fig. 10, there is a clear increase in signal after ingestion of caffeine indicating an increase in deoxyhemoglobin levels. Measurements in other smaller veins together show an overall 30 to 40% increase in the susceptibility value after caffeine administration. This increase corresponds to a reduction in blood flow of close to 30% which is larger than what is usually observed for caffeine. This particular person was a non-coffee drinker and so the large amount of caffeine may have had an abnormally large effect. In this particular subject, no change in basal ganglia iron content was measured pre and post caffeine. Some small shifts in GM iron content could be found. These measurements may eventually help separate out the fractional contributions to phase from ferritin and deoxyhemoglobin.

In conclusion, we have shown that despite the problems in obtaining consistent susceptibility values for all vessels, it is possible to remove phase variations caused by major vessels in SWI high pass filtered phase images. This should be useful in creating SWI processed data without the associated non-local, long distance dipole effects. In the future, it may be possible to use this approach to evaluate quantitatively microbleeds and calcifications (16) and to map oxygen saturation from veins throughout the brain (rather than with the single vessel approach proposed initially in (17) and used more extensively in recent years (18, 19)). Finally, the images shown here present a new form of MR venography and can serve as a quantitative means to distinguish potential oxygen saturation abnormalities in SWI data. Future applications of susceptibility mapping may include iron measurements in tissue.

## REFERENCES

1. Reichenbach JR, Venkatesan R, Schillinger DJ, Kido DK, Haacke EM. Small vessels in the human brain: MR venography with deoxyhemoglobin as an intrinsic contrast agent. Radiology 1997;204:272–277.
2. Haacke EM, Xu Y, Cheng Y-CN, Reichenbach JR. Susceptibility weighted imaging (SWI). Magn Reson Med 2004;52:612–618.
3. Ali Fatemi A, Boylan C, Noseworthy MD, Identification of breast calcification using magnetic resonance imaging. Med. Phys 2009; 36 (12): 5429-5436.
4. Salomir R, Senneville BD, Moonen CT. A Fast Calculation Method for Magnetic Field In homogeneity due to an Arbitrary Distribution of Bulk Susceptibility. Concepts Magn Reson Part B (Magn Reson Engineering) 2003; 198:26-34.
5. Marques JP, Bowtell R. Application of Fourier-Based Method for Rapid Calculation of Field Inhomogeneity Due to Spatial Variation of Magnetic Susceptibility. Concepts in Magnetic Resonance, Part B (Magn Reson Engineering) 2005;25:65-78.
6. Koch KM, Papademetris X, Rothman DL, de Graaf RA. Rapid calculations of susceptibility-induced magnetostatic field perturbations for in vivo magnetic resonance. Phys Med Biol 2006;51(24):6381-6402.
7. Cheng YCN, Neelavalli J, Haacke EM. Limitations of calculating field distributions and magnetic susceptibilities in MRI using a Fourier based method, Physics in Medicine and Biology, 2009; 54: 1169-1189.
8. Kressler B, de Rochefort L, Liu T, Spincemaille P, Jiang Q, Wang Y. NonlinearRegularization for Per Voxel Estimation of Magnetic Susceptibility Distributions From MRI Field Maps. IEEE Trans Med Imaging. 2009.
9. Liu T, Spincemaille P, de Rochefort L, Kressler B, Wang Y. Calculation ofsusceptibility through multiple orientation sampling (COSMOS): a method forconditioning the inverse problem from measured magnetic field map tosusceptibility source image in MRI. Magn Reson Med. 2009 Jan;61(1):196-204.
10. YaoB, T.-Q.Li, GelderenP.v., ShmueliK., de Zwart J.A., Duyn J.H., Susceptibility contrast in high field MRI of human brain as a function of tissue iron content. Neuroimage, 2009. 44(4): 1259-1266.
11. Deville G, Bernier M, Delrieux J. NMR multiple echoes observed in solid 3He. Physical Review B, 1979; 19:5666–5688.
12. Pandian DS, Ciulla C, Haacke EM, Jiang J, Ayaz M. Complex threshold method for identifying pixels that contain predominantly noise in magnetic resonance images. J Magn Reson Imaging. 2008; 28: 727-735.

13. Xu Y, Haacke EM.The Role of Voxel Aspect Ratio in Determining Apparent Phase Behavior in Susceptibility Weighted Imaging. MRI 2006;24:155-160.
14. Neelavalli J, Cheng YCN, Jiang J, Haacke EM. Removing Background Phase Variations in Susceptibility Weighted Imaging Using a Fast, Forward-Field Calculation. J Magn Reson Imaging 2009;29:937–948
15. Haacke EM, Lai S, Reichenbach JR, Kuppusamy K, Hoogenraad FGC, Takeichi H, Lin W. In Vivo Measurement of Blood Oxygen Saturation Using Magnetic Resonance Imaging: A Direct Validation of the Blood Oxygen Level-Dependent Concept in Functional Brain Imaging. Human Brain Mapping 1997; 5:341–346
16. Wu Z, Mittal S, Kish K, Yu Y, Hu J, Haacke EM. Identification of calcification with MRI using susceptibility-weighted imaging: A case study. J Magn Reson Imaging 2008; 29 (1): 177 - 182
17. Haacke EM, Kuppusamy K, Thompson M, et al. High Resolution EPI fMRI using a head gradient coil insert. In: Proceeding of the fourth international conference on functional mapping of the human brain, Montreal, Canada 1998 (Abstract 0547)
18. Barnes S, Haacke EM. Susceptibility weighted imaging: clinical angiographic applications. MRI Clinical N Am 2009 - 17;47-61.
19. Langham MC, Magland JF, Epstein CL, Floyd TF, Wehrli FW. Accuracy and precision of MR blood oximetry based on the long paramagnetic cylinder approximation of large vessels. Magn Reson Med 2009; 62: 333–340.
20. Haacke et al, Susceptibility Weighted Imaging in MRI: Basic Concepts and Clinical Applications. 1st Ed. Wiley-Blackwell, 2011

# Chapter 4: Improving Susceptibility Mapping Using a Threshold-Based K-space/Image Domain Iterative Fourier Transform Reconstruction Approach[3]

---

[3] Most of the contents of this chapter have been adapted from Tang J, Liu S, Neelavalli J, Buch S, Cheng YC. J. Haacke EM. Improving Susceptibility Mapping Using a Threshold-Based K-space/Image Domain Iterative Fourier Transform Reconstruction Approach, Magn Reson Med 2012; In Press.

## 4.1 Introduction

Susceptibility weighted imaging (SWI) using phase information has become an important clinical tool [1-3]. However, the use of phase information itself has stimulated great interest both as a source of contrast [4-6] and a source for producing susceptibility maps (SM) [7-24]. The impetus for solving the inverse problem from magnetic field perturbation came from the work described in Deville et al. [25]. This was noted by Marques and Bowtell in 2005 [26]. Salomir et al. [27] were the first group to utilize this concept in MRI. Unfortunately, this inverse process is ill-posed and requires a regularization procedure to estimate the susceptibility map. There are a variety of approaches to tackle this problem [7-24]. One unique method uses a multiple orientation data acquisition to remove the singularities [17]. Constrained regularizations [14,20,22,23] have shown good overall results, but they require longer reconstruction times and assumptions about the contrast in or near the object to be detected. Threshold-based, single-orientation regularization methods (TBSO) [11,15,18,24] provide the least acquisition time and the shortest computational time to calculate SM. However, their calculated SMs lead to underestimated susceptibility values ($\Delta\chi$) and display severe streaking artifacts especially around the brain areas with large $\Delta\chi$, such as veins.

Based on TBSO approaches, we propose an iterative method to overcome the singularities in the inverse filter and produce improved accuracy for susceptibility mapping. In this approach, we iteratively replace k-space values associated with the SM, $\chi(k)$, near the singularities to obtain an almost artifact free SM, $\chi(r)$. Values used for substitutions are estimated using structural information from the masked version of $\chi(r)$.

Simulations using two dimensional cylinders and full 3D models of the brain were performed to examine the efficacy of this iterative approach. High resolution human data are also evaluated.

## 4.2 Materials and Methods

Briefly, the expression for the susceptibility distribution [26,27] derived from the phase data can be written as (for a right handed system[28]):

$$\chi(r) = FT^{-1}\left[\frac{1}{g(k)} \bullet FT\left[\frac{\Phi(r)}{-\gamma B_0 TE}\right]\right] [1]$$

where,

$$g(k) = \frac{1}{3} - \frac{k_z^2}{k_x^2 + k_y^2 + k_z^2} [2]$$

and $\Phi(r)$ is the phase distribution, TE is the echo time, $\gamma$ is the gyromagnetic ratio for hydrogen protons, $B_0$ is the main field strength, $k_x$, $k_y$ and $k_z$ are coordinates in k-space, and g(k) is the Green's function or filter. Clearly, the analytic inverse filter $g^{-1}(k) = 1/g(k)$, is ill-posed when g(k) is equal or close to zero, i.e., points on or near two conical surfaces in k-space at the magic angles of 54.7° and 125.3° from the $B_o$ axis. This ill-posedness leads to severe artifacts (including severe streaking) in $\chi(k)$ and noise amplification [29]. Thus, for a proper pixel-by-pixel reconstruction of $\chi(r)$, recovering the correct values of $\chi(k)$ near the region of singularities is critical.

### K-space Iterative Approach

If the shapes of the structures of interest are known, then one can use this information in the SM to create a more accurate k-space of said SM in the conical region. The structure of the vessels is obtained directly from the first pass susceptibility map $\chi_{i=0}(r)$. The detailed steps of the iterative method are discussed below and shown in Fig. 1.

**Step-1:** An initial estimate of the SM, $\chi_{i=0}(r)$, is obtained by applying a regularized version of the threshold-based inverse filter, $g_{reg}^{-1}(k)$ [18], in Eq.[1] using the suggested threshold value, *thr*=0.1. The subscript "i" denotes the SM after the $i^{th}$ iteration ("i=0" denotes the initial step before doing the iterative method and i=1 for the first iteration).

**Step-2:** The geometry of the structures of interest is extracted from $\chi_{i=0}(r)$ using a binary vessel mask, i.e. outside the veins, the signal in the mask is set to zero, and inside it is set to unity. Since streaking artifacts associated with veins in the SM are usually outside the vessels, after multiplying the $\chi_i(r)$ map by the mask, little streaking remains in the SM. This leads to $\chi_{vm,\ i}(r)$ as shown in part (b) of Fig.1. Vessel mask generation will be addressed in the next section.

**Step-3:** $\chi_{vm,\ i}(k)$ is obtained by Fourier transformation of $\chi_{vm,\ i}(r)$ (part (c) in Fig. 1).

**Step-4:** The pre-defined ill-posed region of k-space in $\chi_{vm,\ i}(k)$ is extracted (part (d) in Fig. 1). These extracted k-space data are denoted by $\chi_{vm,\ cone,\ i}(k)$. The size of $\chi_{vm,\ cone,\ i}(k)$ is decided by a threshold value, *a*, which is assigned to g(k). For the matrix size 512×512×512, the percentages of cone region in k-space for a given *a*, are 2.4% (*a*=0.01), 24.1% (*a*=0.1), 47.1% (*a*=0.2) and 70.6% (*a*=0.3), respectively. As can be seen, when *a* increases, the size of $\chi_{vm,\ cone,\ i}(k)$ increases too.

**Step-5:** Data from $\chi_{\text{vm, cone, i}}(\text{k})$ and $\chi_{i=0}(\text{k})$ (part (e) in Fig. 1) are merged. This means part of $\chi_{i=0}(\text{k})$ has been replaced by $\chi_{\text{vm, cone, i}}(\text{k})$. The merged data are denoted by $\chi'_{\text{merged, i}}(\text{k})$ (part (f) in Fig. 1).

**Step-6:** Inverse Fourier transformation of $\chi'_{\text{merged, i}}(\text{k})$ gives the improved SM, $\chi_{i+1}(\text{r})$ (part (g) in Fig. 1).

**Step-7:** $\chi_i(\text{r})$ in step-1 is replaced by $\chi_{i+1}(\text{r})$ from step-6 and the algorithm is repeated until

$$\sqrt{\Sigma\left[(\chi_i(r)-\chi_{i+1}(r))^2\right]/N}<\varepsilon \qquad [3]$$

where N is the number of pixels in $\chi_i(\text{r})$ and $\varepsilon$ is the tolerance value chosen here to be 0.004ppm.

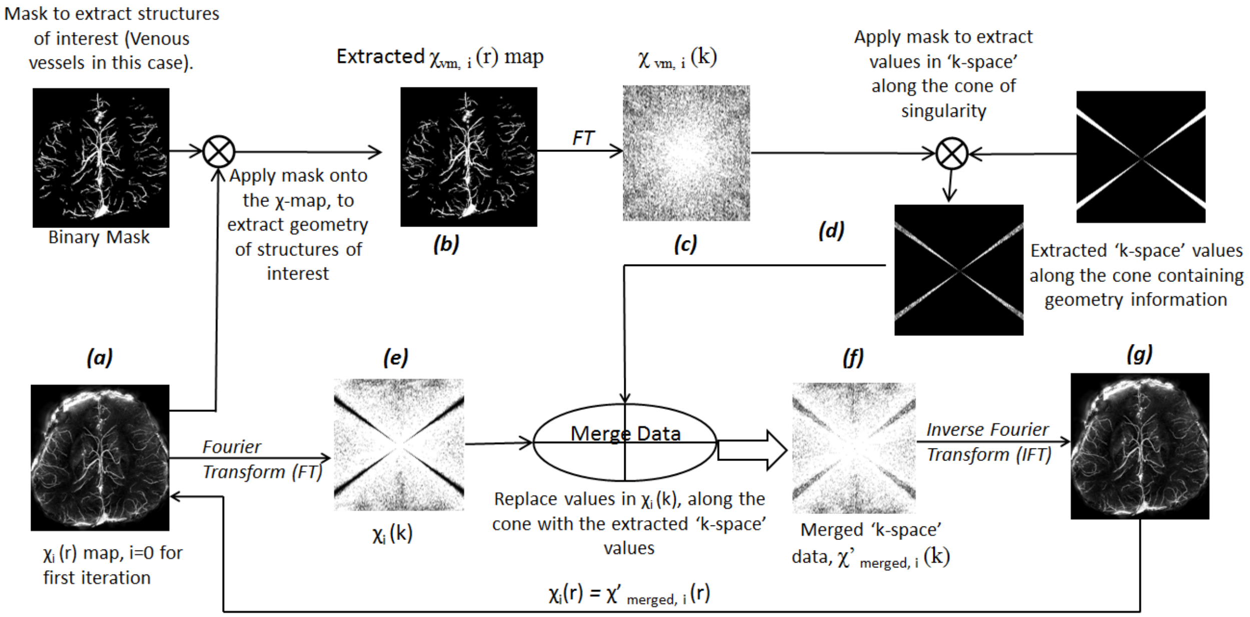

**Figure 1:** Illustration of the iterative reconstruction algorithm to obtain artifact free $\chi(\text{r})$ maps.

### Binary Vessel Mask Generation

The binary vessel mask was generated using thresholding from the $\chi(r)$ map itself. The detailed steps are discussed below and shown in Fig. 2.

**Step-1:** A threshold, $th_1$, is applied to $\chi_{i=0}(r)$ to create an initial binary vessel mask, $M_0$. The pixels whose susceptibility values are lower than $th_1$ will be set to zero while those greater than or equal to $th_1$will be set to unity. In this study, a relatively low susceptibility of 0.07 ppm is used for $th_1$ to capture most vessels. However, doing this inevitably includes many other brain structures in $M_0$.

**Step-2:** Morphological operation i.e. closing operation is performed to fill in holes in $M_0$ to generate an updated mask $M_1$.

**Step-3:** A median filter is applied to remove noise in $M_1$ and create $M_2$.

**Step-4:** False positive data points from $M_2$ are removed as following: First, the $\chi(r)$ map is Mipped over 5 slices centered about the slice of interest to better obtain contiguous vessel information, as seen in $\chi_{MIP}(r)$. Second, another threshold, $th_2$ = 0.25ppm, is performed on $\chi_{MIP}(r)$ to create a new$\chi_{MIP_vm}(r)$ and binary mask $M_P$, which only contains vessels. 0.25 ppm was chosen to isolate the major vessels in the MIP image. Third, each slice from $M_2$ is compared with $M_P$ on a pixel by pixel basis to create $M_3$. If a data point from $M_2$ does not appear on$M_P$, this data point will be treated as a false positive and removed from $M_2$. This process can be equally well applied to extract other tissues by choosing appropriate threshold values, $th_1$and $th_2$.

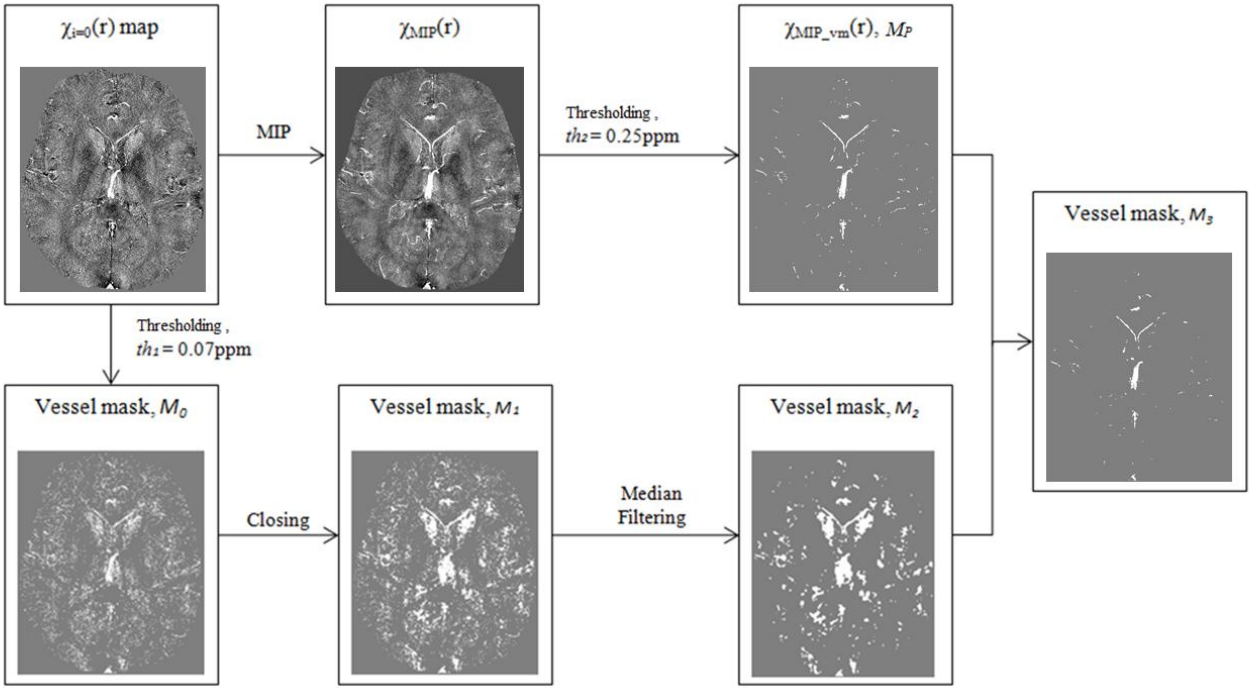

**Figure 2:** Illustration of the binary vessel mask generation process.

## 2D Cylinder Simulations

Simulation of a two dimensional cylinder and its induced phase was started on a 8192 × 8192 matrix. A lower resolution complex image was obtained by taking the Fourier transform of this matrix and applying an inverse Fourier transform of the central 512 × 512 matrix in k-space. This procedure is to simulate Gibbs ringing effects caused by the finite sampling which we usually see in the actual images. Gibbs ringing also comes from discontinuities in the magnitude image. To avoid this form of Gibbs ringing, we used a magnitude image with a uniform signal of unity. Cylinders with diameters 32, 64, 128, 256, 512, and 1024 were simulated on 8192 x 8192 matrices and their effective diameters were 2, 4, 8, 16, 32, and 64 on 512 × 512 matrices. All phase simulations were using a forward method [8,26,27,32] assumed $B_o$= 3T, $\Delta\chi$ =0.45 ppm in SI units, TE = 5 ms, and the cylinder perpendicular to the main magnetic field. 0.45ppm is the susceptibility value for venous blood when the hematocrit (Hct) = 0.44, $\Delta\chi_{do} = 4\pi \cdot 0.27$ppm [30] and the oxygen saturation level = 70%, where $\Delta\chi_{do}$ is the susceptibility difference between fully deoxygenated and fully oxygenated blood [31]. A relatively small echo time was chosen to avoid phase aliasing that can affect the estimated susceptibility values.

### *Selection of a TBSO Method to Generate the $\chi_{i=0}(r)$ Map*

Threshold based single-orientation (TBSO) methods [11, 15, 18, 24] use a truncated g(k) to solve the singularity problem in the inverse filter $g^{-1}(k)$ when g(k) is less than a predetermined threshold value, *thr*. When g(k) <*thr*, $g^{-1}(k)$ is either set to zero [11, 24]; or to 1/*thr* [15]; or to set $g^{-1}(k) = 1/thr$ first and then bringing $g^{-1}(k)$ smoothly to zero as k approaches $k_{zo}$. This smoothing is accomplished by multiplying $g^{-1}(k)$ by $\alpha^2(k_z)$ with$\alpha(k_z) = (k_z-k_{zo}) / | k_{zthr}-k_{zo} |$ where $k_z$ is the z component of that particular point in k-space, $k_{zo}$ is the point at which the function $g^{-1}(k)$ becomes undefined, and $k_{zthr}$ is the $k_z$ coordinate value where $|g(k)| = thr$ [18].

SMs using methods [11,15,18] were calculated based on Eq. 1 using the 2D cylindrical model. Equation 1 can be used to calculate the SM for the simulated 2D cylinder model perpendicular to the main field since the 2D perpendicular model is a special case of the 3D model with 1 slice [10]. Streaking artifacts are obvious in all three SMs (figures are not shown). The calculated mean susceptibility values inside the cylinder are around 0.40±0.01ppm for all SMs. The background noise levels, (i.e., standard deviation of the susceptibility values measured from a region outside the streaking artifact in SM using ref [18] are around 1/2 to 2/3 of the other two using ref [11,15] using *thr* = 0.06, 0.07 and 0.1, which are the optimal threshold values suggested in [11, 12, 18]. Given this, the method in [18] was chosen to generate a $\chi_{i=0}(r)$ map.

*Finding an Optimal Threshold Value*

To find the optimal threshold, a series of $\chi(r)$ maps were reconstructed by the iterative method using threshold value $a$ = 0.01, 0.03, 0.07, 0.1, 0.15, 0.2, 0.25 and 0.3. The larger this threshold, the closer $\chi(r)$ will be to $\chi_{vm}(r)$. The optimal threshold value was found by comparing the accuracy of the estimated susceptibility values as well as the effects on reducing streaking artifacts in the reconstructed $\chi(r)$ maps. To study the effect of noise in $\chi(r)$ maps due to the noise in phase images, complex datasets for cylinders of diameter 2, 4, 8, 32 voxels, respectively, were simulated with Gaussian noise added to both real and imaginary channels. Noise was added in the complex images to simulate an $SNR_{magnitude}$ of 40:1, 20:1, 10:1 and 5:1 in the magnitude images. Since $\sigma_{phase} = 1/SNR_{magnitude}$, this corresponds to $\sigma_{phase}$ = 0.025, 0.05, 0.1 and 0.2 radians.

To estimate the improvement in the SM by the iterative method, we used a root mean squared error (RMSE) to measure streaking artifacts outside the cylinder. Background noise in the SM is measured in a region away from all major sources of streaking artifacts to compare to the noise measured in the phase image (i.e., so we can correlate noise in the phase with the expected noise enhancement from the inversion process).

*Effect of High-Pass Filter*

The effect of high-pass (HP) filtering the phase data on the $\chi(r)$ map generated by the iterative method was also studied. Phase images of a cylindrical geometry with diameters of 2, 4, 8, 16, 32, and 64 voxels were simulated. Homodyne HP filters [33] with a 2D hanning filter (full width at half-maximum, FWHM = 4, 8, 16, and 32 pixels) were applied on these phase images in both in-plane directions. SM reconstructions were stopped based on the criteria in step 7 of the iterative process.

### Three Dimensional Brain Model Simulations

To address the potential of the iterative technique to improve SM of general structures such as the basal ganglia, a 3D model of the brain was created including the: red nucleus (RN), substantia nigra (SN), crus cerebri (CC), thalamus (TH), caudate nucleus (CN), putamen (PUT), globus pallidus (GP), grey matter (GM), white matter (WM), cerebro-spinal fluid (CSF) and the major vessels. Susceptibility values in parts per million (ppm) for each structure were taken from the literature review [12] and from measuring the mean susceptibility value in a particular region from SMs using ref. [18] from real human data: RN = 0.13, SN = 0.16, CC = -0.03, TH = 0.01, CN = 0.06, PUT = 0.09, GP = 0.18, vessels = 0.45, GM = 0.02, CSF = -0.014 and WM=0. All structures were set inside a 512×512×256 matrix of zeros. The phase of 3D brain model was created directly applying the forward method [8,26,27,32] to the 3D brain model with different susceptibility distributions using imaging parameters: TE = 5ms and $B_0$ = 3T. A comparison between the phase maps from this brain model and a real data set with the imaging parameters: $B_0$=3T and TE=18ms is shown in Fig. 3.

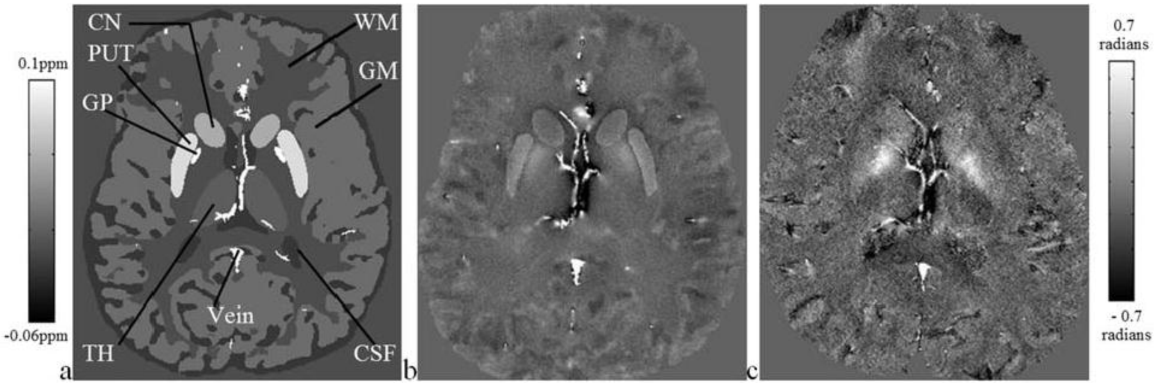

**Figure 3:** a) A transverse view of the 3D brain model. b) The simulated phase map from the model using parameters: $B_o$=3T and TE=18ms which are consistent with imaging parameters in the real data c). Images b) and c) have the same window level setting.

## In Vivo MR Data Collection and Processing

A standard high-resolution 3D gradient echo SWI sequence was used for data acquisition. A transverse 0.5 mm isotropic resolution brain dataset was collected at 3T from a 23-year-old healthy volunteer. The sequence parameters were: TR = 26 ms, flip angle = $15^o$, read bandwidth = 121 Hz/pixel, TE = 14.3 ms, 192 slices, and a matrix size of 512 × 368. To reconstruct $\chi_{i=0}(r)$ with minimal artifacts, the following steps were carried out:

1) The unwanted background phase variations were removed using either: a) a homodyne HP filter (FWHM = 16 pixels) [33] or b) Prelude in FSL [34] to unwrap the phase, followed by the process of Sophisticated Harmonic Artifact Reduction for Phase data (SHARP) [35] with a filter radius of 6 pixels. To reduce artifacts in the calculated SMs, regions with the highest phase deviations due to air/tissue interfaces were removed manually from the HP filtered phase images and the phase in those regions were set to be zero.

2) A complex threshold approach [36] was used to separate the brain from the skull.

3) The phase image with an original matrix size of 512 × 368 × 192 was zero filled to 512 × 512 × 256 to increase the field-of-view and to avoid streaking artifacts caused by the edge of brain to alias back to the reconstructed SM.

4) The regularized inverse filter, $g_{reg}^{-1}(k)$ [18] was applied to obtain $\chi_{i=0}(r)$, followed by the iterative process using $a = 0.1$. For *in vivo* data, the iterative program was terminated at the third iterative step.

## 4.3 Results

***Selection of threshold level based on simulations*:** To find the optimal threshold value, SMs were reconstructed using $a$= 0.01, 0.03, 0.07, 0.1, 0.15, 0.2, 0.25 and 0.3, respectively, with different noise levels (Fig. 4). The streaking artifacts shown in $\chi_{i=0}(r)$(the first column in Fig. 4a) have been significantly reduced by the iterative method and fall below the noise level when $a$>= 0.1. Also, when $a$>= 0.1, the mean susceptibility value inside the cylinder was found to increase to 0.44ppm when the diameter of the cylinder was larger than 8 pixels (Fig. 4b) and this trend is independent of the object size and the noise in the phase image. The optimal result in terms of obtaining the true susceptibility value was with a threshold of 0.1. Fig. 4c shows a plot of RMSE of the susceptibility values from the whole region outside the 32-pixel cylinder using different $a$. The RMSE of the susceptibility values decreases as $a$ increases. Therefore, for vessels, a value of 0.3 would be the optimal value. However, a large threshold value means replacing more original k-space with the k-space only consisting of vessel information which will saturate the signals from other brain structures and blur these structures. Since the SM using $a = 0.1$ already reveals the optimal susceptibility value for the vessels and an acceptable RMSE, it is appropriate to choose 0.1 for more general applications to study the entire brain.

Fig. 4a compares the converged $\chi_{i=b}(r)$ map with the $\chi_{i=0}(r)$ map, where $b$ is the iterative step required to reach convergence. In this data, $b = 2$ when $a = 0.01$ and 0.03, $b = 3$ when $a = 0.07$, 0.1 and 0.15 and $b = 4$ when $a = 0.2$, 0.25 and 0.3 when $\sigma_{phase} = 0$. When $\sigma_{phase}$ becomes bigger, more iterative steps were required to reach convergence. For instance, the maximum iterative step is 9 when $\sigma_{phase} = 0.2$ radians. Using a noise level of 0.025 radians in the phase image as an example, $g_{reg}^{-1}(k)$ [18] leads to a susceptibility noise of roughly 0.025 ppm in the $\chi_{i=0}(r)$ map. The iterative approach leads to a slight decrease in background noise, 0.021 ppm, in $\chi_{i=3}(r)$ map when $a= 0.1$. The background noise was measured in a region outside the streaking artifact indicated by the black circle in Fig. 4a. The overall decrease in RMSE in the background (Fig. 4c) is a consequence of both a decrease in streaking artifacts and a reduction in thermal noise contribution.

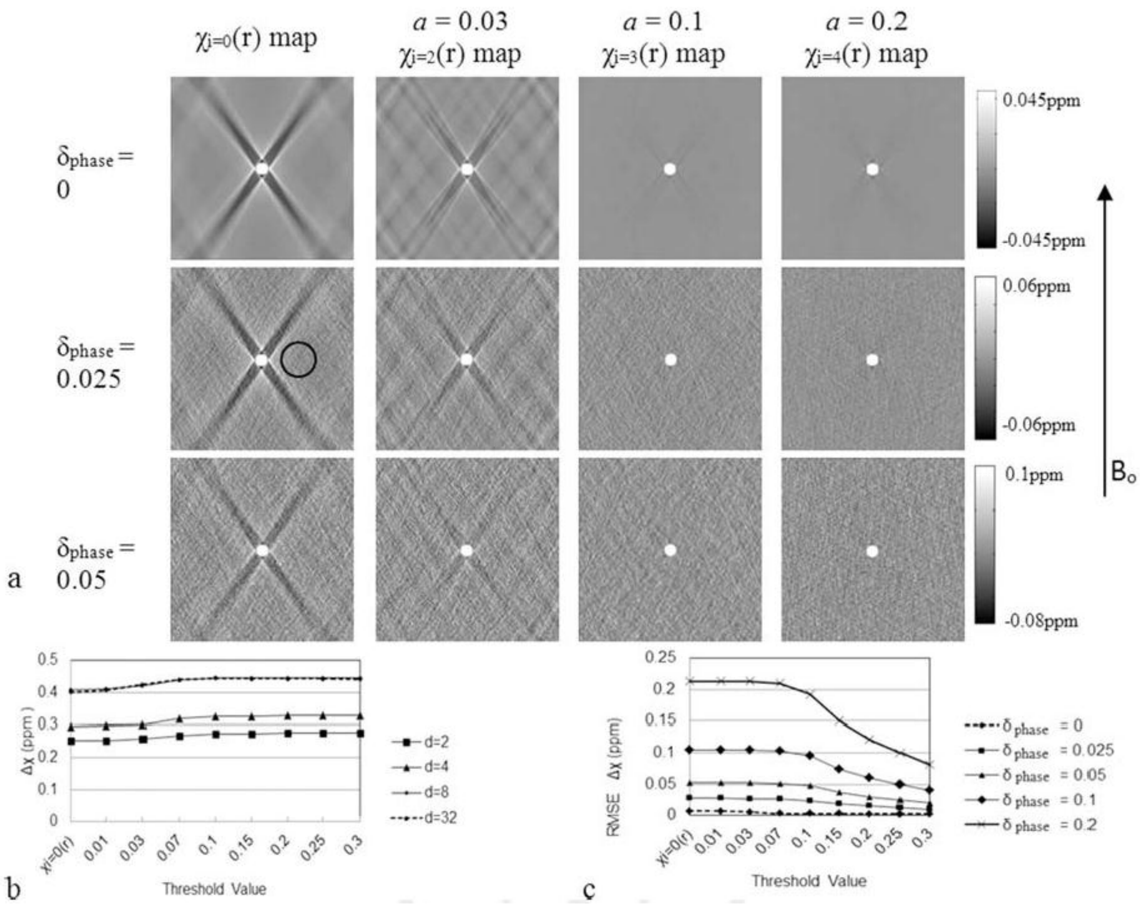

**Figure 4:** Simulations showing the comparison of the calculated susceptibility distributions for a cylinder perpendicular to $B_o$ at different threshold values ($a$) applied to g(k) as well as the initial $\chi_{i=0}$(r)map. The direction of $B_o$ is indicated by a black long arrow. The susceptibility, $\Delta\chi$, inside the cylinder is 0.45 ppm. a) The comparison of the converged $\chi_{i=b}$(r) map with the $\chi_{i=0}$(r) map for a diameter of 32-pixel cylinder, where $b$ is the iterative step required to reach convergence. In this data, $b$ = 2 when $a$ = 0.03, $b$ = 3 when $a$ = 0.1 and $b$ = 4 when $a$ = 0.2when $\sigma_{phase}$ = 0. The top row of images shows simulations with no phase noise. The second and the third row show simulations with added phase noises $\sigma_{phase}$ = 0.025 and 0.05 radians, respectively. The first column of images show initial $\chi_{i=0}$(r)maps for reference. b) The variation of the mean calculated susceptibility inside the cylinder with different threshold value, $a$, for diameter (d) = 2, 4, 8 and 32 pixels cylinders. The mean susceptibility value is independent of the noise level; therefore, only mean values from $\sigma_{phase}$ = 0 were provided. c) The variation of the RMSE of the susceptibility values outside the cylinder as a function of the threshold value, $a$, and the noise level. The d=32 pixels cylinder was used to generate (c).

***Selection of the Optimal Iterative Step:*** The inverse process [18] was applied to the dipole field in Fig. 5a to give $\chi_{i=0}(r)$ map shown in Fig. 5b with prominent streaking artifacts. Streaking artifacts are significantly reduced at each step of the iterative method quickly reaching convergence (Figs. 5c to 5e). The largest improvement is seen in the first iterative step, which is verified by Fig. 5f, showing the difference between Fig. 5c ($\chi_{i=1}(r)$ map) and Fig. 5b ($\chi_{i=0}(r)$ map). After the second iteration, we can see some minor streaking reductions (Fig. 5g, the difference between the $\chi_{i=1}(r)$ map and $\chi_{i=2}(r)$ map). The mean susceptibility value approaches 0.44ppm in a single step. Similar results (not shown) are also obtained when the iterative method is run with different aspect ratios between the in-plane resolution and the through plane resolution (such as 1:2 and 1:4). The iterative results always lead to higher final susceptibility values compared to the initial value in $\chi_{i=0}(r)$. Finally, even when an HP filter is applied, up to a 10% increase in the susceptibility is realized (Fig. 5i). The SMs of large vessels benefit from a low order HP filter (FWMH = 4 pixels) and small vessels up to 8 pixels benefit from a HP filter (FWMH = 16 pixels).

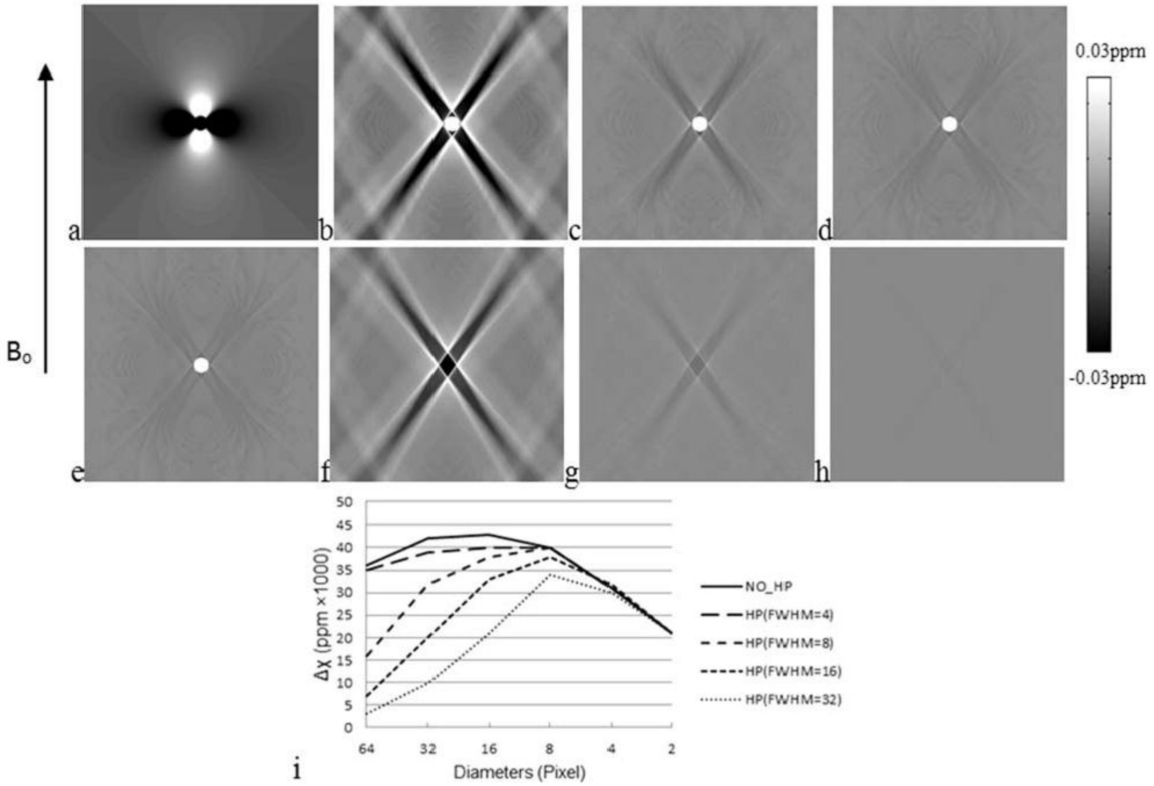

**Figure 5:** a) Phase images from a cylinder with a diameter of 32 pixels are simulated with: $\Delta\chi$=0.45ppm, Bo=3T and TE=5ms. The cylinder is perpendicular to the main field. No thermal noise was added in these images. b) The initial $\chi_{i=0}(r)$ map. c) The SM from the first iteration, $\chi_{i=1}(r)$ map, d) $\chi_{i=2}(r)$ map and e) $\chi_{i=3}(r)$ map using threshold value $a$ = 0.1. The SM has converged at $\chi_{i=3}(r)$ map. The streaking artifacts are reduced as the number of iterative steps increases. f) The difference image of c) subtracted from b) illustrates that the streaking artifacts were reduced by the iterative procedure and the largest improvement happens in this first iterative step. g) The difference image of the $\chi_{i=1}(r)$ map subtracted from the $\chi_{i=2}(r)$ map indicates that the streaking artifacts were further reduced by the second iterative step. h) The difference image of $\chi_{i=2}(r)$ map subtracted from $\chi_{i=3}(r)$ map shows much less improvement at the third iterative step. Thus it indicates a convergence of the iterative procedure. All images were set to the same window level setting for direct comparisons and for enhancing the presence of the streaking and the remnant error. i) The effect of the iterative approach on the changes in susceptibility values from HP filtered phase images. Differences between the values in iterative and non-iterative susceptibility map reconstruction (i.e. $\chi_{converged}(r)$ - $\chi_{i=0}(r)$) from HP filtered phase images are plotted for different filter sizes. Results for four filter sizes (FWHM = 4, 8, 16 and 32 pixels) are shown here. Applying an HP filter leads to an underestimation of

$\Delta\chi$ [18]. The iterative approach helps to improve the accuracy of the estimated susceptibility values.

### *Effect of the Iterative Approach on Surrounding Brain Tissues in the 3D Brain Model:*

#### *a) SM Reconstruction using a vessel mask only*

Figs. 6a and 6d represent $\chi_{i=0}(r)$, without noise and with 0.025 radians of noise in phase images. Fig. 6f is the vessel map. Streaking artifacts (pointed by black arrows) are obvious in Figs. 6a and 6d and completely disappeared in the $\chi_{i=3}(r)$ maps (Figs. 6b and 6e) using $a$ = 0.1. Fig. 6c is the $\chi_{i=3}(r)$ map using $a$ = 0.2. As can be seen, when $a$ increases, the iterative method still works for vessels, but brain tissues become more blurred. Fig. 7a plots the mean susceptibility values inside the vessel (vein of Galen), GP, SN, RN, PUT and CN from $\chi_{i=3}(r)$ maps generated by using $a$=0.1, 0.15, 0.2, 0.25 and 0.3, respectively. The susceptibility value in the brain model and $\chi_{i=0}(r)$ map are also provided in the plot as references. Generally, the susceptibility values of brain tissues except vessels decrease as $a$ increases while, for vessels, the susceptibility value is 0.41ppm in the $\chi_{i=0}(r)$ map and increased to 0.45ppm in the $\chi_{i=3}(r)$ maps.

#### *b) SM Reconstruction using a mask including vessels and brain structures*

Besides veins, the iterative method can be also applied to brain tissues. Figure 6g shows a coronal view of the $\chi_{i=0}(r)$ map for the brain model. The $\chi_{i=3}(r)$ map using a mask keeping all major structures (GP, SN, RN, PUT, CN) and vessels is shown in Fig. 6h. In practice, this is equivalent to setting thresholds in the $\chi_{i=0}(r)$ map to be greater than 0.09ppm to extract all these high susceptibility structures from the $\chi_{i=0}(r)$ map to create the mask. Fig.

6h reveals that streaking artifacts associated with veins as well as all major structures have been reduced. Fig. 6i shows the difference between Fig. 6g and 6h. In addition, streaking artifacts sometimes cause the appearance of "false" structures. For instance, there is no internal capsule (IC) included in the model (Fig. 6l), yet we see a IC like structure in the $\chi_{i=0}$(r)map (Fig. 6j) (indicated by a dashed white arrow in Figs. 6j to 6l). The iterative method removes the streaking artifacts and the "false" IC (Fig. 6k).

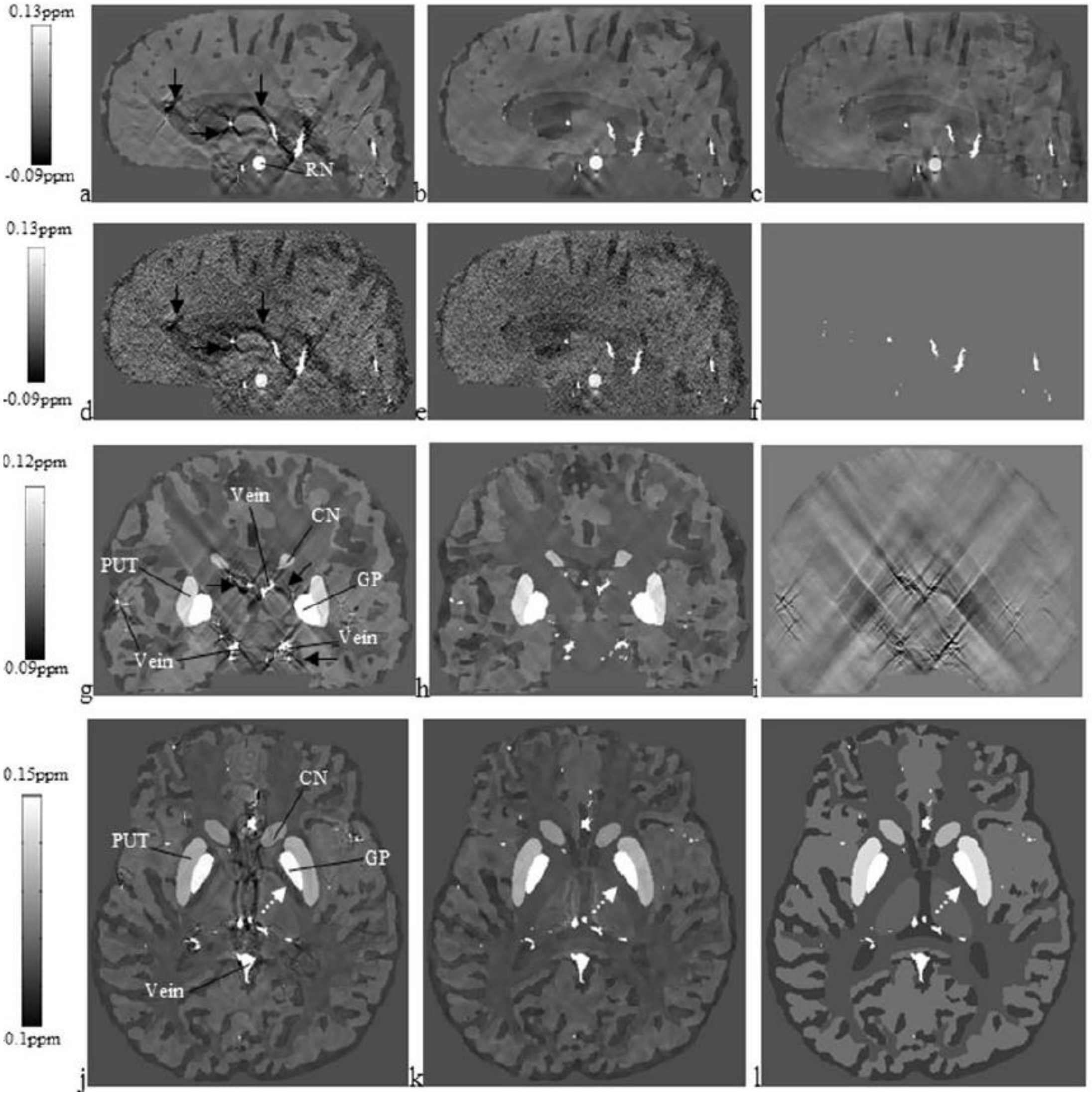

**Figure 6:** Results before and after the iterative method using a region of interest map which consists of either only vessels or specific brain structures (in this case the basal

ganglia) plus vessels. a) The initial $\chi_{i=0}(r)$ map without noise added in the original simulated images. b) $\chi_{i=3}(r)$ map of (a) using threshold value *a*=0.1. c) Similar to (b), *a*=0.2. d) The initial $\chi_{i=0}(r)$ map with noise added in original images, resulting a standard deviation of 0.025 radian in phase images. e) $\chi_{i=3}(r)$ map of (d) using *a*=0.1. f) The associated vessel map. g) The $\chi_{i=0}(r)$map in the coronal plane as a reference. The streaking artifacts are clearly shown in every structure. h) The $\chi_{i=3}(r)$maps created by using a region of interest map which consists of GP, SN, RN, PUT, CN and vessels. i) The difference image of (g) and (h). j)The initial $\chi_{i=0}(r)$ map in the transverse plane has "fake" internal capsule (IC) (pointed by an arrow) around GP; k) The $\chi_{i=3}(r)$map shows no "IC." This matches the originally simulated model (l). No noises were added to images from (g) to (l).

Fig. 7b shows susceptibility values in each structure in the brain model for $\chi_{i=0}(r)$and $\chi_{i=3}(r)$when the mask includes vessels and all major structures. The underestimated susceptibility values of all major structures and vessels in the $\chi_{i=0}(r)$map have been recovered by the iterative method in the $\chi_{i=3}(r)$map.

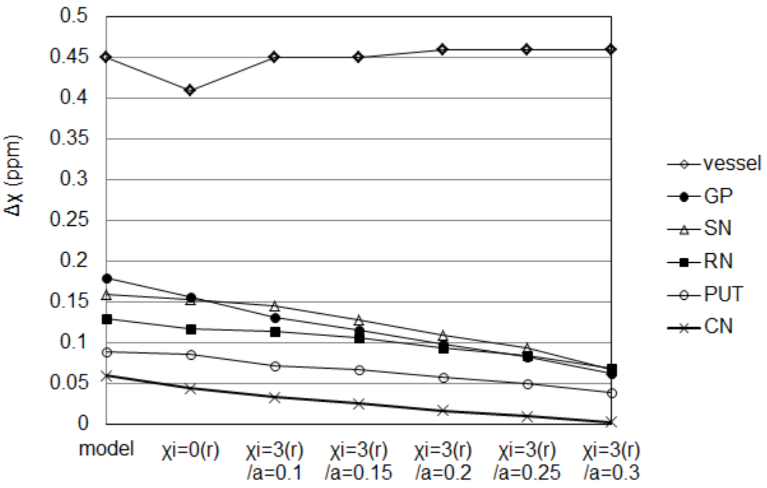

a

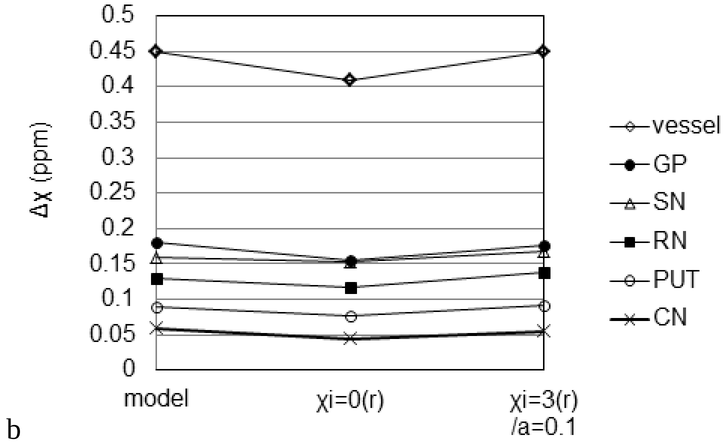

**Figure 7:** The plots of mean susceptibility values inside the vessel (vein of Galen), GP, SN, RN, PUT and CN from $\chi_{i=3}(r)$ maps. The first two data points of each curve is the value inside each structure from the brain model and the $\chi_{i=0}(r)$ map, respectively. a) $\chi_{i=3}(r)$ maps generated by applying a region of interest map which consists only vessels using *a*=0.1, 0.15, 0.2, 0.25 and 0.3, respectively. b) $\chi_{i=3}(r)$ maps generated by applying a region of interest map which consists of the GP, SN, RN, PUT, CN and vessels using *a*=0.1.

***Effect of Errors in the Vessel Map*****:** Accurately extracting vessels from $\chi_{i=0}(r)$is critical for the iterative method. Figs. 8b-8d and the corresponding enlarged views (Figs. 8f-8h) from the rectangular region indicated in Fig. 8a, show the $\chi_{i=3}(r)$ maps using an accurate (Fig. 8j), a dilated (Fig. 8k) and an eroded (Fig. 8l) vessel map to show the effect of errors in the vessel mask on $\chi_{i=3}(r)$map. The dilated and eroded vessel maps were generated using Matlab functions based on a 3-by-3 square structuring element object. The susceptibility values measured from a vein indicated by a white arrow in Fig. 8e are 0.40±0.03ppm (Fig. 8e), 0.45±0.03ppm (Fig. 8f), 0.45±0.03ppm (Fig. 8g) and 0.40±0.07ppm (Fig. 8h), respectively. The iterative method still works if the vessel is slightly enlarged but does little if the vessels are not present. As we just discussed, streaking artifacts produced "fake" vessels indicated by a dashed black arrow in Fig. 7e since these vessels are not in the model (Fig. 8i). These fake vessels disappeared in Fig. 8f.

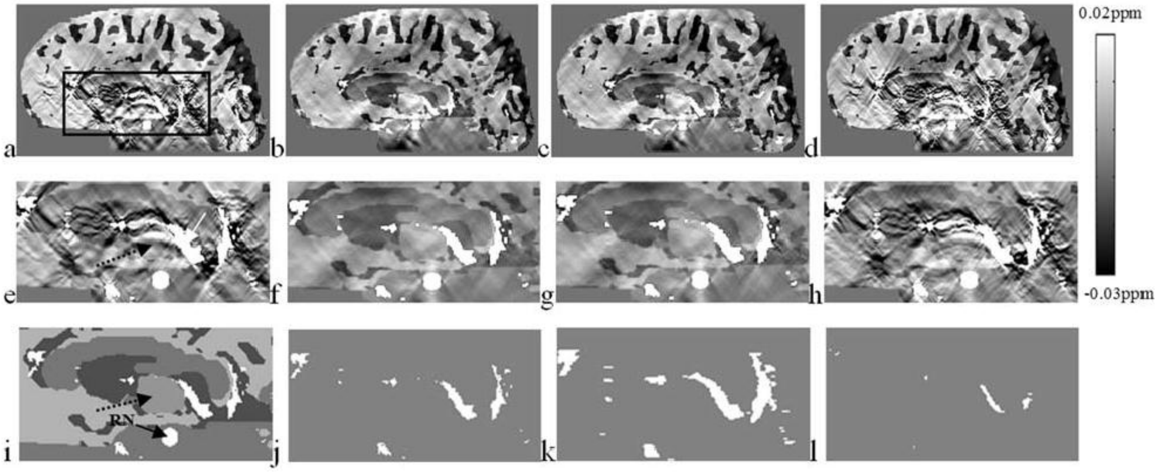

**Figure 8:** Comparison of the reconstructed $\chi_{i=3}$(r) maps using j) accurate, k) dilated and l) eroded vessel maps. Their corresponding vessel maps and the enlarged views from the rectangular regions are provided in b) – d) and f) – h). a) and e) The initial $\chi_{i=0}$(r)maps and i) the original brain model as references. The circle in the midbrain in the $\chi$(r) maps represents the red nucleus (RN) and is indicated by a black arrow in i). Other hyper-intense regions in SMs are vessels.

***Results from the in vivo Dataset:*** In the *in vivo* example, we compare the differences between SHARP (Figs. 9a to 9d) and a homodyne HP filter (FWHM = 16 pixels) (Figs. 9e to 9h). Compared to the transverse view, streaking artifacts are more obvious in the sagittal or coronal view. Fig. 9a shows $\chi_{i=0}$(r)map with severe streaking artifacts. The streaking artifacts were significantly reduced in $\chi_{i=3}$(r)map (Fig. 9b) using *a*=0.1. The streaking artifacts associated with the superior sagittal sinus vein (indicated by two black arrows in Fig. 9a) were significantly decreased in Figs. 9b and 9d. The subtracted image (Fig. 9c), of Fig. 9b from Fig. 9a, reveals the removed streaking artifacts. These streaking artifacts are one of the reasons why the $\chi_{i=0}$(r) maps appear noisy. In the $\chi_{i=3}$(r) map, the reduction in streaking artifacts from individual veins leads to a decrease of noise therefore an increased SNRs of veins. If veins are the only interest, even a threshold of 0.2 can work reasonably well (Fig. 9d). Two relative big veins, V1 and V2, indicated by a white dashed and a white solid arrow, respectively, in Fig. 9b, were chosen to measure the susceptibility values. Results are provided in Table 1. The susceptibility values of these two veins have been improved by roughly 16% by the iterative method. The standard deviation of the susceptibility values measured from a uniform region inside the white matter decreased from 0.042 ppm in $\chi_{i=0}(r)$map to 0.035ppm and 0.023ppm in the $\chi_{i=3}(r)$map with a=0.1 and 0.2, respectively. The baseline susceptibilities of the major structures are higher with SHARP than with an HP filter. Iterative method works for brain structures also when the structure is included in the mask. For instance, the mean susceptibility values of GP and SN have been increased from 0.155±0.058 ppm and 0.162±0.067ppm in $\chi_{i=0}(r)$ map to 0.163±0.070ppm and 0.186±0.083ppm in $\chi_{i=3}(r)$ map, from the dataset processed using SHARP. The result after the HP filtering (Fig. 9e) shows more edge artifacts indicated by a left arrow in Fig.9e. Much of this error was reduced by the iterative method (Fig. 9f). It seems that the iterative method compensated for the worse first guess (Fig. 9e) and ended up with almost the same result (Figs. 9f and 9h) as having started with SHARP (Fig. 9b and 9d) from image perspective. Since a small size of HP filter cannot remove rapid phase wrapping at air-tissue interfaces; we have to cut out the region near the sinuses in the phase images.

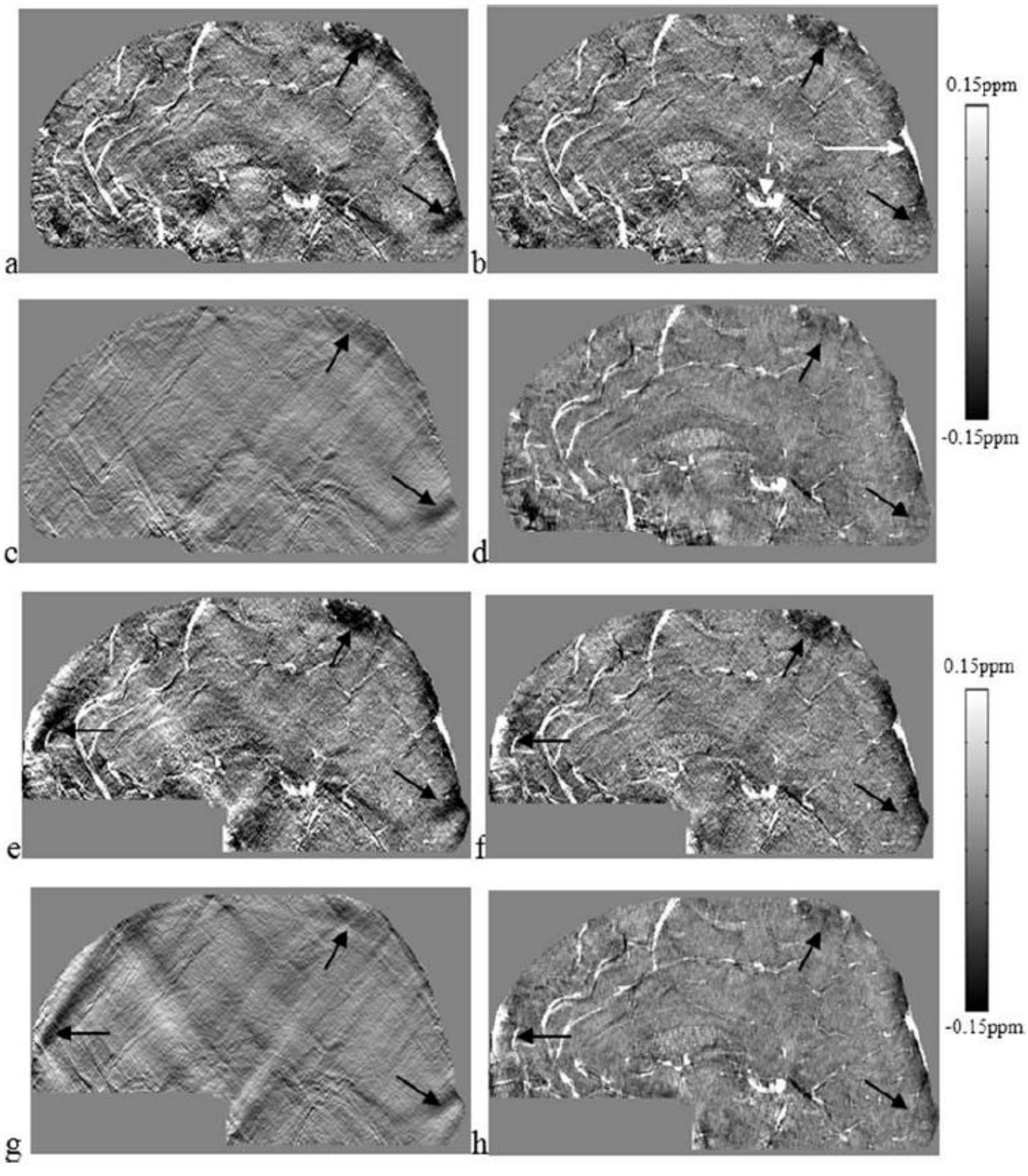

**Figure 9:** Comparisons of SMs using SHARP or a HP filter (FWHM = 16 pixels) to remove the background field. The iterative method with *a* = 0.1 and 0.2 is applied after the background is removed. a – d) and e - h) are results after the application of SHARP and the HP filter, respectively. a) and e) the initial $\chi_{i=0}(r)$ maps. b) and f) The $\chi_{i=3}(r)$ maps generated from the iterative method with *a* = 0.1. c) and g) The differences of images between (a) and (b), and between (e) and (f), respectively. These two images show the

successful reduction of the streaking artifacts. d) and h) The $\chi_{i=3}(r)$ maps generated from the iterative method with *a* = 0.2.

**Table 1**

$\Delta\chi$ measured *in vivo* in two veins in $\chi_{i=0}(r)$ maps and $\chi_{i=3}(r)$ maps with different threshold values

| | $\chi_{i=0}(r)$ map | $\chi_{i=3}(r)$ map / a=0.1 | $\chi_{i=3}(r)$ map / a=0.2 |
|---|---|---|---|
| V1 (SHARP) | 0.32 ± 0.07 | 0.37 ± 0.08 | 0.38 ± 0.09 |
| V1 (HP) | 0.24 ± 0.05 | 0.28 ± 0.06 | 0.28 ± 0.06 |
| V2 (SHARP) | 0.35 ± 0.04 | 0.40 ± 0.05 | 0.41 ± 0.05 |
| V2 (HP) | 0.25 ± 0.05 | 0.31 ± 0.06 | 0.30 ± 0.06 |

Mean and standard deviation for the susceptibility values (in ppm) of two veins processed using SHARP and a HP filter (FWHM = 16 pixels), respectively, were chosen from the 0.5 mm isotropic resolution data. V1 and V2 are shown in Fig. 9. The susceptibility values of these two veins have been increased by the iterative method. There is not much variation of the susceptibility value with different threshold values.

## 4.4 Discussion

In this article, a threshold-based k-space/image domain iterative approach has been presented. Simulations and *in vivo* results show that the ill-posed problems of streaking artifacts and biases in the estimates of susceptibilities can be significantly reduced. The replacement of the$\chi(k)$ values near the singularities by $\chi_{vm}(k)$, which is obtained from the geometric information from the $\chi(r)$ map itself, obviates many of the current problems seen in the TBSO methods. Since $\chi_{vm}(r)$ contains little streaking artifacts itself, the values used inside the thresholded regions in $\chi(k)$ now contain no artifacts either. In this sense, we obtain an almost “perfect” k-space without “bad” data points in the region of singularities anymore. This explains why this method converges very fast and the major improvement is in the first iterative step (Fig. 5).

The proposed iterative approach is different from the other threshold based methods [11,15,18,19,24] which fill pre-defined conical region using an constant, zero or 1/*thr* [11, 15, 24] or the first-order derivation of $g^{-1}(k)$ [19]. The iterative method uses full geometry information from the SM (vessels or pre-defined structures and not edge information) to iteratively change k-space values in the conical region using the forward model. This is also quite different than other currently proposed solutions [9, 12, 20, 22]. Even though spatial priors such as gradients of the magnitude are used [9, 12, 20, 22], in those methods, the meaningful values of the singularity regions in k-space are obtained through solving the complex cost function problem. However, the iterative method uses priors not from the magnitude image but from the SM. The missing data in the singularity regions are obtained through iterating back and forth between the SMs and their k-space. The advantage of cost function approaches is that they do not need to pre-define the singularity region in k-space which is solved by the optimization process automatically (although the optimization process itself is usually quite time-consuming). On the other hand, the iterative method is the time-efficient. It is fast enough to reconstruct SMs for a 512 × 512 × 256 data set using an Intel Core i7 CPU 3.4GHz processor in less than 30 seconds, since in practice usually 3 iterations are good enough to generate decent results.

The threshold value also plays a key role. A threshold value of 0.1 is a reasonable choice since a lower threshold value leads to an increase in noise and a higher threshold value leads to a blurring of the object (Fig. 6c, Figs. 9d and 9h).

It is known that the ill-posedness of the inverse filter will increase the noise level from the phase to the SM. Based on both simulations and real data, we find that there is a factor of 4 increase in noise in the SM relative to the original phase data. This result and the fact that at Bo = 3T, TE = 5ms and $\sigma_{\chi i=0(r)}$ = 0.025ppm, make it possible to write the total noise in the background regionin $\chi_{i=0}(r)$ as $0.025\cdot4\cdot(3/B_o)\cdot(5/TE)$ in ppm. The noise error in $\chi_{i=3}(r)$will be less than this value since the iterative method will reduce streaking artifact in SM.

The iterative method can be used to remove streaking artifacts associated with not only vessels but also other brain structures as well. Fig. 6h shows a reduction in artifacts associated specifically with iron-rich regions such as the GP and CN.

Accurately extracting vessels from the $\chi_{i=0}(r)$ map is critical for the iterative method (Fig. 8). In this study, vessels were segmented directly from the SM (Fig. 2). It may also possible to segment veins from original magnitude images [9,12,20,22], phase images and/or SWI images. Extraction of accurate anatomic information from phase data sometimes is difficult since phase is orientation dependent and phase changes are generally nonlocal. SWI images work better for an anisotropic dataset rather than an isotropic dataset since phase cancellation is needed to highlight vessel information. Therefore, we may consider combining SMs with magnitude images, phase images and/or

SWI images together to segment the veins, since different types of image can compensate for missing information.

The iterative method appears to help even in the presence of non-isotropic resolution with partial volume effects and to a minor degree when an HP filter is applied. A smaller sized HP filter would be better, since a larger HP filter will significantly underestimate the susceptibility value (Table 1). SHARP gave us better results compared with HP filter (FWHM=16 pixels) (Fig. 9), but SHARP requires phase unwrapping which can be time consuming and noise dependent [19]. From this perspective, an HP filter has the advantage since it does not need unwrapped phase. If the forward modeling approach of Neelavalli et al [37] can be used to reduce air/tissue interface fields, then it may be possible to use a small size HP filter (FWHM=8 pixels) which may provide similar results to SHARP.

Severe streaking artifacts associated with structures having high susceptibility values such as veins can lead to major changes in the appearance of the brain structures with low susceptibility. Practically, the susceptibility of the veins is a factor of 2.5 to 20 times higher than other structures in the brain. Therefore, even a 10% streaking artifact can overwhelm the information in the rest of the brain and create false appearing structures as in (Fig. 6j) and in (Fig. 8e). The reduction of these artifacts makes a dramatic difference in the ability to properly extract the susceptibility of other tissues.

In conclusion, both simulations and human studies have demonstrated that the proposed iterative approach can dramatically reduce streaking artifacts and improve the accuracy of susceptibility quantification inside the structures of interest such as veins or other brain tissues. Given its fast processing time, it should be possible to expand its use into more daily clinical practice. With the improved accuracy of the susceptibility values inside veins, this method could potentially be used to improve quantification of venous oxygen saturation [18].

## References

1. Haacke EM, Mittal S, Wu Z, Neelavalli J, Cheng YC. Susceptibility-weighted imaging: technical aspects and clinical applications, part 1. AJNR Am J Neuroradiol. 2009; 30:19-30.
2. Mittal S, Wu Z, Neelavalli J, Haacke EM. Susceptibility-weighted imaging: technical aspects and clinical applications, part 2. AJNR Am J Neuroradiol. 2009; 30: 232-52.
3. Haacke EM, Reichenbach JR. Susceptibility Weighted Imaging in MRI: Basic Concepts and Clinical Applications. New Jersey: John Wiley & Sons, Hoboken; 2011.
4. Duyn JH, van Gelderen P, Li TQ, de Zwart JA, Koretsky AP, Fukunaga M. High-field MRI of brain cortical substructure based on signal phase. Proc Natl Acad Sci U S A 2007;104:11796-11801
5. Haacke EM, Lai S, Yablonskiy DA, Lin W. In-vivo validation of the BOLD mechanism: a review of signal changes in gradient-echo functional MRI in the presence of flow. International Journal of Imaging Systems and Technology 1995; 6:153-163
6. Rauscher A, Sedlacika J, Barthb M, Mentzela HJ, Reichenbacha JR. Magnetic susceptibility-weighted MR phase imaging of the human brain. AJNR Am J Neuroradiol. 2005; 26:736-42
7. Haacke EM, Cheng NY, House MJ, Liu Q, Neelavalli J, Ogg RJ, Khan A, Ayaz M, Kirsch W, Obenaus A. Imaging iron stores in the brain using magnetic resonance imaging. Magn Reson Imaging 2005; 23: 1-25.
8. Koch KM, Papademetris X, Rothman DL, de Graaf RA. Rapid calculations of susceptibility-induced magnetostatic field perturbations for in vivo magnetic resonance. Phys Med Biol 2006; 51: 6381-6402.
9. de Rochefort L, Brown R, Prince MR, Wang Y. Quantitative MR susceptibility mapping using piece-wise constant regularized inversion of the magnetic field. Magn Reson Med 2008; 60: 1003-1009.
10. Cheng YC, Neelavalli J, Haacke EM. Limitations of calculating field distributions and magnetic susceptibilities in MRI using a Fourier based method. Phys Med Biol 2009; 54: 1169-1189.
11. Wharton S, Schafer A, Bowtell R. Susceptibility mapping in the human brain using threshold-based k-space division. Magn Reson Med 2010; 63: 1292-1304.
12. Wharton S, Bowtell R. Whole-brain susceptibility mapping at high field: a comparison of multiple- and single-orientation methods. Neuroimage 2010; 53: 515-525.

13. Schweser F, Deistung A, Lehr BW, Reichenbach JR. Differentiation between diamagnetic and paramagnetic cerebral lesions based on magnetic susceptibility mapping. Med Phys 2010; 37: 5165-5178.
14. Kressler B, de Rochefort L, Liu T, Spincemaille P, Jiang Q, Wang Y. Nonlinear regularization for per voxel estimation of magnetic susceptibility distributions from MRI field maps. IEEE Trans Med Imaging 2010; 29: 273-281.
15. Shmueli K, de Zwart JA, van Gelderen P, Li TQ, Dodd SJ, Duyn JH. Magnetic susceptibility mapping of brain tissue in vivo using MRI phase data. Magn Reson Med 2009; 62: 1510-1522.
16. Schafer A, Wharton S, Gowland P, Bowtell R. Using magnetic field simulation to study susceptibility-related phase contrast in gradient echo MRI. Neuroimage 2009; 48: 126-137.
17. Liu T, Spincemaille P, de Rochefort L, Kressler B, Wang Y. Calculation of susceptibility through multiple orientation sampling (COSMOS): a method for conditioning the inverse problem from measured magnetic field map to susceptibility source image in MRI. Magn Reson Med 2009; 61: 196-204.
18. Haacke EM, Tang J, Neelavalli J, Cheng YC. Susceptibility mapping as a means to visualize veins and quantify oxygen saturation. J Magn Reson Imaging 2010; 32: 663-676.
19. Li W, Wu B, Liu C. Quantitative susceptibility mapping of human brain reflects spatial variation in tissue composition, NeuroImage 2011; 55: 1645-1656.
20. Liu T, Liu J, de Rochefort L, Spincemaille P, Khalidov I, Ledoux JR, Wang Y, Morphology enabled dipole inversion (MEDI) from a single-angle acquisition: Comparison with COSMOS in human brain imaging. Magn Reson Med 2011; 66: 777-783.
21. Li L, Leigh JS, Quantifying arbitrary magnetic susceptibility distributions with MR. Magn Reson Med 2004; 51: 1077-1082.
22. de Rochefort L, Liu T, Kressler B, Liu J, Spincemaille P, Lebon V, Wu J, Wang Y, Quantitative susceptibility map reconstruction from MR phase data using bayesian regularization: validation and application to brain imaging. Magn Reson Med 2010; 63: 194-206.
23. Li Y, Xu N, Fitzpatrick JM, Morgan VL, Pickens DR, Dawant BM, Accounting for signal loss due to dephasing in the correction of distortions in gradient-echo EPI via nonrigid registration. IEEE Trans Med Imaging 2007; 12:1698-1707.
24. Grabner G, Trattnig S, Barth M. Filtered deconvolution of a simulated and an in vivo phase model of the human brain. J Magn Reson Imaging 2010; 32: 289-297.
25. Deville G, Bernier M, Delrieux J. NMR multiple echoes observed in solid 3He. Phys Rev B 1979; 19: 5666-5688.

26. Marques JP, Bowtell R. Application of a Fourier-based method for rapid calculation of field inhomogeneity due to spatial variation of magnetic susceptibility. Concepts Magn Reson B Magn Reson Eng 2005; 25B:65-78.
27. Salomir R, De Senneville BD, Moonen CTW. A fast calculation method for magnetic field inhomogeneity due to an arbitrary distribution of bulk susceptibility. Concepts Magn Reson B Magn Reson Eng 2003; 19B: 26-34.
28. Hagberg GE, Welch EB, Greiser A. The sign convention for phase values on different vendor systems: definition and implications for susceptibility weighted imaging. Magn Reson Imaging 2010; 28: 297-300.
29. Demmel JW. Perturbation theory for the least squares problem. Applied numerical linear algebra. Berkeley, CA: SIAM; 1997. 117-118 p.
30. Spees WM, Yablonskiy DA, Oswood MC, Ackerman JJ. Water proton MR properties of human blood at 1.5 Tesla: magnetic susceptibility, T(1), T(2), T*(2), and non-Lorentzian signal behavior. Magn Reson Med 2001; 45:533-542.
31. Haacke EM, Brown RW, Thomson MR, Venkatesan R, Magnetic Resonance Imaging. Physical Principles and Sequence Design, New York: John Wiley & Sons; 1999. 766 p.
32. Hoffman RE. Measurement of magnetic susceptibility and calculation of shape factor of NMR samples. J Magn Reson 2006; 178: 237-247.
33. Reichenbach JR, Venkatesan R, Schillinger DJ, Kido DK, Haacke EM. Small vessels in the human brain: MR venography with deoxyhemoglobin as an intrinsic contrast agent. Radiology 1997; 204: 272-277.
34. Smith SM, Fast robust automated brain extraction. Hum Brain Map 2002; 17: 143-155.
35. Schweser F, Deistung A, Lehr BW, Reichenbach JR. Quantitative imaging of intrinsic magnetic tissue properties using MRI signal phase: an approach to in vivo brain iron metabolism?.Neuroimage 2011; 54:2789-2807.
36. Pandian DS, Ciulla C, Haacke EM, Jiang J, Ayaz M. Complex threshold method for identifying pixels that contain predominantly noise in magnetic resonance images. J Magn Reson Imaging 2008; 28:727-735.
37. Neelavalli J, Cheng YCN, Jiang J, Haacke EM. Removing background phase variations in susceptibility weighted imaging using a fast, forward-field calculation. J Magn Reson Imaging 2009; 29: 937-948.

# Chapter 5: Conclusions and Future Directions

## 5.1 Conclusions

Knowledge of the oxygen saturation of venous blood is important to characterize the physiological or pathological state of blood supply or oxygen consumption in tissue. This is especially true in the human brain where there is a strong clinical demand for noninvasive and reliable oxygenation quantification. The clinical need is to better understand the changes in cerebral hemodynamics due to neuronal activation and/or improve the characterization and monitoring of treatment of cerebral pathologies, such as stroke or tumors (1). Several methods are available for quantification of cerebral oxygen saturation. These methods, however, either have low spatial resolution (near infrared spectroscopy – NIRS), or are invasive by inserting a catheter; or the technique is quite expensive and not ubiquitously available ($^{15}$O-PET). In contrast to these methods, which measure tissue oxygen saturation, the MR method introduced here relies on the oxygenation level of venous blood due to the difference of its magnetic property in the oxygenated and deoxygenated state. The smaller the veins that can be probed, the closer one comes to a more local estimate of tissue oxygen saturation.

The basic concept of using a simple Fourier transformation method to predict the magnetic field distribution from a single acquisition approach given the susceptibility distribution was described first by Deville at al. (2). However, the inverse problem, i.e., obtaining the source susceptibility distribution from magnetic field measurements, is more complicated. Of course, one of the major advantages of this approach is that we can make these measurements independent of the body's position in the magnet. A primary difficulty is that high values of the inverse filter, 1/g(k) where g(k)= $\frac{1}{3}-\frac{k_z^2}{K^2}$, lead to streaking artifacts and noise amplification in the images reconstructed by the inverse filter. Such problematic high values of 1/g(k) occur where g(k) is close to or equal to zero, namely, on or near a conical region in k-space at the magic angles (i.e., 54.7° and 125.3° from the $B_o$ axis).

In Chapter 3, we proposed a regularized inverse filter, $1/g_{reg}(k)$ to solve the ill-posed problem associated with 1/g(k). The regularized form of $1/g_{reg}(k)$ that we proposed appears to work fairly well in simulations. Generally, the systematic errors depend on the object size (Figs. 1 and 3 in Ch. 3) with smaller vessels showing smaller values due to partial volume effects. Larger vessels show a bias toward a reduced susceptibility approaching 90% of the expected value. We found that there are six major sources of error in creating venous susceptibility maps which are: i) errors in the inversion process, i.e., those due to $g^{-1}_{reg}(\mathbf{k})$ itself; ii) voxel aspect ratio affects and partial voluming; (iii) aliasing in input phase images caused by longer echo times; (iv) errors caused by high pass filtered phase data; v) errors due to discrete sampling in MRI and vi) thermal noise in the phase data. These errors affect the susceptibility quantification. For instance, high-pass filtering the phase has a strong influence on the quantitative accuracy of the susceptibility values (see Fig. 4 in Ch. 3). Fortunately, for vessels that are on the order of 5 mm wide or less (i.e., 10 voxels or less), the error is only 15% for a filter size of 32 × 32. Most of the veins in the brain lie close to or less than this diameter. For a filter size of 64 × 64, the error increases to 28%. This prediction is close to what we see from the real data where we used a 64 × 64 filter size. The typical value measured in veins *in vivo* is around 0.3 ppm (Table 3, Ch. 3) which is about 67% of the physiologically expected normal value of 0.45 ppm. Partial volume effects can cause a complete loss of phase information when the vein is much smaller than the slice thickness(3). This leads to the issue of lower than expected susceptibilities. The susceptibility map theoretically is independent of the choice of echo time (See Fig. 8 and Table 2 in Ch. 3). However, the effect of echo time is complicated since longer echo times will lead to aliasing around the vein. This aliasing coupled with partial volume effects creates a nonphysical phase at the edge of the object which will cause errors in the estimated susceptibility values.

To reconstruct a susceptibility map of venous vessels in an *in vivo* dataset with minimal artifacts, we proposed the following steps: i) collect an isotropic high resolution SWI data set, ii) high pass filter the phase images, iii) interpolate k-space, iv) remove spurious phase noise sources from the phase images and v) regularize the data. Each step is to improve the quality of SMs. For instance, using a high resolution dataset (step i) reduces partial volume effects and Gibbs ringing. This should help in improving quantitative accuracy of the susceptibility values for small vessels and make it possible to probe a more local region of tissue to understand tissue function. With the advent of high fields such as 7T, imaging resolution can be reduced in plane to 200μ quite practically. Using shorter echo times may be viable with high resolution and the subsequent image quality improvement. The imaging time can also be reduced thanks to the shorter TRs available with the TEs. This should open the door to studying veins on the order of 1mm. Finally, shorter echo times also reduce aliasing effects.

To improve the accuracy of SM and reduce the streaking artifacts in SM, a k-space iterative method was proposed in Chapter 4. This method replaced the values near the singularities in k-space by the corresponding values from the geometric information from the SM itself. The missing data in the singularity regions were obtained through iterating back and forth between the image domain, i.e., the SMs, and their k-space domain. The iterative method is the most time-efficient approach. It is fast enough to reconstruct SMs for a 512 × 512 × 256 data set using an Intel Core i7 CPU 3.4GHz processor in less than 30 seconds, since in practice usually 3 iterations are good enough to generate decent results. According to simulations, the bias toward lower mean susceptibility values inside vessels has been shown to decrease from around 10% to 2% when choosing an appropriate threshold value for the proposed iterative method (Fig. 4 in Ch. 4). The proposed iterative method can not only improve quantification of susceptibility inside vessels but also reduce streaking artifacts throughout the brain (Figs. 5, 6 and 9 in Ch. 4).Severe streaking artifacts associated with structures having high susceptibility values such as veins can lead to major changes in the appearance of brain structures with low susceptibility. Practically, the susceptibility of the veins is a factor of 2.5 to 20 times higher than other structures in the brain. Therefore, even a 10% streaking effect can overwhelm the information in the rest of the brain and create false appearing structures as in (Figs. 6j and 8e in Ch. 4). The reduction of these artifacts makes a dramatic difference in the ability to properly extract the susceptibility of other tissues. Although, in this thesis, we focus on vessels, the iterative methods can be applied to other brain tissues, for instance basal ganglia, as well which could help to better quantify iron contents inside these structures. With the improved accuracy of the susceptibility values inside veins, this iterative method could potentially be used to improve quantification of venous oxygen saturation. Following up on the comments regarding shorter echo times, faster imaging and higher resolution, with the resulting need for reduced high pass filter matrix sizes and subsequent improvement in baseline phase values, it would seem that susceptibility mapping would benefit most from a combination of all three of these approaches.

Errors in the susceptibility value are directly related to the errors in the quantified oxygen saturation. As aforementioned, factors such as phase aliasing, partial voluming and high pass filtering will increase the errors in the quantified susceptibility value. Fig. 1a plots the Yv versus susceptibility value. As can be seen, if the measured susceptibility value is less than 0.37ppm (i.e. an error of 18% with respect to an expected value of 0.45ppm), then the calculated oxygen saturation value will be greater than 75% (i.e., an error of 7% with respect to an expected oxygen saturation level of 70%). This value exceeds the upper limit of venous oxygen saturation for a healthy person. This example shows the importance of obtaining an accurate susceptibility value. If the error in susceptibility exceeds 18%, its corresponding oxygen saturation of greater than 75%, could be meaningless for a healthy person. Fortunately, the proposed iterative method helps to increase the underestimated susceptibility, and avoid the overestimated venous oxygen saturation to a certain degree (Table 1 in Ch.4). We also notice that, in the above example, the error of 7% in oxygen saturation is less than half of the error of 18% in the susceptibility. For instance, if we could conquer the problem of the underestimated susceptibility value caused by phase aliasing, partial voluming and high pass filter and control the error of susceptibility value within 10%, then we would reduce the error of oxygen saturation to less than 5%, a clinically acceptable value for quantification of oxygen saturation.

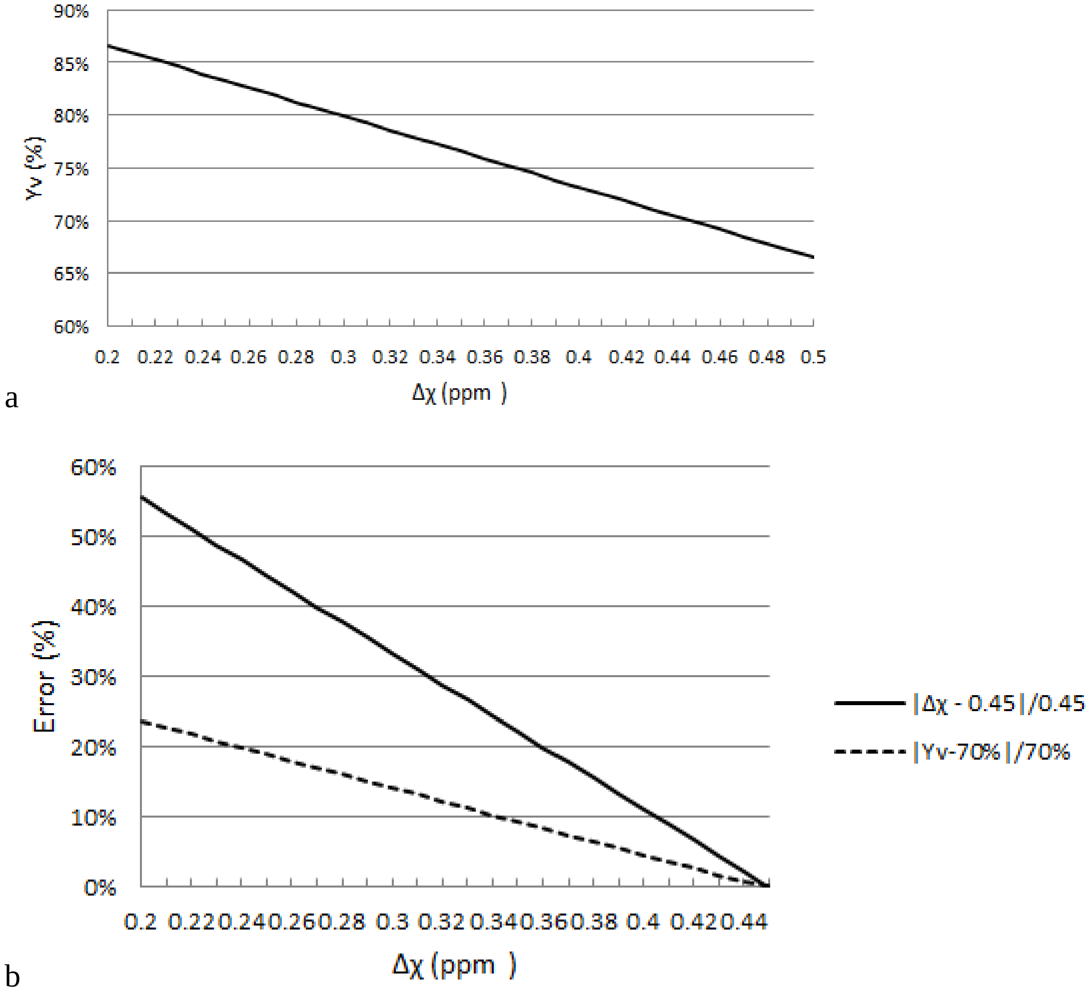

**Figure 1:** a) Venous oxygen saturation Yv as a function of susceptibility. b) Error in both oxygen saturation and Yv as a function of the measured susceptibility. The error (in percentage) is defined as |estimated value – expected value|/expected value. Here 0.45ppm and 70% are the expected values for the susceptibility and oxygen saturation, respectively. The plot shows the errors in oxygen saturation is less than half of the error in susceptibility.

## 5.2 Future Directions

### *Improving the accuracy of measuring the susceptibility of veins using a correction factor method*

Mapping susceptibility from field perturbation data often uses a high pass filter to remove the low spatial frequency phase. The problem of doing this is that the high pass filter will result in a concomitant loss of important local phase information (4) and lead to decreases of susceptibility values inside vessels, especially for large vessels. In addition, with an increase of the filter size, the estimated susceptibility value will be decreased accordingly (Fig.4 in Ch. 3). According to an earlier filter size evaluation (Fig. 4 in Ch. 3), for a large vessel such as the superior sagittal sinus, when a 64×64 high pass filter is applied, the susceptibility value will decrease to only around half of the value without using the high pass filter. If this susceptibility value is used to estimate oxygen saturation, we will obtain a totally wrong answer. Fig. 4 in Ch. 3 gives us a hint that we can estimate the loss the susceptibility value using simulations; therefore, it should be possible to compensate for the loss of susceptibility values (due to using a high pass filter) pixel by pixel inside the vessels using a correction factor (CF) obtained from forward modeling of the veins. If the problem of the underestimated susceptibility values due to using a high pass filter can be solved using this CF approach, it would help to improve the accuracy of susceptibility quantification and oxygen saturation quantification of veins.

### *Building a vessel phantom to verify these algorithms*

The proposed algorithms, i.e., the regularized inverse filter and the k-space iterative method, have been verified using simulations. We could build a vessel phantom to further verify these two algorithms and building a vessel phantom could also prove useful for validating the newly developed algorithms. We could build a vessel phantom containing tubes of different radii, coiled in a tortuous configuration. The coiled phantom can have no flow, flow and be doped with contrast agent to allow us to mimic a variety of vascular situations to accurately create SMs and ensure that flow effects (which often create phase problems) do not interfere with the susceptibility estimates. By filling the tubes in the phantom with Gd-DTPA solution of known susceptibility, we could verify the quantitative accuracy the susceptibility quantification algorithms under various experimental conditions. The multiple windings surrounded by gel in the phantom make various angles to the main field throughout the course of their length and would provide an excellent test scenario of veins making different angles to the main magnetic field. The orientation of the vessels can also be changed by changing the phantom's orientation with respect to the main magnetic field. Both these situations allow us to verify that the SMs are independent of vessel orientation. This phantom could be used to evaluate modifications in the imaging parameters such as the use of shorter echo times mentioned above for SM. If this approach were to prove viable, then this would have a major clinical impact on the use of SM to evaluate oxygen saturation in the clinical domain.

***Measuring oxygen saturation in the Superior Sagittal Sinus (SSS)***

Measuring oxygen saturation in SSS is meaningful since the SSS drains the outer tissue including gray matter and provides a global estimation of oxygen consumption (5). Many of the most common disorders of the brain, such as Alzheimer's, Parkinson's, Huntington's and multiple system disorder have been found to be associated with alterations in cerebral oxygen metabolism(6). The SSS is likely to be preferred over the internal jugular vein (another major draining vein) in light of the often severe susceptibility artifacts caused by the proximity of air spaces such as the oral cavity and trachea. The internal jugular vein by C2/C3 collects blood from the brain. Starting at the superior bulb, it runs down the neck in the vertical direction and ends at the inferior bulb. Monitoring oxygen saturation in jugular venous blood gives an estimate of the balance of global oxygen delivery and cerebral oxygen consumption. Xu et al (7) have previously shown that the oxygen saturation levels in the SSS are comparable to those in the internal jugular vein. Phase measurement in the SSS is convenient and robust in the absence of major tissue interfaces with markedly different susceptibilities (6). As introduced in Chapter 2, magnetic resonance oximetry (8) was used in studies (9–13) to calculate the oxygen saturation level (Y) based on a cylindrical model. With improved accuracy of susceptibility maps using the proposed regularized inverse filter, $1/g_{reg}(k)$, and the k-space iterative method, we would be able to calculate Y in SSS using susceptibility mapping. Then, we can do compare the result from using susceptibility mapping with the one from magnetic resonance oximetry. However, one major problem may be the fact that the SSS sits on the surface of the brain and it may not be possible to give full phase information on the external side. This will need to be investigated in any future study. The next two biggest veins are the straight sinus and the inferior saggital sinus but they drain the medial aspects of the brain (including the deep gray matter). Still they are of equal interest and are surrounding by tissue where phase information external to the brain is available for SM.

### ***Combining with CBF to calculate the cerebral metabolic rate of oxygen utilization ($CMRO_2$)***

As discussed in Chapter 1, $CaO_2$ indicates the arterial oxygen content, CBF indicates cerebral blood flow rate and OEF denotes the oxygen extraction ratio defined as (Ya-Yv)/Ya. Here, Ya and Yv denote the oxygen saturation values of arteries and veins, respectively. Perfusion weighted imaging (PWI) offers an approach to quantify relative cerebral-blood volume (rCBV), cerebral blood flow (CBF) and time-of-arrival (TOA) of local blood flow. Using CBF from the PWI data along with the oxygen saturation from SM, would make it possible to calculate $CMRO_2$. This will help us to understand the hemodynamics of the whole brain. This is one of the main directions we see the use of susceptibility mapping going in the next few years.

**References:**

1. Haacke EM, Reichenbach JR. Susceptibility Weighted Imaging in MRI: Basic Concepts and Clinical Applications. New Jersey: John Wiley & Sons, Hoboken; 2011.

2. Deville G, Bernier M, Delrieux JM. NMR multiple echoes observed in solid ^{3}He. Phys. Rev. B. 1979 Jun 1;19(11):5666–88.

3. Xu Y, Haacke EM. The role of voxel aspect ratio in determining apparent vascular phase behavior in susceptibility weighted imaging. Magn Reson Imaging. 2006 Feb;24(2):155–60.

4. Haacke EM, Ayaz M, Khan A, Manova ES, Krishnamurthy B, Gollapalli L, et al. Establishing a baseline phase behavior in magnetic resonance imaging to determine normal vs. abnormal iron content in the brain. J Magn Reson Imaging. 2007 Aug;26(2):256–64.

5. Ge Y, Zhang Z, Lu H, Tang L, Jaggi H, Herbert J, et al. Characterizing brain oxygen metabolism in patients with multiple sclerosis with T2-relaxation-under-spin-tagging MRI. J. Cereb. Blood Flow Metab. 2012 Mar;32(3):403–12.

6. Jain V, Langham MC, Wehrli FW. MRI estimation of global brain oxygen consumption rate. J. Cereb. Blood Flow Metab. 2010 Sep;30(9):1598–607.

7. Xu F, Ge Y, Lu H. Noninvasive quantification of whole-brain cerebral metabolic rate of oxygen (CMRO2) by MRI. Magn Reson Med. 2009 Jul;62(1):141–8.

8. Haacke EM, Lai S, Reichenbach JR, Kuppusamy K, Hoogenraad FGC, Takeichi H, et al. In vivo measurement of blood oxygen saturation using magnetic resonance imaging: A direct validation of the blood oxygen level-dependent concept in functional brain imaging. Human Brain Mapping. 1997 Jan 1;5(5):341–6.

9. Liu Y, Pu Y, Fox PT, Gao J. Quantification of dynamic changes in cerebral venous oxygenation with MR phase imaging at 1.9 T. Magnetic Resonance in Medicine. 1999 Feb 1;41(2):407–11.

10. Fernández-Seara MA, Techawiboonwong A, Detre JA, Wehrli FW. MR susceptometry for measuring global brain oxygen extraction. Magnetic Resonance in Medicine. 2006 May 1;55(5):967–73.

11. Wright GA, Hu BS, Macovski A. Estimating oxygen saturation of blood in vivo with MR imaging at 1.5 T. Journal of Magnetic Resonance Imaging. 1991 May 1;1(3):275–83.

12. Langham MC, Magland JF, Epstein CL, Floyd TF, Wehrli FW. Accuracy and precision of MR blood oximetry based on the long paramagnetic cylinder approximation of large vessels. Magnetic Resonance in Medicine. 2009 Aug 1;62(2):333–40.

13. Langham MC, Magland JF, Floyd TF, Wehrli FW. Retrospective correction for induced magnetic field inhomogeneity in measurements of large-vessel hemoglobin oxygen saturation by MR susceptometry. Magnetic Resonance in Medicine. 2009 Mar 1;61(3):626–33.